Computational Study of Rotating Stall in High-Speed Compressor

by

Jun Luo

B.E. Aerospace Engine, Beijing University of Aeronautics and Astronautics
Beijing (1998)

Submitted to the Department of Aeronautics and Astronautics
in partial fulfillment of the requirements for the degree of

MASTER OF SCIENCE IN AERONAUTICS AND ASTRONAUTICS

at the

MASSACHUSETTS INSTITUTE OF TECHNOLOGY

May 2003

Author .....

Department of Aeronautics and Astronautics
May 23, 2003

Certified by .....

Yifang Gong, Thesis Advisor
Research Engineer

Certified by .....

Choon S. Tan, Thesis Advisor
Senior Research Engineer

Accepted by .....

Edward M. Greitzer
H. N. Slater Professor of Aeronautics and Astronautics
Chair, Committee on Graduate Students

Computational Study of Rotating Stall in High-Speed Compressor

by

Jun Luo

Submitted to the Department of Aeronautics and Astronautics

on May 15, 2003 in partial fulfillment of the

requirements for the degree of Master of Science in Aeronautics and Astronautics

Abstract

A computational study of compressor instability based on body force representation of each blade-row of a transonic stage has been implemented for both clean inlet flow and flow with circumferential total pressure inlet distortion. The computational results indicate that many aspects related to compressor instability differ from what was observed in the experiment: steady compressor characteristics, stalling mass flow as well as the key details in stall inception process. The discrepancy has been attributed to the inadequacy of the body force formulation, which only reproduces the design operating point of the research compressor. In order to overcome this inadequacy, a procedure is proposed and implemented to modify the compressor body force based on the experimental data to match the stalling mass flow and compressor characteristic slope near stall. To assess the adequacy of the modified body force formulation, instability calculations incorporating the modification are carried out for both clean inlet flow and flow with circumferential total pressure inlet distortion. The modified body force formulation gives a computed stalling mass flow in agreement with measured value. While it also yields the modal type stall inception that are in agreement with experiment for clean inlet flow, the computed stall inception with inlet distortion differs from experiments in which the stall inception is through spike followed by modal wave disturbance. The calculations with inlet distortion show that both the compressor performance and the stability margin deteriorate.

Thesis Supervisors: Yifang Gong

Research Engineer

Choon S. Tan

Senior Research Engineer

Acknowledgements

Many people have given me a lot of help in this thesis and made my life at MIT more enjoyable. I would like to express my deep gratitude to them.

First and foremost, I would like to thank my advisors, Dr. Yifang Gong and Dr. Choon S. Tan for their guidance and support throughout this project. Much gratitude is also extended to Dr. James D. Paduano for his guidance, lots of help and financial support. I would also like to express my sincere thanks to those professors who taught me the courses at MIT: Professor Epstein, Professor Greitzer, Professor Spakovszky, Dr. Tan, Professor Drela in Department of Aeronautics and Astronautics; Professor Sonin and Professor Mckinley in Department of Mechanical Engineering. I believe all the knowledge I have learned at MIT will benefit my future development and even the whole life.

In addition, I am also thankful to the staff and graduate students of Gas Turbine Laboratory. Paul Warren, Julie Finn, Holly Anderson, Dongwon Choi, Brenda Macleod, Beilene Hao, Andrew Luers, Neil Murray, Yong Wang, Yiben Lin, Lixian Liu, Deborah Pilczer, Sebastien Akouche, Jhongwoo Peck, Bobby Sirakov, Van-Man Lei, Chiang Juay Teo, Benny Chi Kin Yam, Dr. Hongwei Sun, Dr. Shengfang Liao. Their friendship and help has been invaluable and is well appreciated.

I would like to thank my family, my parents and my sister for their continued moral support throughout all the time that I have spent at MIT.

Last but not least, I would like to thank my girlfriend Lingling Li for her moral support and encouragement.

This research was funded by the U.S Air Force under a Grant F49620-00-0014 and its support is gratefully acknowledged.

Centents

List of Figures

Chapter 1

Introduction

1.1 Introduction

The compressor is one of the three primary components of a gas turbine engine (the other two being the combustor and the turbine). As the mass flow through the compressor is decreased, the angle of attack increases, the pressure rise across the compressor increases, this trend continues until a point is reached where the flow cannot sustain the pressure rise across the compressor and the flow through the compressor becomes unstable. Loss of stability is undesirable, as the amplitudes of the unstable oscillations are often very large and can cause severe damage to the compressor blades. In addition, the loss of stability is accompanied by a significant loss in pressure rise. To avoid such instabilities, the compressor (hence the engine) has to work at an operating point corresponding to lower pressure ratio so that an adequate stall margin is maintained. The stall margin can be considerably reduced in operating environments for which the inlet flow conditions are non-uniform.

1.2 Overview of Compression System Instabilities

Conceptually, a compression system is represented by a series of components comprising

1. Inlet duct, which provides the necessary mass flow for the compression system
2. Compressor, which is the core component of the compression system and produce pressure rise.
3. Plenum, which is used to store the mass flow and acts like a combustion chamber
4. Throttle, which is used to regulate the mass flow through the compression system and acts like a turbine.

The basic structure of a compression system is shown schematically in Fig. 1.1.

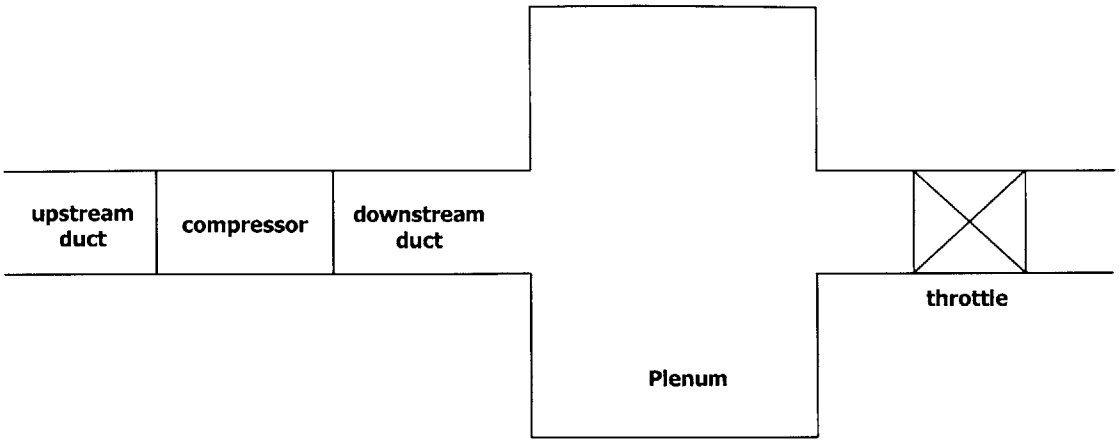

Fig. 1.1 Basic components of compression system

1.2.1 Types of Instability in Axial Flow Compressors

Three types of instability behavior have been observed at compressor operating points beyond the instability point. They are progressive stall, 'abrupt' stall, and surge. They are characterized in terms of pressure rise characteristics (Fig. 1.2) and flow field respectively (Fig. 1.3).

With progressive stall, there is a gradual deterioration of pressure rise. The pressure rise characteristic is shown in Fig. 1.2 (a). This happens for example when a multistage compressor is operated at a speed below the design speed. The flow field associated with this type of instability is illustrated in Fig. 1.3 (a) which shows several part-span stall cells rotating around the annulus. This flow pattern usually occurs in one or several stages in a multistage compressor.

Abrupt stall features with a sudden drop of pressure rise at the compressor performance map, with the formation of a full span stall cell (stall cells that extend from hub to tip). The stall cell has an axial extent that encompasses the whole compressor; this explains the large drop of pressure rise (in comparison to the situation in the part-span stall cell pattern). To recover from this type of stall pattern, the throttle has to be moved to a position corresponding to a corrected mass flow much larger than that at which the compressor would stall upon throttle closing. This effect is usually referred to as hysteresis, shown in Fig. 1.2 (b).

Surge is a system-type instability, it is a global one dimensional flow instability that includes the whole compression system. The mass flow undergoes large amplitude

oscillations where the entire compression system depressurizes and repressurizes, forming the surge cycle as shown in Fig. 1.2 (c). Sometimes, when surge occurs, the flow oscillations are so severe that the flow through the compressor reverses, a flame can be seen at the intake and exhaust as the combustion moves forward and backward from the combustor.

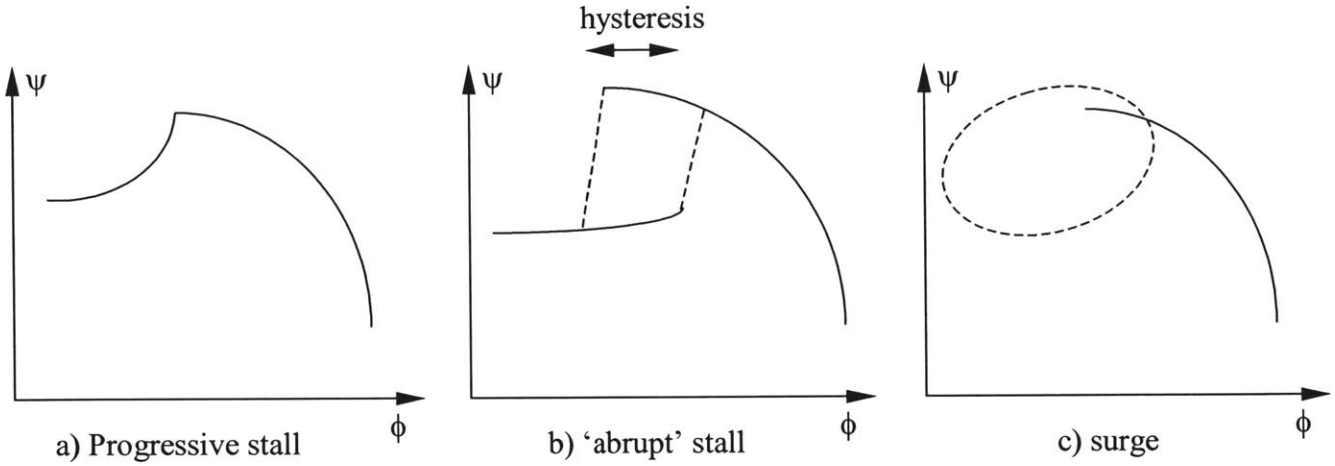

a) Progressive stall b) 'abrupt' stall c) surge

Figure 1.2 Three types of compressor instability characterized in terms of the respective pressure rise characteristics

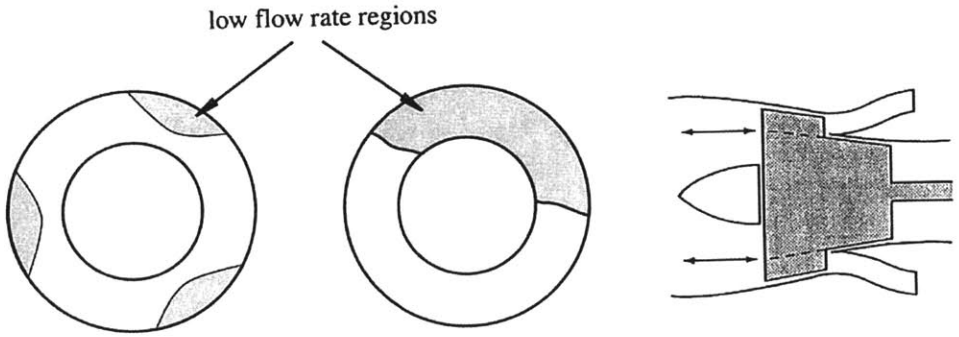

(a) Part span stall (b) Full span stall (c) Surge

Fig. 1.3 Three types of instabilities in a compression system characterized in terms of respective flow field

1.2.2 Onset of Instability

Predicting the condition at which instability will occur in a compressor requires an understanding of the flow processes leading to the onset of instability. The phenomena described in the previous subsection are the final forms of instability. And it's important

to distinguish the final form from the onset of instability. The transition from initial disturbance to final stall or surge can be usefully divided into three stages (1) inception; (2) development; and (3) final flow pattern. The inception stage is the period when disturbances start to grow (flow becomes unstable). It defines the operating point and conditions for which instability occurs. In practice, the disturbances will take a finite amount of time (from a few to several hundred rotor revolutions) to grow into final stall or surge, so that the inception stage can be viewed as the early development of the unstable flow.

For some compressors, the inception stage consists of the linear growth (extending up to several hundred rotor revolutions) of disturbances of infinitesimal amplitude, while in others the inception stage only extends over one or two rotor revolutions after its detection. The stall inception stage is the major focus of the instability modeling and prediction.

The development stage, which includes all the processes after the inception stage before the final flow pattern to be reached, is usually of less importance. It is often the case that one final form of instability could be the pre-stage of the other final form in the same compressor. For example, rotating stall might cause surge in some compressors, as noted by Greitzer [1]:

Surge is basically one-dimensional phenomenon, involving on overall, annulus averaged compressor performance curve. For typical volumes, lengths, and throttle characteristics must generally be slightly positive sloped for system instability to occur. We have also seen that the axisymmetric flow through a compressor can be unstable to two (three) dimensional infinitesimal disturbances, and that this local instability marks the inception of rotating stall. However, the onset of this rotating stall is very often associated with a precipitous drop in the overall ("one-dimensional") pressure-rise mass flow curve of compressor performance. In other words, the inception of rotating stall can lead to a situation where the instantaneous compressor operating point is on a steeply positively sloped part of the characteristics, with a consequent violation of the dynamic and /or the static instability criteria.

1.2.3 Stall Inception

The stall inception stage is the period when disturbances start to grow and flow field begins to become unstable. Accurate prediction and description of stall inception process are of considerable engineering value in that it defines the stable operating range of the compressor.

Two major inception types have been experimentally identified: modal waves, and spikes. Modal waves are exponentially growing long wavelength (length scale comparable to the annulus) small amplitude disturbances. The rotating speed of this type of disturbance is in the range between 20% to 50% of rotor speed. Modal wave penetrate the whole compressor in the axial direction, so they can be detected by sensors at any locations at the inlet, exit, or within the compressor. Usually, this type of stall inception occurs at a point near the peak of the characteristics and this type of inception can be well described by linear stability theory. Moore-Greitzer model [2] predicted the pre-stall modal wave before measurements were taken [3].

The other inception mechanism is the growth of localized non-linear short wavelength (with length scale of several blade pitches) disturbances [4]. This type of stall inception is referred to as "short wavelength stall inception". The inception starts as one or several spike-shaped finite amplitude disturbances within the tip region of a particular stage. Usually the disturbances develop into a large full span stall cell within three to five rotor revolutions. The initial rotating speed of this type of disturbances is about 70% of rotor speed, substantially higher than that for the typical modal wave speed. Fig. 1.4 shows the velocity traces that lead to rotating stall through modal wave disturbances [17].

From experimental observations, Camp and Day [21] concluded that the spike-type stall inception occurs at a "unique rotor tip incidence". They examined a specific compressor with different IGV stagger angles and found that the stall points line up on a constant rotor tip incidence line whenever the compressor shows spike as its stall inception mechanism. The stall inception mechanism could be switched between modal type and spike-type for the same rotor and stator but with different IGV stagger. The overall trend is that when the first rotor is highly loaded (higher pressure rise for the given flow coefficient), the compressor tends to show spike-type inception, otherwise it shows modal type of stall inception. These experiments suggest that the first-stage rotor

is the key component responsible for the spike-type stall inception. Fig. 1.5 shows velocity traces in the typical spike stall inception process.

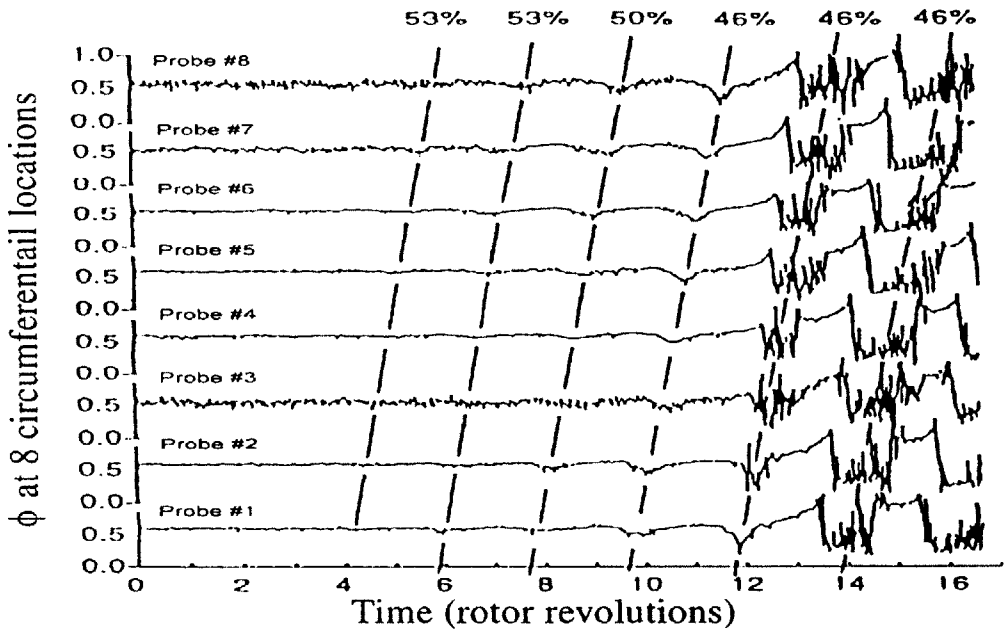

Fig. 1.4 Velocity traces of eight sensors around the compressor annulus show a typical modal wave stall inception process

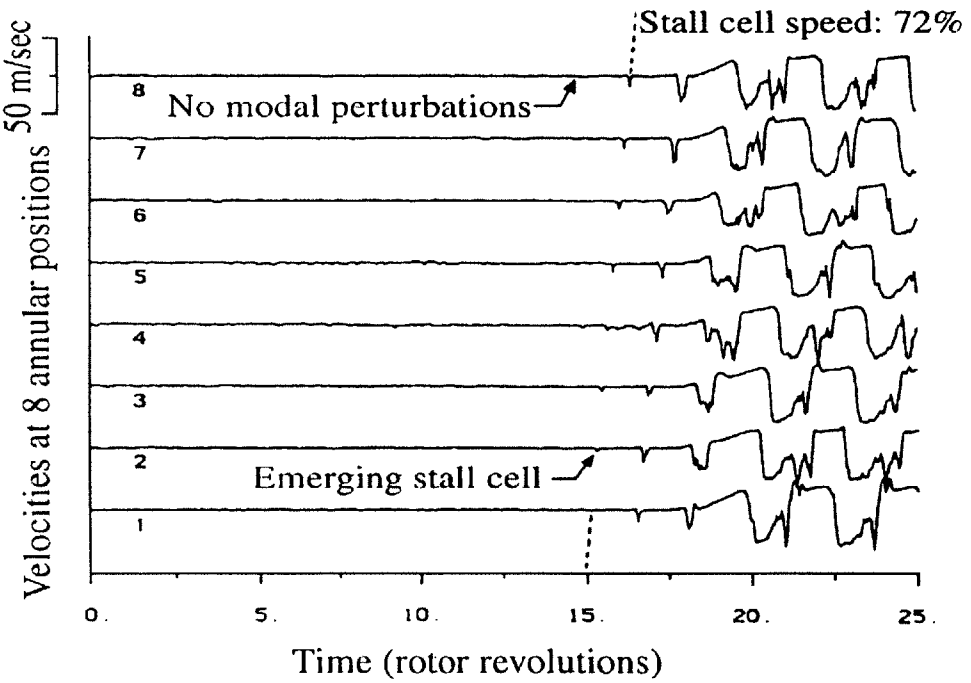

Fig. 1.5 Velocity traces of eight sensors around the compressor annulus show a typical spike stall inception process

Based on their observations, Camp and Day proposed a "unique rotor tip incidence" as a short wavelength stall criterion (Fig. 1.6). When the incidence is reached before the peak of the compressor characteristic, the compressor will stall through short wavelength disturbances; otherwise the compressor will stall at the peak pressure rise and show modal waves as its stall inception type.

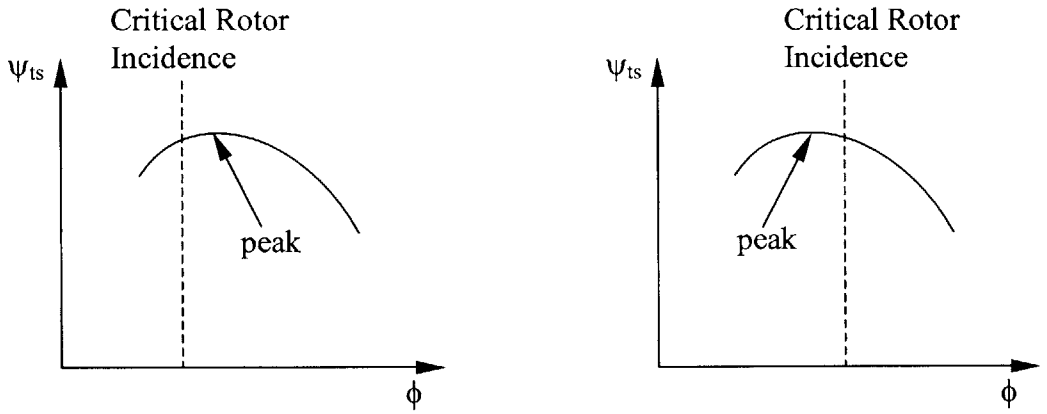

Fig. 1.6 A model for determining the stall inception type of a compressor [21]

Based on the above description, some important distinctions between the two kinds of stall inception (modal wave and spike) can be concluded as follows:

1. The number of blade rows that are responsible for their initiation. Spike stall inception is associated with the breakdown of the flow-field in a single blade row. In contrast, the growth of a modal disturbance is associated with an instability of the flow in the whole compressor.
2. The rotating speed of the disturbances in stall inception process. Spike rotates at a faster speed than modal wave disturbances. Usually modal wave disturbances rotate at about 20%-50% rotor speed, while the rotating speed of spike disturbances is about 70%.
3. Mathematical character. Modal wave disturbances are basically linear, their growth are governed by a exponential function of time, while spike disturbance is always associated with separation and three dimensional flow redistribution phenomenon both of which are nonlinear.

1.3 A Review of Current Modeling for Rotating Stall

There are two central issues of rotating stall prediction: rotating speed and instability point, but from the practical point of view, only the instability point is of real concern. Of engineering value is the capability to establish a casual link between instability behavior and compressor design characteristics.

1.3.1 Stall propagation mechanism

The first rotating stall model was the analysis and physical description proposed by Emmons [5]. It can be summarized as follows.

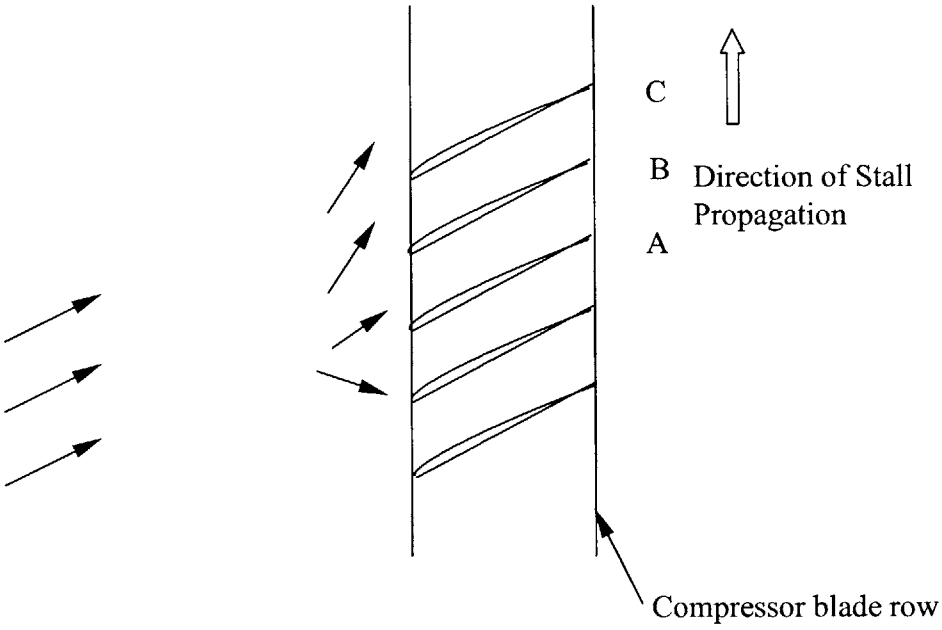

Fig. 1.7 Physical mechanism of rotating stall inception

Fig. 1.7 shows that in a row of highly loaded blades, a minor physical irregularity, or flow non-uniformity, can result in momentary overloading and separation. This separation, or blockage, will restrict the flow through the blade passage and will therefore divert the incoming streamlines. When this happens, the flow can separate from the suction surface of the blade so that a substantial flow blockage occurs in the channel between B and C. This blockage causes a diversion of the inlet flow away from blade B and towards C and A to occur (as shown by the arrows), resulting in an increased angle of attack on C and a reduced angle of attack on A. Since C was on the verge of stall before, it will not tend to stall, whereas the reduced angle of attack on A will inhibit its

tendencies to stall. The stall will thus propagate along the blade row in the direction shown, and under suitable conditions it can grow to a fully developed cell covering half the flow annulus or more. In this fully developed regime, the flow at any local position is quite unsteady; however, the annulus averaged mass flow is steady, with the stall cells serving only to redistribute the flow. Although the sketch only shows one of several possible stall propagation mechanisms, the idea is so intuitive that it is widely accepted by both academic and industrial communities.

Cumpsty and Greitzer [23] used the balance between acceleration in the rotor, stator, and upstream and downstream ducts to argue that the rotating speed of stall cell is determined as the speed at which the unsteady inertial effects in rotors are balanced by the unsteady inertial effects in stationary components. Their model predicted well the measured speed of rotating stall cells. The results also suggest that although the flow redistribution idea is intuitive, the main mechanism for propagation is due to the inertial effects in blade rows and ducts.

1.3.2 Zero Slope Instability Criterion

Perhaps the most well-known instability criterion, which states that the instability will occur at the zero-slope point (peak) of the characteristics, was proposed by Dunham [6]. He found that at zero-slope of total-to-static pressure rise characteristics, the compressor flow field is neutrally stable, which means the disturbances do not decay.

Gysling examined compressor stability in terms of the net mechanical energy input into the flowfield. A compressor puts energy into a non-axisymmetric flowfield disturbance whenever the total-to-total characteristic has a positive slope ($\partial\psi_{tt}/\partial\phi>0$). Mechanical energy can escape since some of it is convected away by the non-steady vortical disturbance in the exit flowfield, and instability will only occur when the compressor puts in more energy than can be convected away (or dissipated in losses). In rough terms, the vortical field carries energy at flow rate "ϕ", the convection speed, and so instability occurs when:

$$d\psi_{tt}/d\phi \approx \phi$$

or equivalently, since $\psi_{tt}=\psi_{ts}+1/2\phi^2$, when

$$d\psi_{ts}/d\phi = 0$$

This is the zero slope of the total-to-static pressure rise characteristic condition.

The zero slope stability criterion may be explained by a static style argument based on changes in the local mass flow and pressure rise in Fig. 1.8

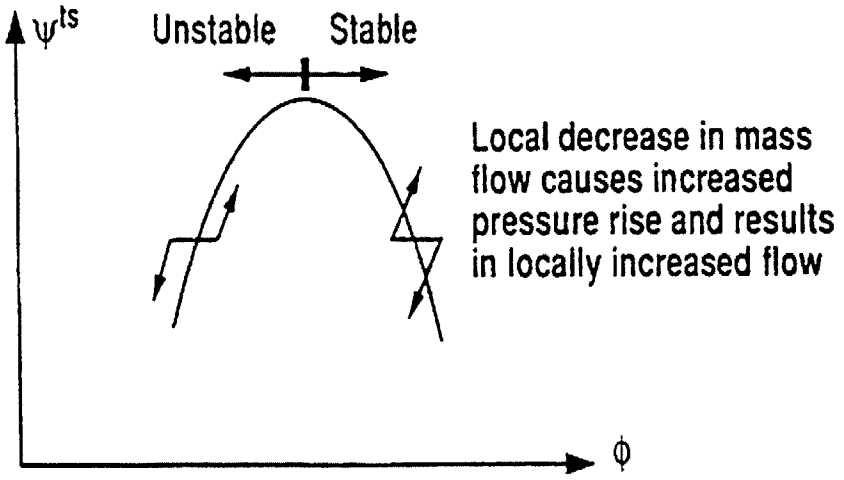

Fig. 1.8 Static argument showing why negative slopes are stable whilst positive ones are unstable

On the negatively sloped pressure rise mass flow characteristics a local increase in mass flow causes a decrease in pressure rise. This causes the flow to decelerate, and the disturbances decay. On a positively sloped characteristic the opposite is true, so any circumferential disturbance is amplified.

1.3.3 Moore-Greitzer Theory

A theory of rotating stall disturbances developed by Moore [7] and a more complete theory of post-stall transients in compressor by Moore and Greitzer [2] are the basis for understanding a different mechanism of rotating stall inception. They assumed that compressor instabilities grow from small amplitude disturbances, and for this reason the linearized form of the equations should accurately describe their initial growth. The inception equations suggest that rotating stall will develop as a result of small flow disturbances that are spatially periodic around the annulus and growing in amplitude. Any spatially periodic disturbance can be represented mathematically as the sum of several pure harmonics (spatial modes) and the growth of any spatial mode can be governed by a exponential function of time.

Although most of the work and development of Moore-Greitzer's model has been for linear cases, the model itself is not limited to small amplitude disturbances. For example, an inlet distortion can be viewed as a stationary large amplitude disturbance. Mathematically, general non-linear disturbances are very hard to be treated analytically; however modern CFD methods can be used to simulate the evolution of any type of disturbances in the system. Longley [17] and Hendricks et al [18] used this idea to simulate instability behavior in high-speed compressors. Escuret and Garnier [19] extended the method to three-dimensional cases.

1.3.4 Three-Dimensionality and Non-Linearity of Rotating Stall

Two-dimensional rotating stall models are limited in that they do not account for flow variations in the spanwise direction. Measurements in compressor rigs indicate that spanwise variations of axial velocity as large as 40% of the mean flow can arise before stall [12]. Reid [24] and Spakovszky et al. [32] showed that radial total pressure distortions at the inlet of the compressor reduced the stalling pressure rise. Gorrell et al. [33] altered casing treatment designs and observed that rotors with the most uniform radial profile of pressure ratio led to the most stable compressors. These results reveal the importance of radial flow variations in affecting the stall point.

Two-dimensional models usually use either a radial average of the flow variation [32,34], or else applied at the mean-radius [35]. To account for the spanwise flow nonuniformity, it has been proposed that the stability of the compressor can be determined by a two-dimensional model at the most unstable spanwise region [36]. The validity of such a proposition is not yet known, although experimental evidence indicates that the location of the stall cell is often linked to the location of highest loading and the lowest velocity. McDougall et al. [36] observed that modal waves had the largest amplitude at either the hub or tip, determined by which region had excessive blockage before stall. Camp and Day [21] found that increased rotor tip loading led to spike stall inception at the outer radius; but increased hub blockage, which diverted the flow outward to unload the tip, led to a modal-type stall inception. On the other hand, Soundranayagam and Elder [37] measured stall inception occurring at the tip of a fan, despite forcibly degrading the root performance; and Jackson [38] detected stall at the tip

of a single stage compressor. All the above work demonstrates the importance of three-dimensionality in stall inception process.

Another important aspect of rotating stall is its non-linearity. Although the linearized analyses have in the past been used to try to predict some of the features of fully developed rotating stall, it has become clear that in this flow regime the stall cells are definitely not small perturbations and linear analysis is not applicable. Thus this type of investigation is only useful for the problem of stall inception, and to follow the subsequent development of rotating stall, one must use a nonlinear model. This has been done by Nakata and Nagano [14], as well as Orner [29]. Extension of these calculation procedures to the case of circumferentially distorted inlet flow has been carried out by Adamczyk [30] and Pandolfi and Colasurdo [31]. These models use time marching techniques to determine whether a small disturbance will grow or decay by calculating the development of the flow to some eventual steady-state solution. This could consist of a flow with a large amplitude disturbance propagating around the compressor, which is taken to be indicative of compressor operation in rotating stall. However, these early efforts [14] did not show much positive results mostly due to the lack of computational resources. Recently, several CFD methods have been used to simulate compressor instability [15, 16]. One advantage of these methods is that they can relate the blade passage events to the instability. One uncertainty of these calculations is that they are performed on a single rotor blade row, since no data are available on short wavelength stall inception in a single rotor. Although CFD can play an important role for implementing computation to provide information on instability behavior that is difficult to measure in a laboratory/test rig, such simulations are still beyond the presently available computational resources for multistage axial compressors.

There is another class of methods that uses both modeling and CFD technique to model the flow in a compression system. These methods could handle three-dimensional nonlinear flow phenomena in a practical manner and require reasonable amount of computational resources. These methods have been demonstrated to be able to compute steady three-dimensional inlet distortion cases [20], long wavelength disturbances in a three-dimensional compressor [19] and disturbances in two-dimensional high-speed

compressors [18]. Conceptually this type of model is able to handle non-linear three-dimensional disturbances (spike) in a compressor.

Gong [9] used body force model, which replace the compressor blades by the body force imposed by the blades to the flow field to simulate rotating stall in GE 4 stage low speed compressor with clean inlet flow. A significant feature of the body force representation is that it is a function of local flow properties. This is essential to model short wavelength disturbances in compressors where flow redistribution occurs in a blade row in the presence of these disturbances. The strength of this computational model is that the compressor is naturally coupled with unsteady three-dimensional flow, so that the model could be used to investigate the interactions between compressor and other components, such as interaction between intake and compressor with inlet distortions, and its impact on the performance and stability margin; The behavior of inlet vortex in an intake and engine, and its impact on the performance and stall margin, etc. Gong also extended the body force model for low speed compressors to high-speed compressors, in which compressor response to inlet distortion was the main focus. However, no effect has been made to quantify the effect of inlet distortion on instability behavior using Gong's formulation, this constitutes the main motivation for the current research focus

1.3.5 Inlet Distortion Effects on Compressor Operability

The above discussions mainly focus on the case with clean inlet flow, which is circumferentially uniform. However, in practice, there are a lot of other factors that can significantly affect the point at which the onset of instability occurs. One of the most important of these is inlet distortion, which is a term used to describe a situation in which substantial total pressure, total temperature, velocity, and/or flow angle variations exist at the compressor inlet face. Aircraft engines are particularly prone to inlet distortion problems due to changes in aircraft altitude and the effect of the airframe on the inlet flow conditions. However, industrial installations can also suffer from inlet distortion in cases where poorly designed bends have been installed upstream of the compressor. In these situations, some portion of the blading is likely to be operating under more unfavorable conditions than would occur with a uniform flow at the same mass flow rate, leading to a decrease in the useful range of operation of the machine.

An illustration of the effect of inlet distortion on compressor stability and performance is given in Fig. 1.9, which shows data from a nine-stage axial flow compressor [24]. The horizontal axis is the corrected mass flow, and the vertical axis is the total pressure ratio. The dashed lines indicate the measured performance with a uniform inlet, while the solid curves give the measured performance with a circumferential distortion, i. e., circumferentially nonuniform inlet flow. It can be seen that there is a substantial degradation in performance and, more importantly, a large drop in the stability margin due to the inlet distortion. While the consequences may not be this severe with all compressors, there is generally a reduction in the stability of the compression system associated with the presence of an inlet distortion.

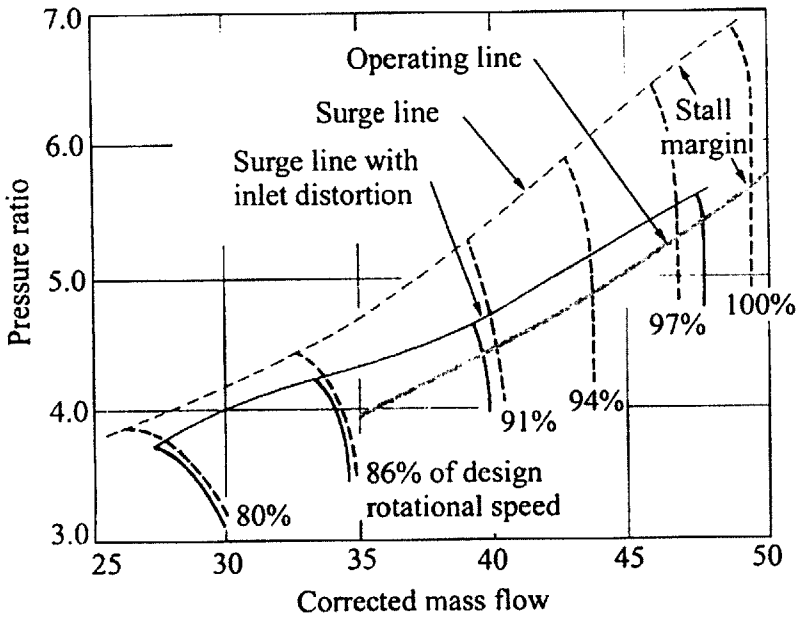

Fig. 1.9 Effect of Inlet Distortion on Axial Compressor Performance and Stability [24]

Because of the widespread occurrence of inlet distortions, and their adverse effects on system stability, there has been a large amount of work on the problem of predicting compressor response to flow distortion. For example, Mazzawy developed a nonlinear compressible flow model, which can predict compressor performance and stability with a circumferential flow distribution. This model uses multiple parallel compressor segments and accounts for deviations from undistorted compressor performance. Hynes and Greitzer [8] studied the compressor stability with inlet distortion, it is basically an extension of Moore-Greitzer model to the case with inlet distortion. Longley et al. [26]

investigated the effects of rotating inlet distortions on compressor stability in several compressors, and found that there are two types of compressor response (measured in terms of stall margin vs. rotating speed of the distortion): One shows a single resonance peak corresponding to a large decrement in stall margin when inlet distortion is rotating at around 0.4 rotor speed in the direction of rotor rotation (Fig. 1.10 a); the other shows two resonance peaks at 0.3 rotor speed as well as at 0.75 rotor speed (Fig. 1.10 b). The compressors which show one resonance peak stall through modal waves while the other exhibit the spike type of stall inception. Thus the respective characteristic response of the compressor corresponds to two types of observed stall inception mechanisms which have different impact on stall margin due to inlet distortions.

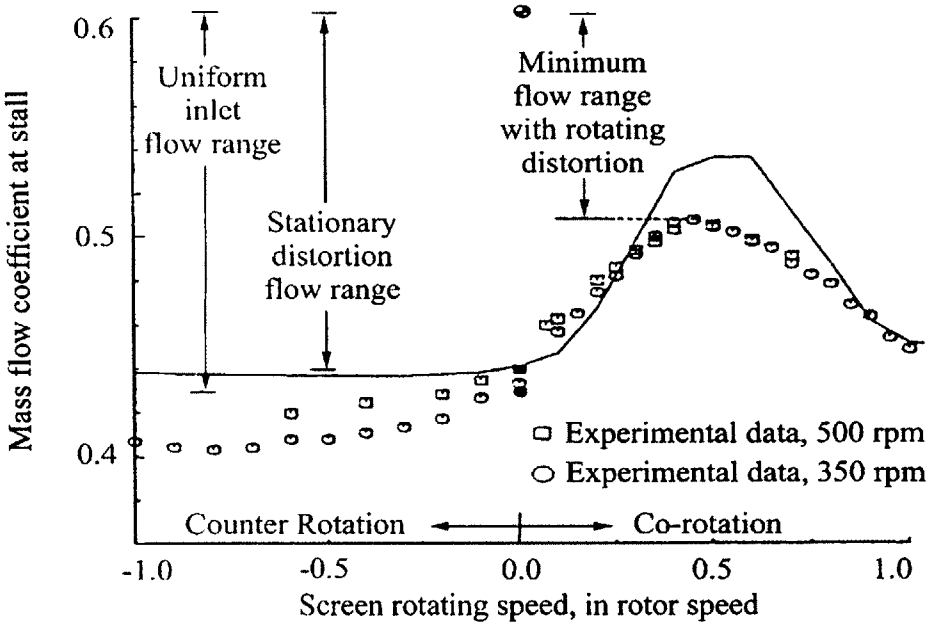

(a) Single resonance peak

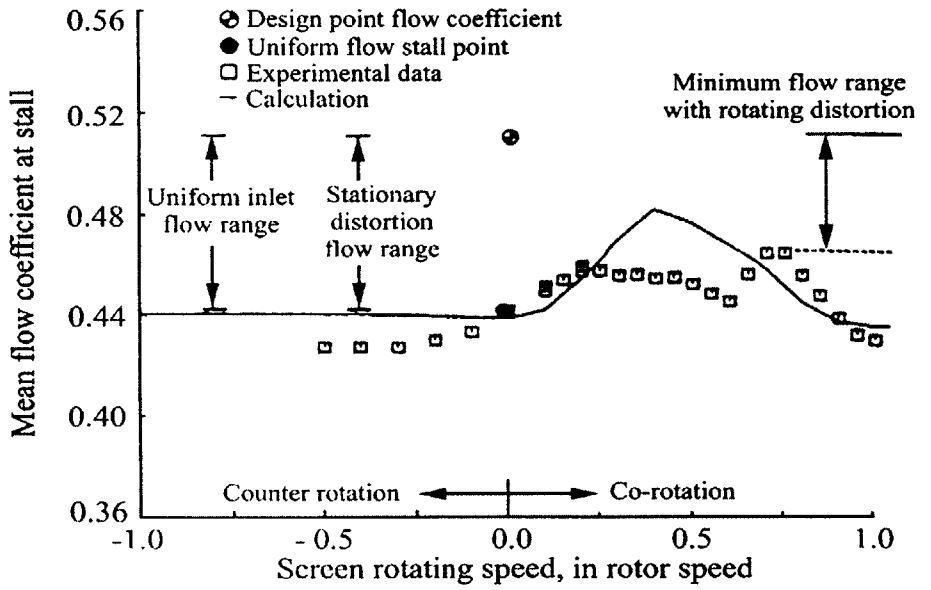

(b) Two resonance peaks

Fig. 1.10 Two types of compressor resonance response to rotating inlet distortions [26].

1.4 Research Objectives

A key objective of this thesis is to assess the adequacy of Gong's computational model [9] for simulating instability behavior in high-speed compressor. As noted in Section 1.3.4, Gong's computational model [9] for high-speed compressor has not been applied to simulating compressor instability inception and development in a representative high-speed compressor stage. In addition, the adequacy of the computational model is to a large extent determined by the level of details in body force representation of the compressor blade row. Specifically, we need to address the issue on the level of details needed: ***is the body force formulation proposed by Gong [9] able to capture the key aspects of instability inception and development in high-speed compressor?***

In addition, other important issues that need to be addressed are:

1. The instability behavior of a high-speed compressor with clean inlet flow versus inlet distorted flow;
2. The effect of inlet distortions of different length scale and time scale on compressor operability;

1.5 Contributions

The contributions of this thesis can be described as follows:

While the work constituted a first attempt on using body force representations of blade rows to simulate instability behavior in a high-speed single stage compressor for both clean inlet flow and inlet distorted flow, the results indicate that a body force representation that match the design point performance is not adequate for instability simulation. Modifying the body force representation to match the stalling mass flow and compressor characteristic slope near stall reproduces the stalling point but not the stall inception behavior.

1.6 Thesis Organization

This thesis is organized as follows: Chapter 2 describes the computational model for high-speed compressors developed in [9], which will be used to study the instability behavior of the research compressor in this thesis. Chapter 3 presents representative instability calculations of NASA research compressor stage 35 using Gong's body force

formulation for both clean inlet flow and distorted inlet flow for determining the effect of inlet distortion on compressor operability. In addition, the computational results are compared with experimental data in terms of compressor characteristic, stalling mass flow and stall inception process. The observed differences are attributed to the inadequacy of the body force formulation in Gong [9] for simulating rotating stall at 70% rotor speed. Based on the explanation in chapter 3, chapter 4 presents a method on how to modify the body force formulation using available experimental data at 70% compressor speed. Representative instability calculations are given in chapter 4 with the modified body force formulation. Chapter 5 summarizes the main work of this thesis and states the key conclusions. Finally, recommendations for future work are suggested.

Chapter 2

Computational Flow Model for High-speed Compressors

A brief introduction of non-linear three-dimensional computational model for high-speed compressors which was developed by Gong [9] will be presented in this chapter.

This non-linear three dimensional computational model developed in [9] is aimed at simulating three-dimensional finite amplitude disturbances such as inlet distortions, short wavelength stall inception process, and part-span stall cells, which are encountered by compressors. The basic idea of the model is to emphasize the response of a blade row to unsteady three-dimensional non-uniform flow but ignores the detailed flow structure in each individual blade passage. Therefore, the desired model should at the very least include the following key issues:

1. A non-linear three-dimensional flow field which includes flow redistribution both between blade rows and in each blade;
2. The response of blade rows to general three-dimensional non-linear disturbances;

Based on the above analysis, some simplifications were made in [9] to make the model practicable for currently available computational resources (i.e to avoid the need to resolve the flow structure in each individual blade passage), they include:

1. Infinite number of blades assumption. There are two considerations that should be noted: (i) the phenomena of smallest length scale under consideration has a length scale of several blade pitches, so that the present assumption is marginal in being adequate to capture the key physics of these disturbances; (ii) the resolution of flow field in every blade passage is not computationally feasible with currently available computational resources. The adequacy of this model has been demonstrated in [9].
2. A local pressure rise characteristic in every small portion of a blade passage can be defined. This aspect of the model is different from the other two-dimensional and three-dimensional models, which assume that blade row performance is essentially set by the inlet conditions. It is essential for a blade row to respond in a local manner, since flow redistribution is expected within a blade row. This

treatment is consistent with the infinite number of blades assumptions, and is thus good for a blade passage of high solidity.

In addition, due to compressibility, some additional effects are introduced such as:

1. Phenomenon unique to high-speed compressors (choking, shock) can change the behavior of the system;
2. Behavior of acoustic waves need to be considered in the prediction of compressor instability
3. Blade rows and ducts also act to increase the effective flow capacity of the plenum of a compression system.

The following section will describe briefly the computational model in [9] for high-speed compressors, it consists of governing equations, formulation of body force in blade regions.

2.1 Modeling of a Compression System

A compression system, which is illustrated in Fig. 2.1, consists of an inlet duct, an exit duct, blade rows, gaps between blade rows, a plenum, and a throttle. Each component will be described in the following:

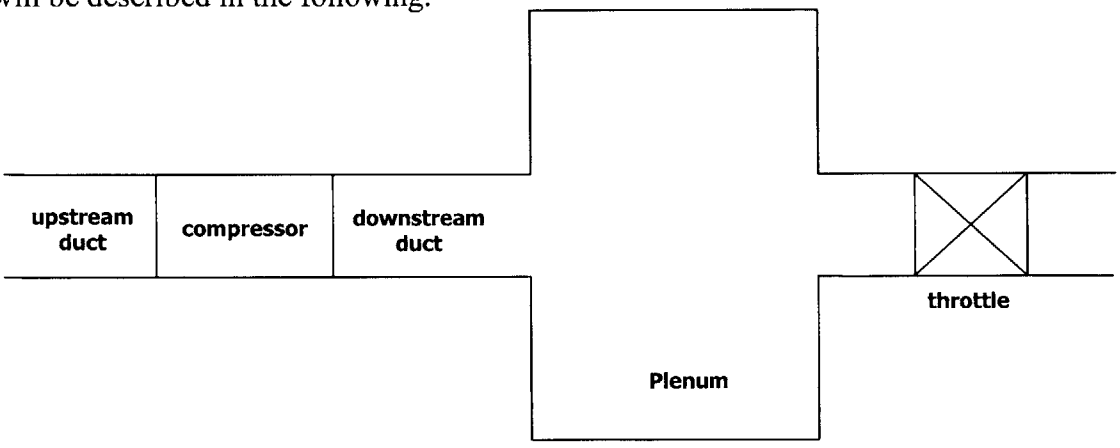

Fig. 2.1 Illustration of a compression system

2.1.1 Flow in Ducts

The flow in inlet duct, exit duct and intra-blade-row gaps is described by the three-dimensional unsteady Euler equations for mass, momentum, and energy conservation:

$$\frac{\partial}{\partial t}\begin{bmatrix} r\rho \\ r\rho V_x \\ r\rho V_\theta \\ r\rho V_r \\ r\rho e_t \end{bmatrix} + \frac{\partial}{\partial x}\begin{bmatrix} r\rho V_x \\ r\rho V_x^2 + rp \\ r\rho V_x V_\theta \\ r\rho V_x V_r \\ rV_x(\rho e_t + p) \end{bmatrix} + \frac{\partial}{\partial \theta}\begin{bmatrix} \rho V_\theta \\ \rho V_x V_\theta \\ \rho V_\theta^2 + p \\ \rho V_\theta V_r \\ V_\theta(\rho e_t + p) \end{bmatrix} + \frac{\partial}{\partial r}\begin{bmatrix} r\rho V_r \\ r\rho V_x V_r \\ r\rho V_\theta V_r \\ r\rho V_r^2 + rp \\ rV_r(\rho e_t + p) \end{bmatrix} = \begin{bmatrix} 0 \\ 0 \\ -\rho V_\theta V_r \\ \rho V_\theta^2 + p \\ 0 \end{bmatrix} \quad (2.1)$$

2.1.2 Flow in Blade-Rows

Under the assumption that the number of blades is infinite (or the length scale of flow events is much larger than a blade pitch), the flow at each circumferential position (or at each infinitesimal blade passage) can be regarded as axisymmetric flow in a coordinate frame fixed to the blade row. The pressure rise and flow turning due to the blades can thus be simulated by a body force field. Due to the presence of the blades, the flow fields between any two blade passages can be different, therefore a three-dimensional flow field in a blade row can be composed of an infinite number of axisymmetric flow fields.

In the blade row region, the assumption of infinite number of blades implies that the flow is locally axisymmetric in the blade row reference frame. The equations for blade rows are as follows:

$$(\frac{\partial}{\partial t} + \Omega\frac{\partial}{\partial \theta})\begin{bmatrix} r\rho \\ r\rho V_x \\ r\rho V_\theta \\ r\rho V_r \\ r\rho e_t \end{bmatrix} + \frac{\partial}{\partial x}\begin{bmatrix} r\rho V_x \\ r\rho V_x^2 + rp \\ r\rho V_x V_\theta \\ r\rho V_x V_r \\ rV_x(\rho e_t + p) \end{bmatrix} + \frac{\partial}{\partial r}\begin{bmatrix} r\rho V_r \\ r\rho V_x V_r \\ r\rho V_\theta V_r \\ r\rho V_r^2 + rp \\ rV_r(\rho e_t + p) \end{bmatrix} = \begin{bmatrix} 0 \\ r\rho F_x \\ -\rho V_\theta V_r + r\rho F_\theta \\ \rho V_\theta^2 + p + r\rho F_r \\ r\rho(F \cdot V + q) \end{bmatrix} \quad (2.2)$$

where

$$\vec{F} = (F_x, F_\theta, F_r) = \vec{F}(\vec{V}(x,\theta,r), x, r) \quad (2.3)$$

and F_x, F_θ, F_r, q are the body force and heat source terms. The units of these terms are force or heat release per unit volume.

The above equation set is derived through the following steps:

1. Transform Equation 2.1 into the blade row relative frame (rotating frame for the rotor) using

$$\frac{\partial}{\partial t}|_{stationary} = (\frac{\partial}{\partial t} - \Omega\frac{\partial}{\partial \theta})|_{bladerow} \tag{2.4}$$

2. Remove all $\partial / \partial\theta$ terms in the equation set;
3. Transform the equation back to the stationary frame using

$$\frac{\partial}{\partial t}|_{bladerow} = (\frac{\partial}{\partial t} + \Omega\frac{\partial}{\partial \theta})|_{stationary} \tag{2.5}$$

The first two steps are to get the axisymmetric flow equation set in the frame fixed on the blade row. The equation set is then transformed to the stationary frame.

The operator $\partial / \partial t + \Omega\partial / \partial\theta$ in Equation 2.2 is the result of the transformation of $\partial / \partial t$ from the relative frame to the stationary frame. The $\Omega\partial / \partial\theta$ represents the effects of the flow field moving with the rotor and is viewed from the stationary frame. In the momentum equations, the corresponding terms are referred to as the inertia terms.

If there is no additional heat source in the fluid, the energy exchange between fluid and outside is through the blade force; therefore the source term in the energy equation is the work done by the rotor blade row and can be expressed as

$$F \cdot V + q = F_\theta \Omega r \tag{2.6}$$

where Ω is the rotating speed of the blade row, and F_θ the net tangential body force.

2.1.3 Plenum and Throttle

Following the treatment by Greitzer for a one-dimensional model, the fluid in the plenum is considered as uniform and isentropic. The dynamics of the plenum can be described by the following equation

$$\frac{dP}{dt} = \frac{\gamma P}{\rho V_{plenum}}(m_c - m_t) \tag{2.7}$$

where m_c is the mass flow rate from the compressor and m_t the mass flow rate through the throttle, and V_{plenum} is the volume of the plenum.

The throttle pressure drop is given as

$$\frac{P - P_{ambient}}{\rho U^2} = K_t \phi^2 \tag{2.8}$$

since the plenum has little effect on the early development of short wavelength disturbances, the plenum volume can be set to zero. Thus the governing equation for plenum and throttle becomes:

$$\frac{P_{exit} - P_{ambient}}{\rho U^2} = K_t \phi^2 \tag{2.9}$$

where P_{exit} is the static pressure at the exit of the computation domain.

2.2 Formulation of Body Force

The general idea of body force formulation of blade row can be found in the reference by Marble [10]. The formulation in Gong [9] focuses on those aspects that represent the response to unsteady three-dimensional flow, the most important feature in the flow situations of interest here. The key idea is to let body force field respond to local flow properties instantaneously. The body force formulation (i.e. the way body force responds to local flow properties) is determined based on steady flow field. This type of body force formulation has been shown to be adequate for simulation of stall inception through short wavelength disturbances (chapter 3.4 of Gong [9])

2.2.1 A Form of Body Force for Representing a Blade Passage

The force normal to the blade surface is associated with the blade pressure difference between pressure side and suction side; while the force parallel to the blade surface is associated with the viscous shear.

A key aspect of the formulation is to express the body force as a function of local flow properties. To elucidate the functional dependency of body force on local flow properties, it is useful to examine flow in a straight channel which is, in a first order approximation, similar to flow in a blade passage. A sector of a blade passage is considered as a straight channel, and the flow properties at a particular location are indicated in Fig. 2.2.

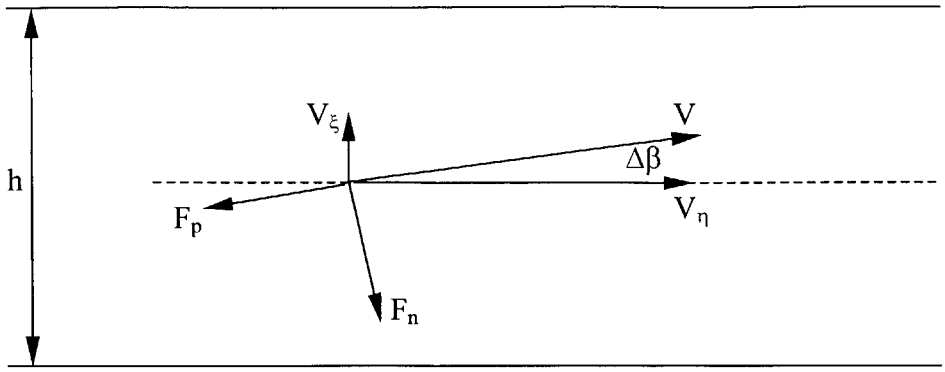

Fig. 2.2 Flow in a blade passage is modeled locally as a flow in a straight channel

The force can be expressed as

$$\frac{hF}{\rho V^2} = f(M, \Delta\beta, \mathrm{Re}) \tag{2.10}$$

where $V, M, \Delta\beta$ and Re are local velocity, mach number, relative flow angle and Reynolds number respectively. h is the local spacing of the blade passage. For high enough Re, the viscous effect is negligible, therefore an adequate form of the body force is

$$\frac{hF}{\rho V^2} = f(M, \Delta\beta) \tag{2.11}$$

Following the analysis of Marble, it is useful to split the body force into two parts: one normal to the relative flow direction annotated as F_n, the other parallel to the flow direction in the relative frame. An advantage of splitting the body force representation into these two parts is that each part can be formulated on its own physical meaning. F_n represents the effects of pressure difference between the pressure surface and suction surface, which enables work exchange between fluid and blade row. The body force parallel to the flow, F_p, is due to the viscous shear stress. The functional dependence of the body force can be written as

$$\frac{hF_n}{\rho V^2} = f_n(M, \Delta\beta) \tag{2.12}$$

$$\frac{hF_p}{\rho V^2} = f_p(M, \Delta\beta) \tag{2.13}$$

So the body force formulation is reduced to the task of determining f_n and f_p at every spatial point in each blade row.

The pressure gradient in a staggered channel could also produce pressure difference across the blade, as shown in Fig. 2.3. The pressure gradient in a staggered blade passage is different from the axisymmetric assumption which states that the pressure gradient is in the direction of the meridional plane. The force term which corresponds to the local pressure gradient is

$$F_n = \frac{1}{\rho}\frac{\partial p}{\partial x}\sin\alpha \tag{2.14}$$

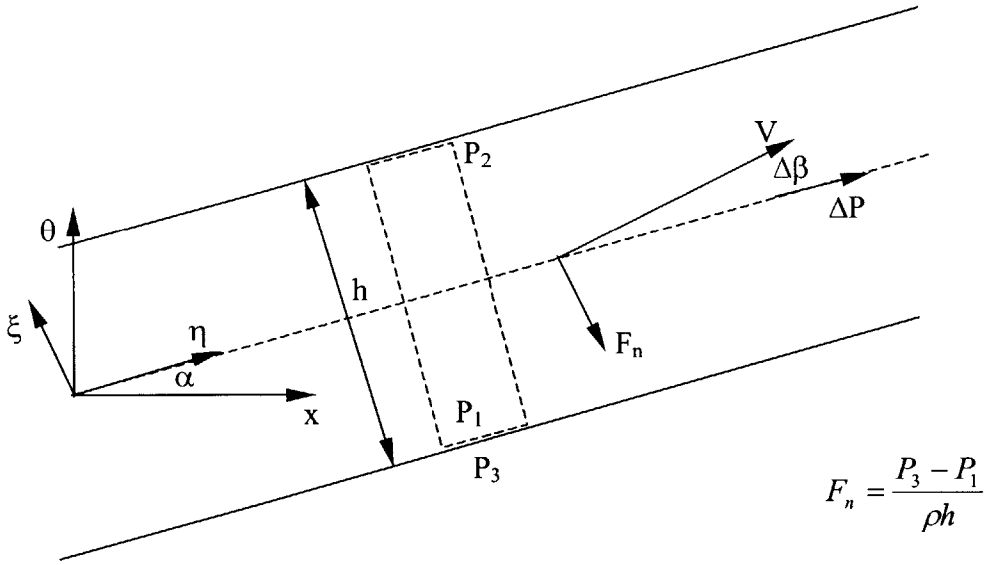

Fig. 2.3 Body force due to pressure gradient in a staggered channel. The velocity is along the blade passage; and the pressure gradient is also in the blade passage direction. The pressure gradient has a component in circumferential direction, so it creates the pressure difference (P_3-P_1) across the blade.

2.2.2 Body Force Formulation Proposed in Gong [9]

The formulation proposed in Gong [9] yield a body force that represents the blade response to the discrepancy between blade metal angle and flow direction. The flow in a blade passage is locally modeled as flow in a straight channel, as shown in Fig. 2.3 η and ξ are the axes in the local blade channel direction and the direction normal to the local blade channel respectively.

The ξ momentum equation can be written as

$$V_\eta \frac{\partial V_\xi}{\partial \eta} = F_{n,\xi} \tag{2.15}$$

Therefore, the normal to blade passage component of the normal body force has the following form

$$F_{n,\xi} \sim \frac{V_\eta V_\xi}{h} \tag{2.16}$$

In the above expression, h is preferred to the blade chord since h can be defined locally. Using the functional form of Eq. 6.4, the $F_{n,\xi}$ can be expressed as

$$F_{n,\xi} = K_{n,\eta}(\Delta\beta, M)\frac{V_\eta V_\xi}{h} \tag{2.17}$$

An undesirable difficulty associated with above formulation is when $\Delta\beta$ reaches 90^0

$$F_{n,\eta} = F_{n,\xi}\tan(\Delta\beta) = K_{n,\xi}(\Delta\beta, M)\frac{V_\xi^2}{h} \tag{2.18}$$

which has a finite value. This can not be right since $F_{n,\eta}$ must be zero in this situation.

To overcome this, the formulation is modified to:

$$F_n = K_n(\Delta\beta, M)\frac{V_\eta V_\xi}{h} \tag{2.19}$$

The above form is nearly equivalent to the original form when $\Delta\beta$ is small since

$$F_{n,\xi} = \cos\Delta\beta F_n \tag{2.20}$$

and it will not be zero if V_η becomes zero.

Upon applying the above formulation in a blade passage where the local blade passage (a straight channel) is along the local blade metal angle, α, we have

$$F_{n,x} = F_n \sin(\alpha + \Delta\beta) \tag{2.21}$$

$$F_{n,\theta} = -F_n \cos(\alpha + \Delta\beta) \tag{2.22}$$

The final results of normal body force can be written as:

$$F_{n,x} = \frac{K_n(\Delta\beta, M)}{h}\frac{V_\theta}{V}(V_x\cos\alpha + V_\theta\sin\alpha)(V_\theta\cos\alpha - V_x\sin\alpha) \tag{2.23}$$

$$F_{n,\theta} = -\frac{K_n(\Delta\beta, M)}{h}\frac{V_x}{V}(V_x\cos\alpha + V_\theta\sin\alpha)(V_\theta\cos\alpha - V_x\sin\alpha) \tag{2.24}$$

Where K_n is the normal body force coefficient.

The expressions for viscous shear force is against the flow direction, and can be written as

$$F_{p,x} = -\frac{K_p(\Delta\beta, M)}{h} VV_x$$

$$F_{p,\theta} = -\frac{K_p(\Delta\beta, M)}{h} VV_\theta \tag{2.25}$$

$$F_{p,r} = -\frac{K_p(\Delta\beta, M)}{h} VV_r$$

Where K_p is the parallel body force coefficient. The resultant parallel body force is the vector sum of all these terms.

A significant feature of the current body force representation is that it is a function of local flow properties. This is essential to model non-linear three-dimensional disturbances in compressors where flow redistribution occurs in a blade row in the presence of these disturbances.

2.3 Numerical method

The governing equations of this body force formulation are three-dimensional unsteady Euler equations. The solution procedure for the governing equations for the compressor model is based on a standard finite volume discretization and a multi-stage Runge-Kutta method for time discretization [22].

The flows within blade row and duct regions are compatible with one another in the computational domain. This will be demonstrated in the following. Fig. 2.4 shows the fluxes through a computational cell in the blade row region. The role of blades is to block (or force) the fluxes through the constant θ face (in the shadowed area). More specifically, if the cell is in a stator blade row, there is no flux through that face, and if the cell is in a rotor blade row, the flux is evaluated using $\Omega\frac{\partial}{\partial\theta}U$. The term can be viewed as the mass and momentum that are forced into the cell by the moving blades. The fluxes on the other faces can be evaluated in the way used by Jameson [22]. The interface between blade row region and duct region is the constant r face; the fluxes on

that face can be evaluated by the same method as is for the three-dimensional flow region. Thus coupling the two types of flow region will not cause any incompatibility problem.

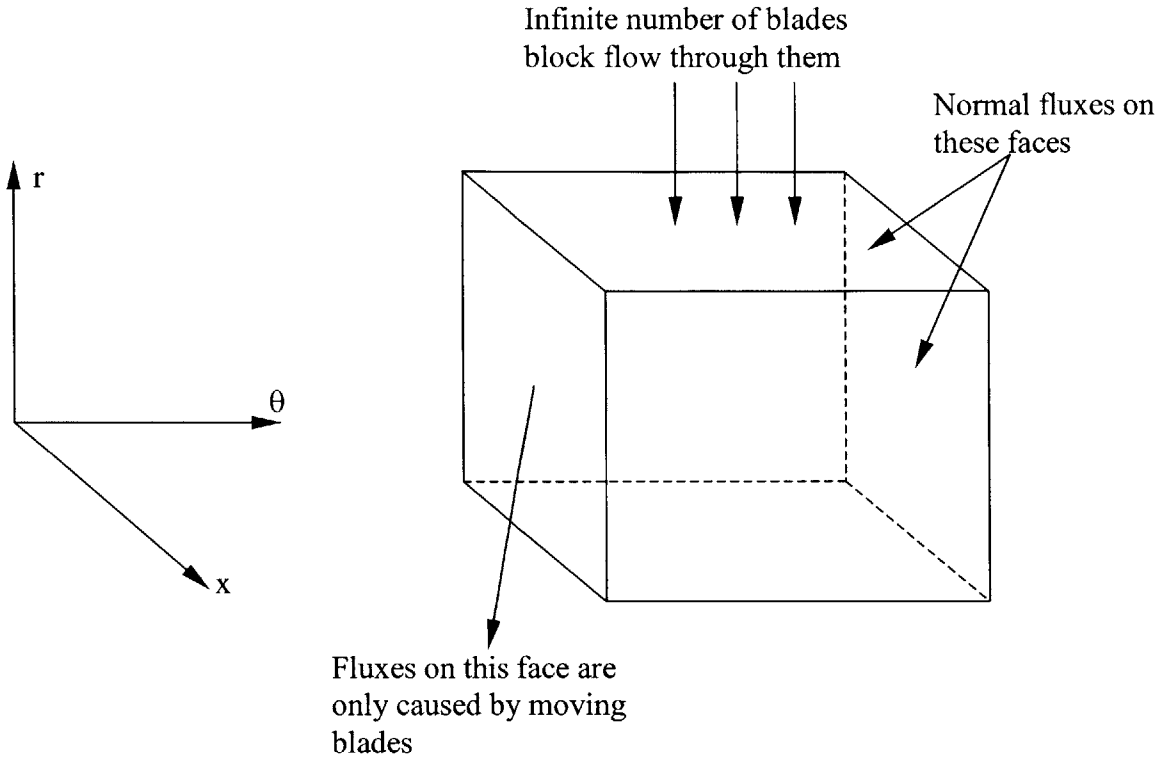

Fig. 2.4 Illustration of fluxes evaluation around a cell in the blade row region

The inlet and exit boundary conditions are standard one-dimensional linearized boundary conditions [28]. The exit static pressure of the computational domain is updated every iteration using the plenum-throttle equation.

2.4 Summary

The non-linear three-dimensional computational model for high-speed compressors which was developed in Gong [9] has been introduced and briefly summarized in this chapter. The key aspect of the model is to emphasize the three-dimensional compressor blade row response to general three-dimensional non-linear flow disturbances. The model has proved to be adequate in simulating compressor response to different types of inlet distortions in Gong [9]. However, its adequacy has not been assessed in terms of

capturing the instability behavior in high-speed compressors, this motivates and constitutes the main work of chapter 3.

Chapter 3

Instability Calculation of a High-Speed Compressor

In this chapter, the computational model for high-speed compressors presented in Chapter 2 is used to simulate the instability behavior of a high-speed single stage compressor (NASA stage-35 compressor) for both clean inlet flow and inlet distorted flow. The work is mainly aimed at assessing the adequacy of the computational model in [9] for simulating the instability behavior in high-speed compressors.

This chapter is arranged as follows: Section 1 briefly introduces the research compressor. Section 2 shows the instability calculation results using the body force formulation in Gong [9]. Section 3 compares the computational results with the experiment; the observed discrepancies between the computational results and experimental observation are delineated to provide motivation for the work described in chapter 4. Section 4 gives a summary of this chapter.

3.1 NASA Stage 35 Compressor

NASA Stage 35 is a single stage transonic compressor designed by NASA Glenn Research Center in the late 70's [12]. The compressor features low aspect ratio rotor and stator blades and a high design pressure ratio of 1.82. The design parameters are listed in Table 3.1. The rotor and stator of this compressor are shown in Fig. 3.1.

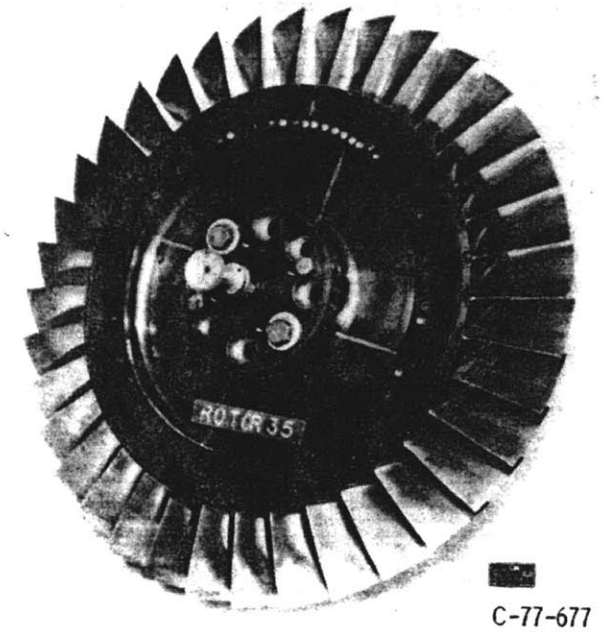

Rotor

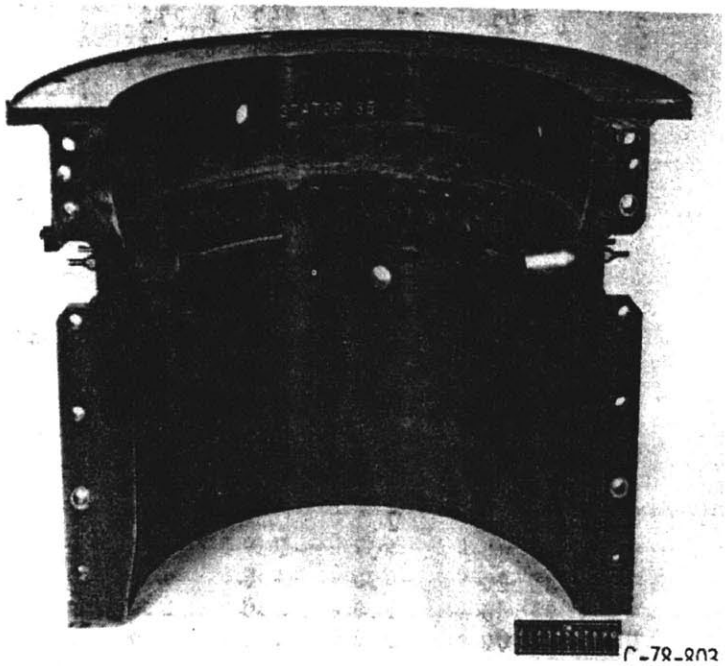

Stator

Fig. 3.1 Rotor and stator of NASA Stage-35 compressor

Number of rotor blades	36
Rotor rotating speed	1800 rad/sec
Rotor aspect ratio	1.19
Hub-to-tip ratio at rotor inlet	0.7
Solidity of rotor	1.29 at tip 1.77 at hub
Number of stator blades	46
Stator aspect ratio	1.26
Solidity of stator	1.3 at the tip 1.5 at the hub

Table 3.1 Design parameters of Stage 35 Compressor

The computational domain is shown in Fig. 3.2

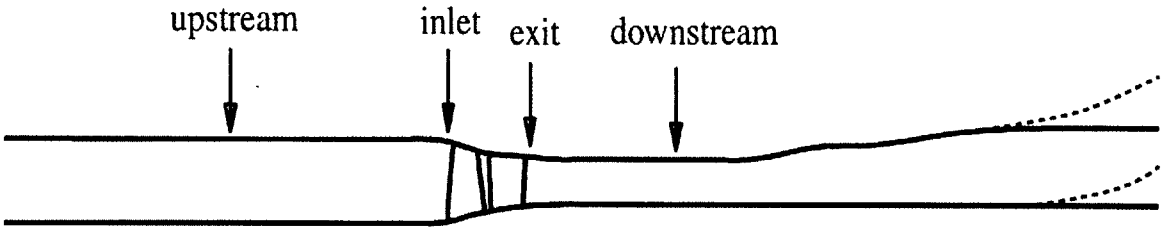

Fig. 3.2 Computational domain of NASA stage 35 compressor

The only difference between the configuration shown and actual experimental configuration setup is that near the exit, the flow path has been modified to avoid any numerical difficulties due to reverse flow at the hub-wall curvature (shown by dashed line). Fig. 3.3 and Fig. 3.4 show the computational mesh in meridional plane and compressor inlet face respectively.

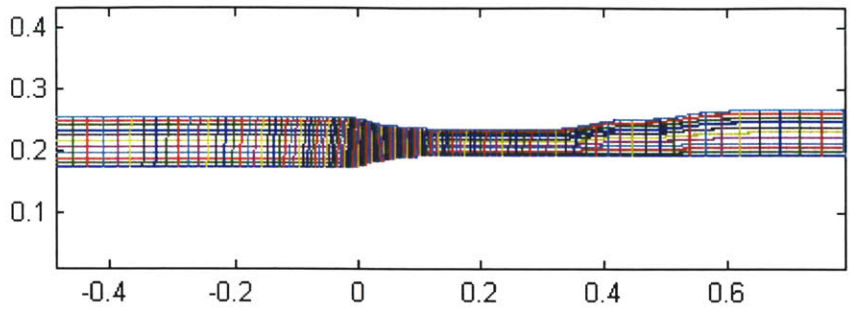

Fig. 3.3 Computational mesh in meridional plane

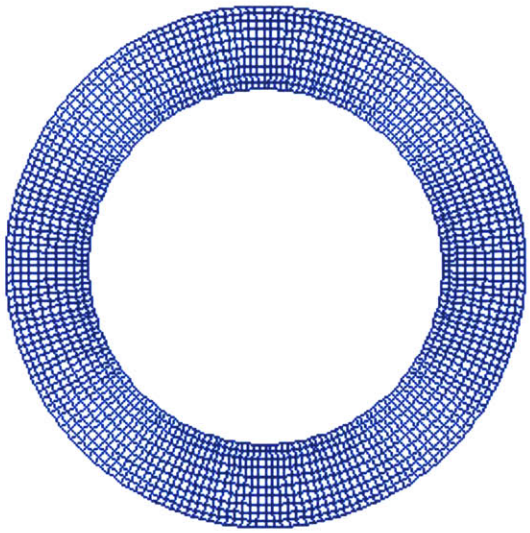

Fig. 3.4 Computational mesh at inlet face

The grid number used in the calculation is 129(axial), 200(circumferential), 10(radial), The large grid number of 200 in the circumferential direction is needed to resolve any stall inception that are associated with short length scale flow disturbances.

3.2 Instability Calculations

Instability calculations have been carried out based on Stage 35 configuration for both clean inlet flow and inlet distorted flow and they are described in this section. These calculations are aimed at simulating stall inception process of the research compressor and the effect of inlet distortion on compressor stability. The expressions for the body force representation of blade row are given as [9]:

$$F_{n,x} = \frac{K_n(\Delta\beta, M)}{h}\frac{V_\theta}{V}(V_x\cos\alpha + V_\theta\sin\alpha)(V_\theta\cos\alpha - V_x\sin\alpha) \qquad (3.1)$$

$$F_{n,\theta} = -\frac{K_n(\Delta\beta, M)}{h}\frac{V_x}{V}(V_x\cos\alpha + V_\theta\sin\alpha)(V_\theta\cos\alpha - V_x\sin\alpha) \tag{3.2}$$

$$F_{p,x} = -\frac{K_p(\Delta\beta, M)}{h}VV_x$$

$$F_{p,\theta} = -\frac{K_p(\Delta\beta, M)}{h}VV_\theta \tag{3.3}$$

$$F_{p,r} = -\frac{K_p(\Delta\beta, M)}{h}VV_r$$

Where K_n and K_p are the body force coefficient in direction normal and parallel to flow respectively. In this chapter, the body force coefficients used in this section is the same as that used in Gong [9], which were correlated based on Rotor 35 geometry at the mid-span and tip location, using loss and deviation data from a standard reference [11] at design mass flow, they are

$$K_n = 4.2 - 3.3\alpha$$

$$K_p = 0.04$$

where α is the metal angle of the compressor blades. As shown in Fig. 3.5 and Fig. 3.6, the resultant body force representation of stage-35 rotor yields a spanwise distribution of deviation and loss coefficient that are in accord with the data at design operating point.

Having obtained the body force formulation, there are three issues regarding compressor instability calculations that need to be addressed:

1. Initial disturbances
2. Determination of stall point
3. Characterization of stall inception type

They are further elaborated next.

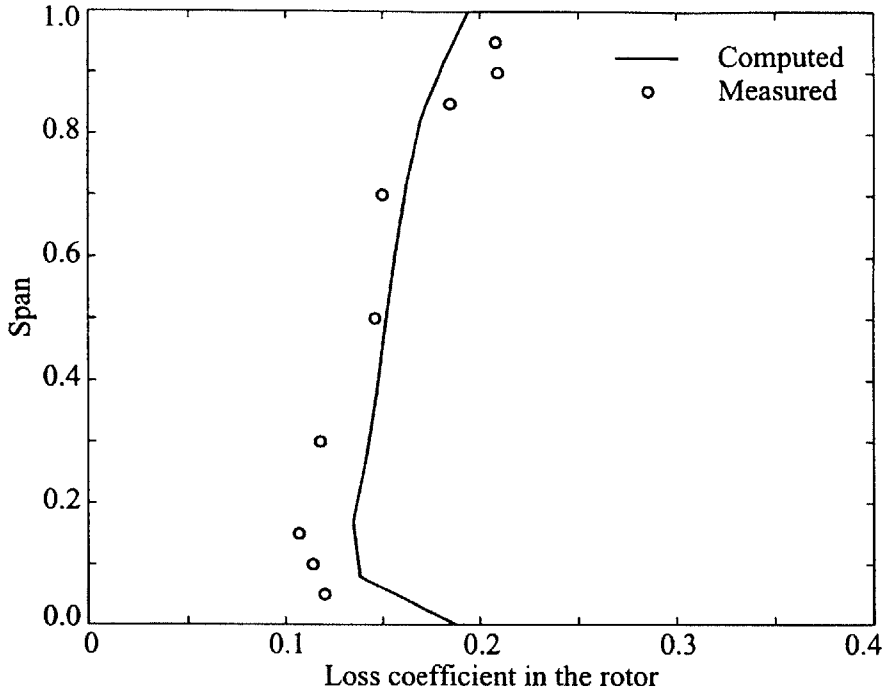

Fig. 3.5 The computed and measured loss coefficient profile of Rotor 35 at 100% rotational speed and 20.2 kg/sec mass flow rate [9].

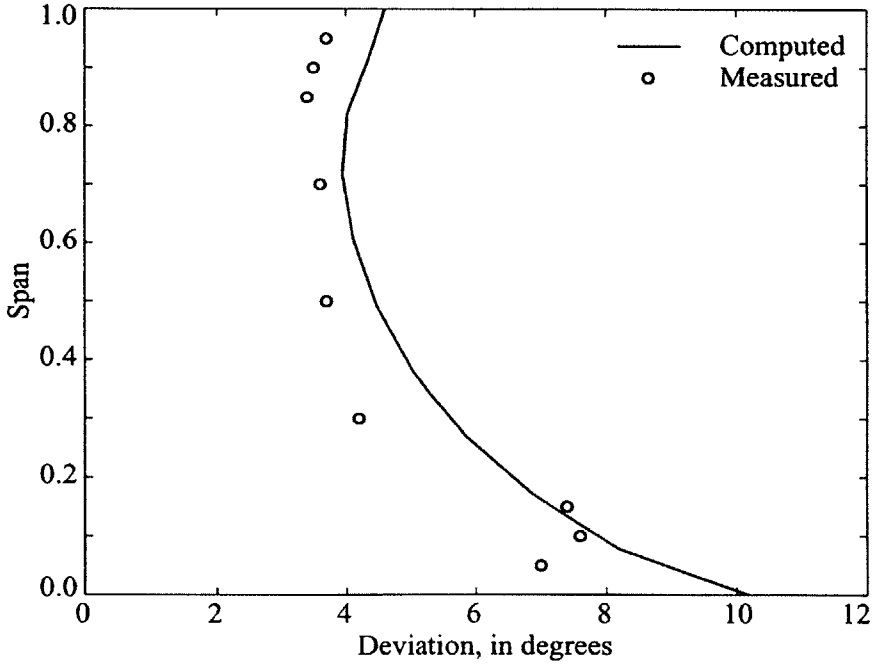

Fig. 3.6 The computed and measured deviation angle of Rotor 35 at 100% rotational speed and 20.2 kg/sec mass flow rate [9].

Initial Disturbances

Any instabilities have to be initiated from background disturbances which would normally be absent in computations; therefore for clean inlet flow, disturbances have to be part of the input in the computational model. There are two types of disturbances that are used in the simulations. Short wave length disturbances are generated by imposing an axial force impulse in the tip region of a selected blade row. Long wavelength disturbances, consisting of a two-dimensional disturbance extending through the whole compressor, are imposed as an initial condition. The amplitude of the long wavelength disturbances is always less than 1% of the mean velocity. For the above cases with clean inlet flow, the disturbances are imposed on the steady flow field and the determination of whether the imposed disturbance will grow or decay is implemented with the throttle fixed at varying settings.

Determination of the Stall Point

Once the disturbances are imposed on a steady flow field, its development determines if the compressor flow field is stable. If the disturbances decay, then the flow in a compressor is stable, and a similar simulation at a lower flow coefficient will be performed. The instability point is determined by repeating the above simulation until the imposed disturbance no longer decays.

Continuous changing of throttle, which is usually used in experiments, is avoided because any numerically acceptable throttle change rate is much faster than that used in experiments. Thus at each throttle point, simulation is allowed to proceed until the imposed disturbance decays or grows. However, for flow with inlet circumferential distortion, as no additional disturbance is imposed on the steady flow field, the mass flow is continuously decreased to approach the stall point. This is achieved by scheduling the throttling rate to ensure that it is not the fast throttling transient behavior that drives the compression system to instability.

Characterization of Stall Inception Type

The two types of stall inceptions are characterized in the following [40]:

The main features of modal stall inception are:

(i) Long length scale; the length scale of modal wave disturbance is comparable to compressor annulus

(ii) Exponential growth; the growth of different harmonics of the disturbance can be well described by an exponential function of time

(iii) Low rotating speed; the rotating speed of modal wave disturbance is normally in the range 20% to 50% of rotor speed

(iv) Nearly two-dimensional; the modal type inception varies little in spanwise direction and extend through the compressor

In contrast, spike stall inception has the following key distinctive characters:

(i) Short length scale; the length scale of spike stall inception is about 2~3 blade pitches

(ii) Non-linear phenomenon; the growth of spike disturbance is thought to be associated with separation and three-dimensional flow redistribution

(iii) High rotating speed; the rotating speed of spike disturbances is about 70% rotor speed

(iv) Three-dimensional phenomenon; the spike stall inception is observed to be confined to blade tip region and there is considerable spanwise variation

These characteristic features for the two different types of stall inception described in the above constitute the basic criteria for discriminating one type of stall inception process from the other.

3.2.1 Clean Inlet Flow

Instability calculations were performed and they are described in this section with an emphasis on characterizing the compressor instability behavior in a high-speed compressor for clean inlet flow. Two kinds of disturbances are imposed on the steady flow field. One is short wave length disturbance imposed on the flow in rotor tip region, the other is long wavelength disturbances that extend through the whole compressor. The calculations are aimed at delineating the stall inception process.

a. Short wave length disturbance imposed on the flow in rotor tip region

In this simulation, the short wave length disturbances, generated by imposing an axial body force impulse, are imposed on the flow in the tip region of the rotor. The duration for which the force impulse is imposed on lasts for about 0.1 rotor revolutions (this value is chosen to be much shorter than the time scale of stall inception). During this period, the imposed disturbances are rotating with the same speed as rotor and the axial body force in the rotor tip region is set to zero. The circumferential extent of the impulse is about one blade passage, corresponding to the collapse of flow in one local blade passage.

The detailed calculation procedure is as follows:

For a steady flow field from axisymmetric calculation, impose the short wavelength disturbance on the flow field and observe its development. If the disturbance decays, a similar simulation at a lower mass flow is performed. This process is repeated until the disturbance no longer decays.

Fig. 3.7 shows the axial velocity disturbance traces in rotor tip exit when mass flow through the compressor decreases to 7.97 kg/s (flow coefficient ϕ=0.22). The spike-shaped disturbance is seen to be suppressed almost immediately after it is inserted into the system and the compressor stalls through long wavelength disturbances. The Fourier spectrum of the disturbances, as shown in Fig. 3.8, shows clearly that the dominant harmonics in the stall inception process are the 8^{th} and 9^{th} harmonics.

Fig. 3.9 gives the Fourier component of axial velocity disturbance corresponding to t=22.8 rotor revolutions, showing the dominance of 8^{th} and 9^{th} harmonics in agreement with the results in Fig. 3.8. Fig. 3.10 shows the flow coefficient contour on the rotor exit, where a disturbance dominant in 9 harmonics content can be clearly identified in the

compressor annulus. In summary, all the above analysis shows that the dominant harmonics in stall inception process are the 8^{th} and 9^{th} harmonics.

2. Modal wave disturbance imposed throughout the whole flow field

Sinusoidal axial velocity disturbance is imposed throughout the whole compressor on the mean flow field as initial condition. The amplitude of the sinusoidal oscillation is less than 1% of the mainstream velocity in axial direction.

Fig. 3.11 shows the axial velocity disturbance traces in rotor tip inlet when the mass flow through the compressor is decreased to 7.8 kg/s (flow coefficient ϕ=0.216). Similar to the case where spike-shaped disturbance is imposed on, the computed results show clearly that the disturbance is growing through a modal wave disturbance. Fig. 3.12 shows the spectrum of Fourier coefficients evolution for the first 15 harmonics, again indicating the dominant role of the 8^{th} and 9^{th} harmonic disturbance in the stall inception process. This can also be seen in the Fourier component distribution of disturbance shown in Fig. 3.13 corresponding to t=22.8 rotor revolutions. Fig. 3.14 show the flow coefficient contour on rotor exit and nine sinusoidal variation can be seen around the compressor annulus; this is also consistent with the Fourier spectrum results of Fig. 3.12 which show that the 8^{th} and 9^{th} harmonics are the dominant harmonics. The small discrepancy in the stalling mass flow for both types of initially imposed disturbances (spike-shaped and modal-shaped) implies that the compressor with the body force formulation in this chapter is a modal-type stall compressor.

3.2.2 Flow with Circumferential Total Pressure Inlet Distortion

Instability calculations are performed in this section for flow with circumferential total pressure inlet distortion. These calculations are aimed at

1) Simulating the instability behavior of the research compressor when background flow is circumferentially non-uniform;
2) Assessing the effect of inlet distortion on compressor instability.

The imposed circumferential total pressure inlet distortion covers a 120 degree sector angle with a distortion amplitude of 1.05 dynamic head.

Fig. 3.15 shows the temporal development of axial velocity disturbance traces in rotor tip inlet upon further throttling from a mean flow of 8.5 kg/s. An apparent velocity deficit can be seen to first occur at the time instant corresponding to 6.2 rotor revolutions. The compressor was found to have stalled by examining the flow field at that time instant. Velocity traces subsequent to time instant corresponding to 6.2 rotor revolutions show finite number of stall cells rotating around the compressor annulus.

Fig. 3.16 shows the comparison of compressor characteristics for clean inlet flow and inlet distorted flow. The curve with open circle symbol represents the characteristics with clean inlet flow. The curve with open square symbol is the characteristics for flow with inlet distortion. It is deduced that both the compressor performance and the stability margin deteriorate significantly with inlet distortion.

3.3 Comparison of Computational Results with Experimental Data

In this section, comparison between computational results in this chapter with experimental data is presented. The comparison is aimed at assessing the adequacy of the body force formulation in Gong [9] as described by the expressions in Eq. 3.1~ Eq. 3.3 in simulating compressor instability.

The key differences between computation and measurement and the resulting implications on compressor instability behavior can be summarized as follows:

(1) Stalling mass flow

Fig. 3.17 shows the compressor characteristic for Stage-35 at 70% rotor speed. The computed stalling mass flow is considerably lower than the measured stalling mass flow.

(2) Slope of characteristic line.

As shown in Fig. 3.17, the slope of computed characteristic is substantially different from that of the measured characteristic.

(3) Rotor deviation and loss distribution.

Fig. 3.18 and Fig. 3.19 shows the experimental data for rotor deviation angle and rotor loss coefficient. As mass flow is decreased to near stall point (mass flow=11.8kg/s), there is an increase in the rotor tip region for both rotor deviation angle and loss. By contrast, the computational results in Fig. 3.20 and Fig. 3.21 do not show this trend; the rotor hub region has higher deviation angle and loss.

(4) Stall inception process.

The computational results differ from the experimental investigation in terms of stall inception process: While the computational results for clean inlet flow in this chapter implies that stall inception is through modal wave disturbance that is in agreement with experiment (Fig. 3.22), the results for inlet distorted flow differ from experimental results [46] which show that the stall inception is through initial spike and then modal wave disturbance (see Fig. 3.23).

Based on the above reasons, we deduce that the current body force model is not a good representation of stage-35 compressor at 70% rotor speed in terms of compressor instability behavior.

3.4 Summary

Rotating stall calculations for NASA stage-35 compressor were carried out in this chapter based on the body force formulation given in Eq. 3.1 to Eq. 3.3 (Gong [9]) for both clean inlet flow and flow with circumferential total pressure inlet distortion. The key results in this chapter are:

1. For clean inlet flow, given a spike-shaped disturbance in rotor tip region that lasted for about 0.1 rotor revolutions, the compressor will stall through modal wave disturbance. The dominant harmonics in stall inception process are the 8^{th} and 9^{th} harmonics. The stalling flow coefficient is ϕ=0.221.
2. For clean inlet flow, given a sinusoidal axial velocity disturbance through the whole compressor of amplitude less than 1% of the mainstream velocity, the compressor stalled through the modal wave disturbance. The dominant harmonics in stall inception process are the 8^{th} and 9^{th} harmonics. The stalling flow coefficient is ϕ=0.216.
3. Both the stall inception process in 1 and 2 and the small discrepancy between the stalling mass flow in 1 and 2 indicate that the compressor based on the body force formulation in this chapter is a modal stall type compressor.
4. The comparison between clean inlet flow and flow with inlet distortion indicates that inlet distortion deteriorate compressor performance and degrade stability margin.

The comparison between the computational results and experimental data indicates that the compressor using the body force formulation in Eq. 3.1 to Eq. 3.3 (Gong [9]) differs from stage-35 compressor measurements in the following aspects:

a. Stalling mass flow;
b. Slope of compressor characteristic;
c. Loss and deviation distribution along blade span;
d. Stall inception process;

These differences can be attributed to the fact that the body force formulation provides a valid description of compressor performance at the design operating point rather than the operating conditions at 70% rotor speed. The aspect of the inadequacy will be examined and assessed in chapter 4.

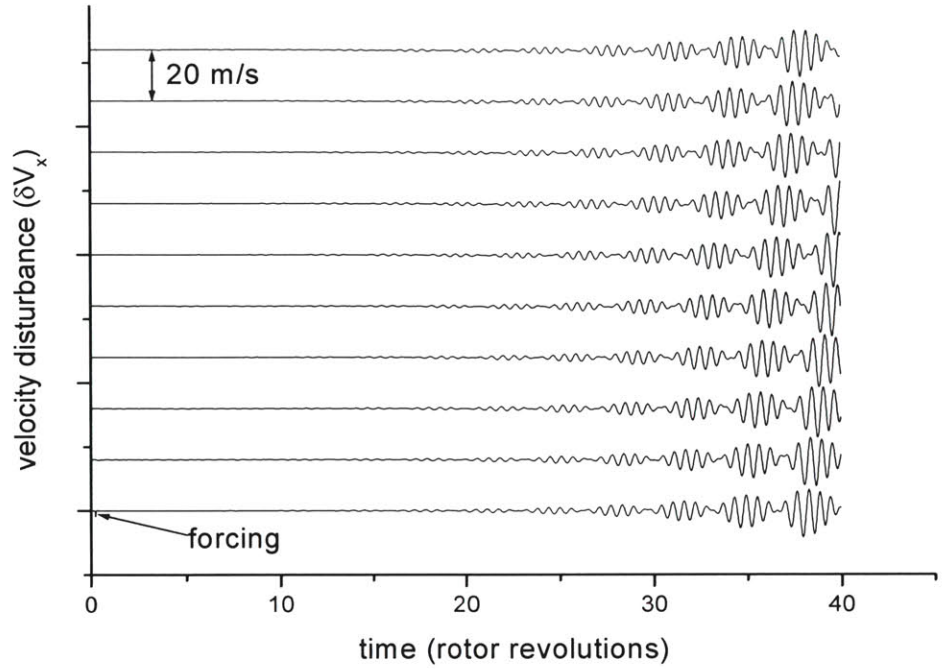

Fig. 3.7 Computed V_x traces in rotor tip exit during stall inception process (spike-shaped disturbance as initial disturbance)

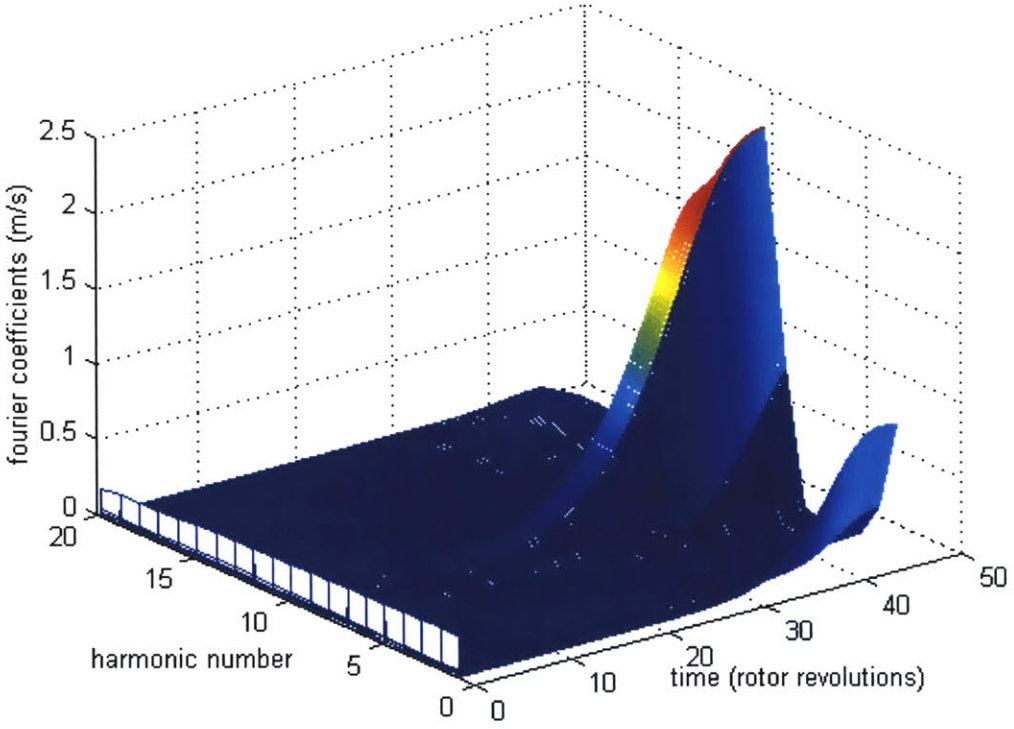

Fig. 3.8 Evolution of Fourier coefficients of computed V_x in rotor tip exit for the first 15 harmonics

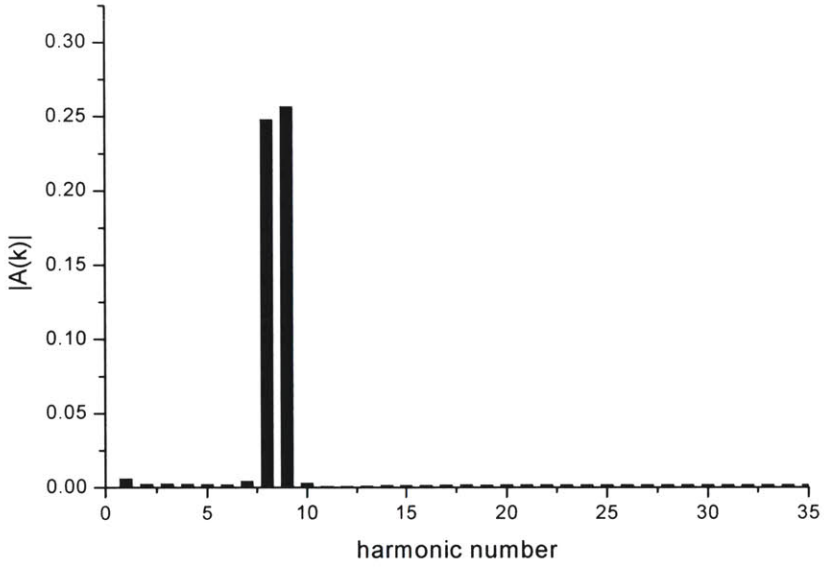

Fig. 3.9 Harmonic distribution for t=22.8 rotor revolutions

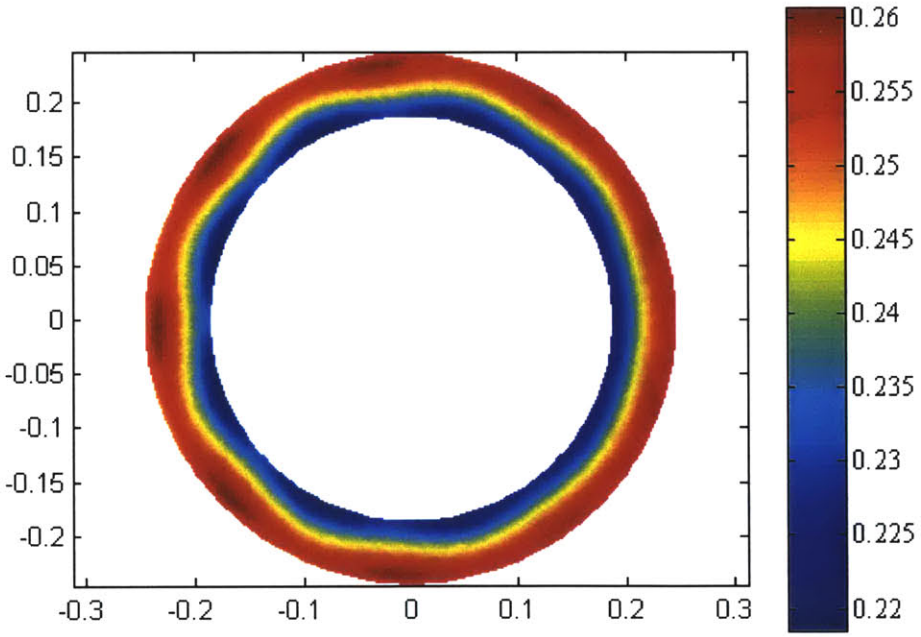

Fig. 3.10 Computed flow coefficient contour on rotor exit plane
(t=22.8 rotor revolutions)

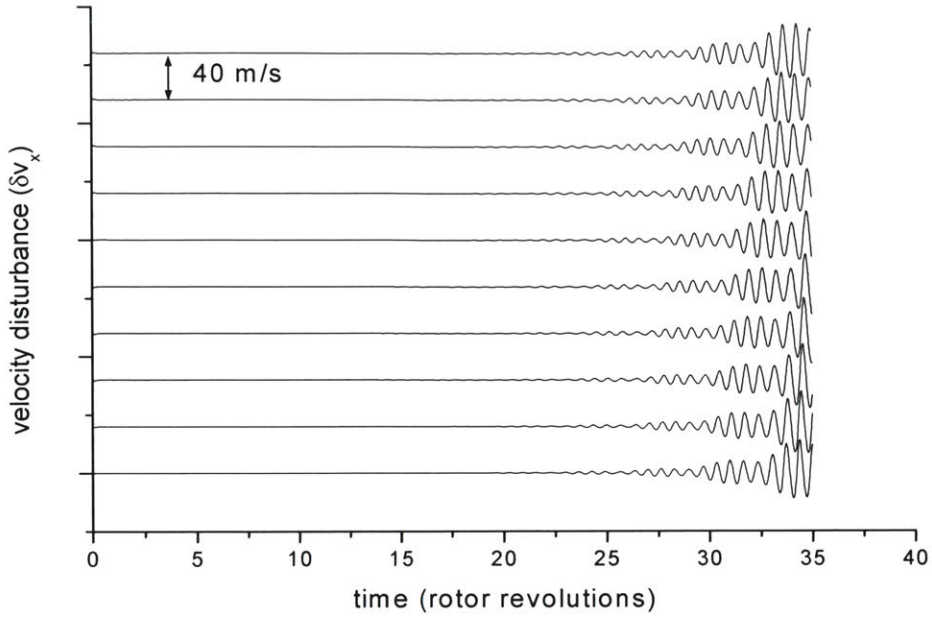

Fig. 3.11 Computed V_x traces at rotor tip exit during stall inception process (long wavelength wave disturbance as initial disturbance)

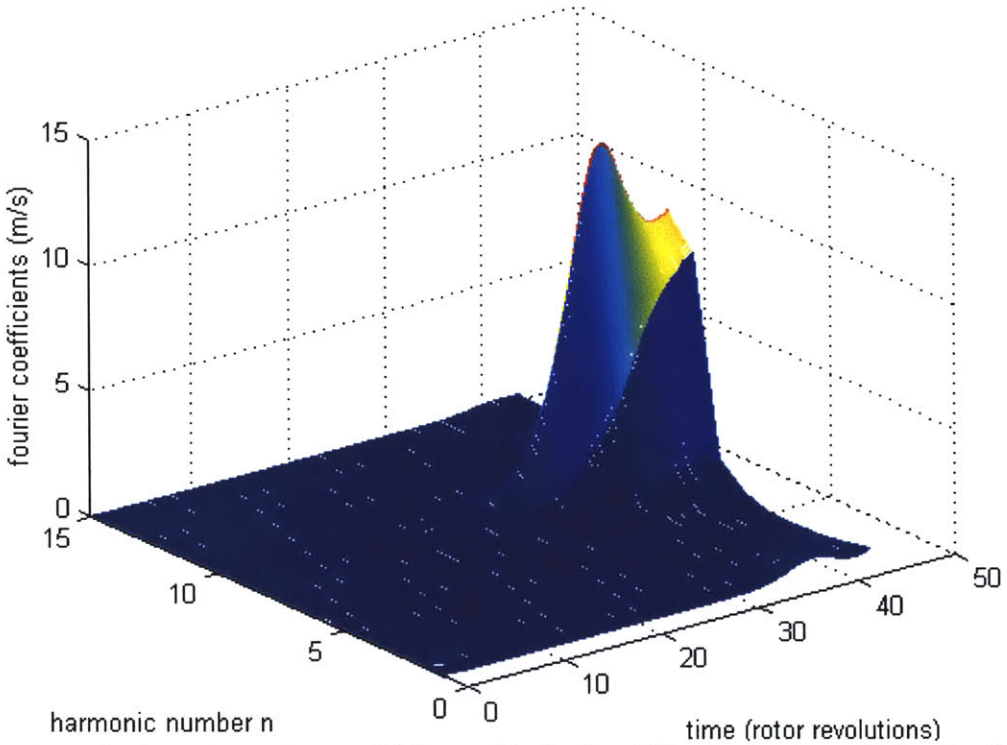

Fig. 3.12 Evolution of Fourier coefficients of calculated V_x at rotor tip exit for the first 15 harmonics

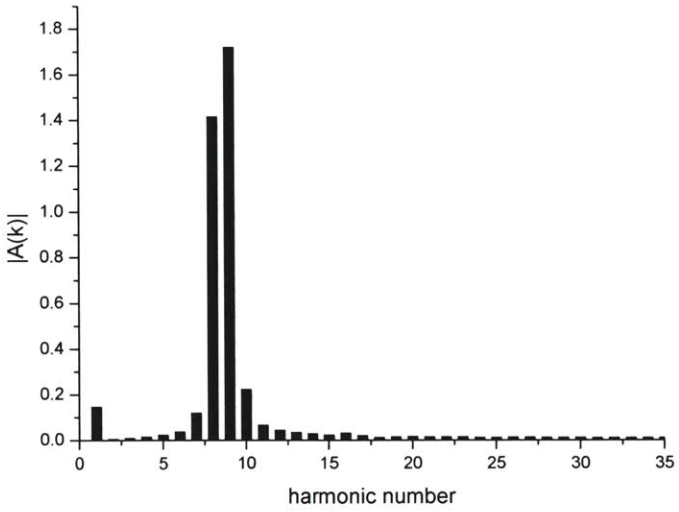

Fig. 3.13 Harmonic distribution for t=22.8 rotor revolutions

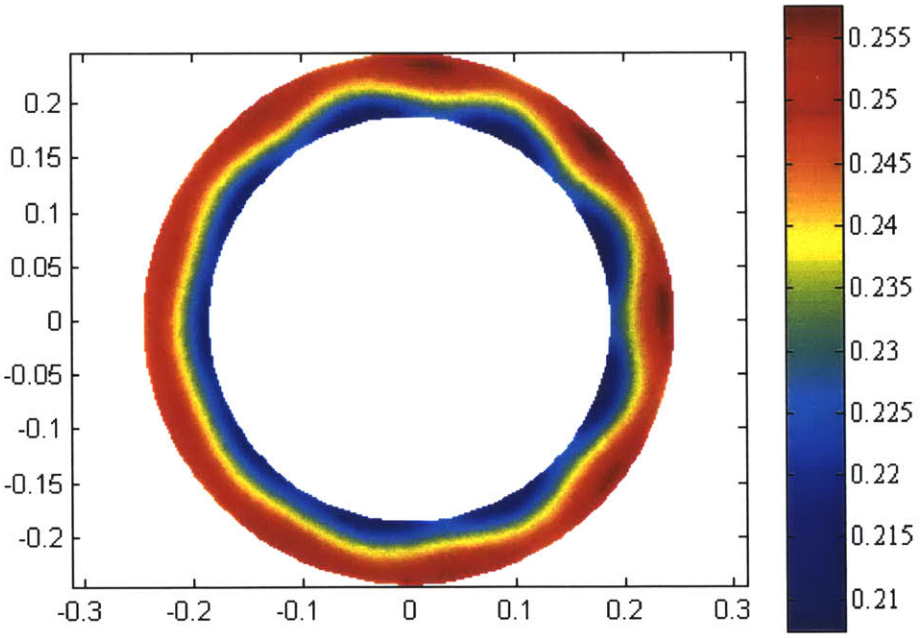

Fig. 3.14 Flow coefficient contour at rotor exit (t=22.8 rotor revolutions)

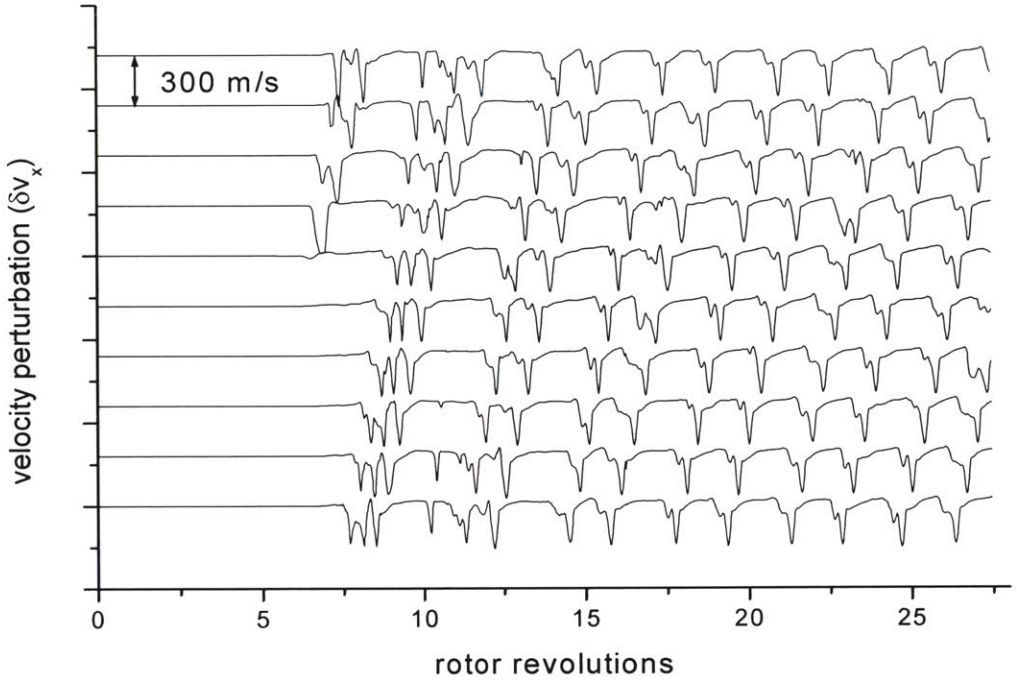

Fig. 3.15 Velocity disturbance traces in rotor tip inlet (flow with inlet distortion)

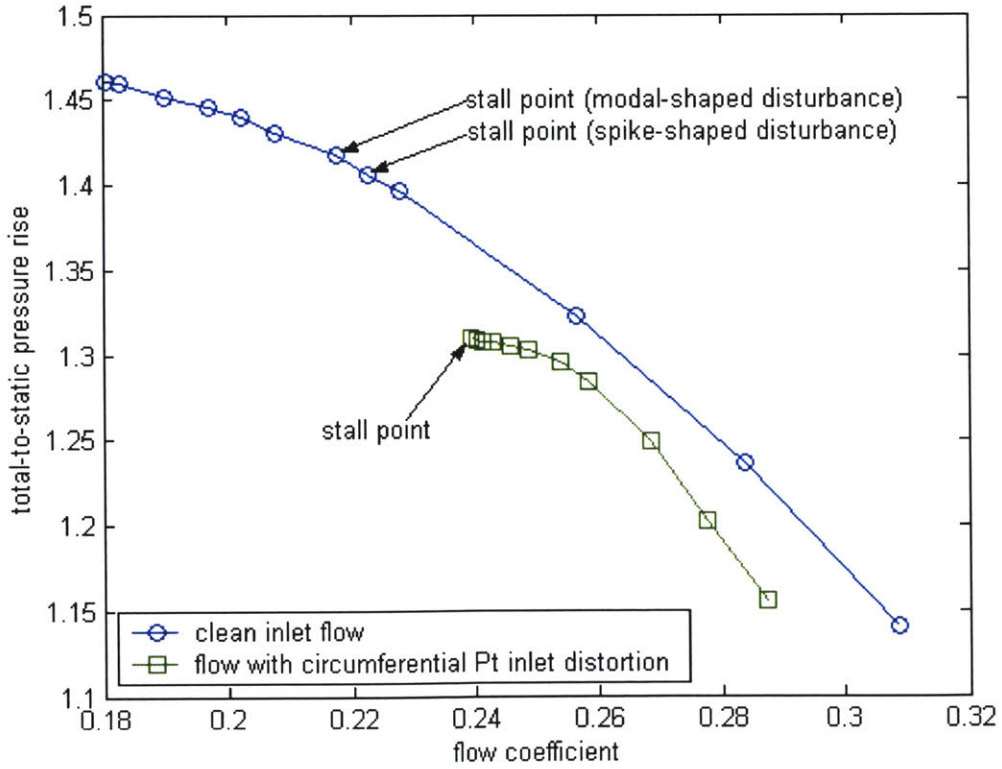

Fig. 3.16 Comparison of compressor characteristic for clean inlet flow and inlet distorted flow

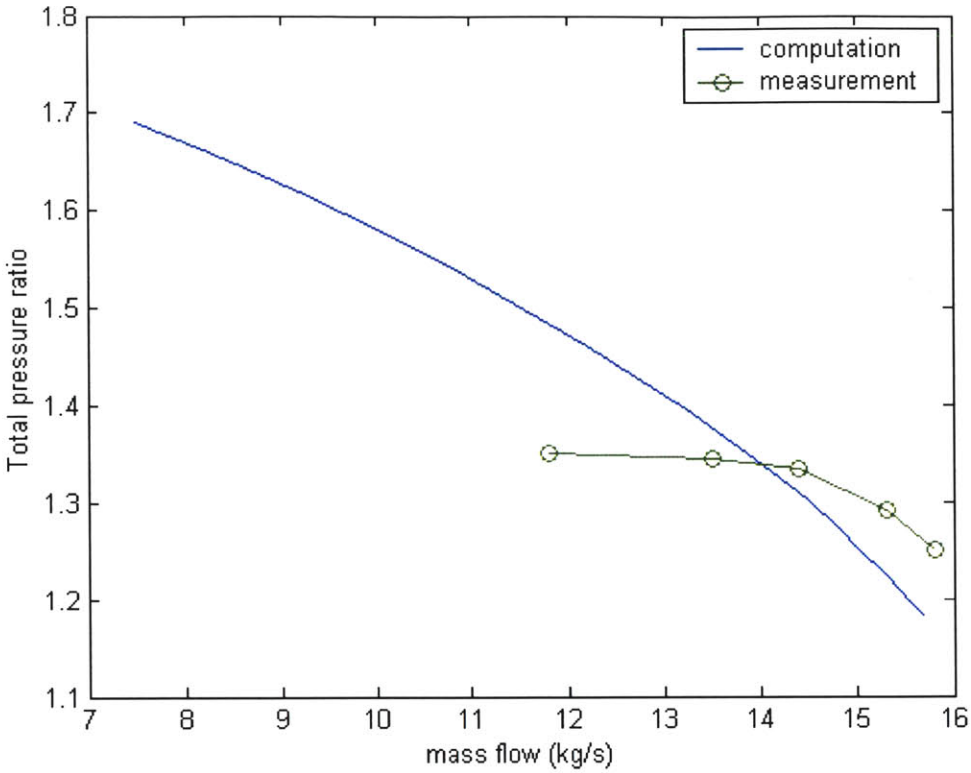

Fig. 3.17 Comparison of compressor characteristics by computation and measurement

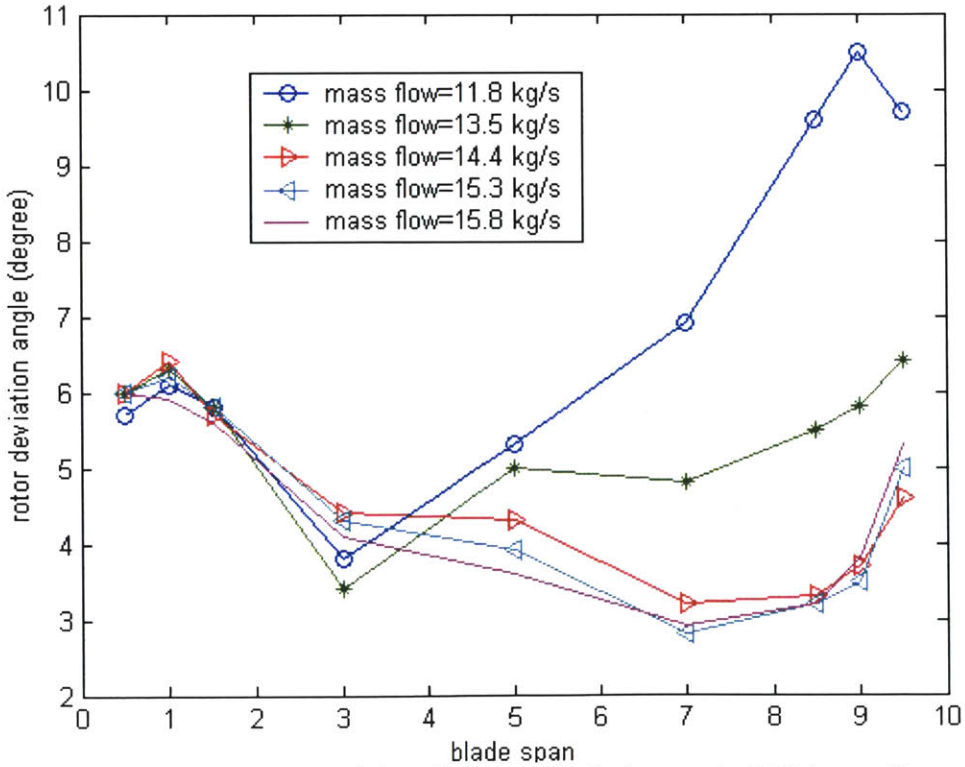

Fig. 3.18 Experimental data for rotor deviation angle (70% speed)

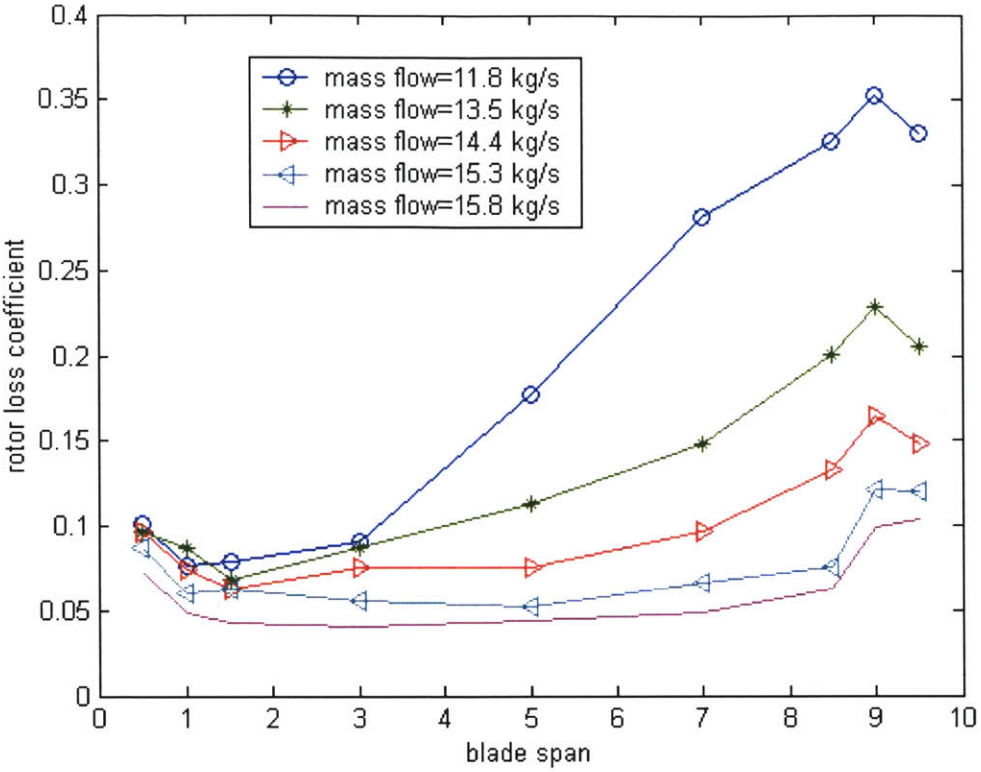

Fig. 3.19 Experimental data of rotor loss coefficient (70% speed)

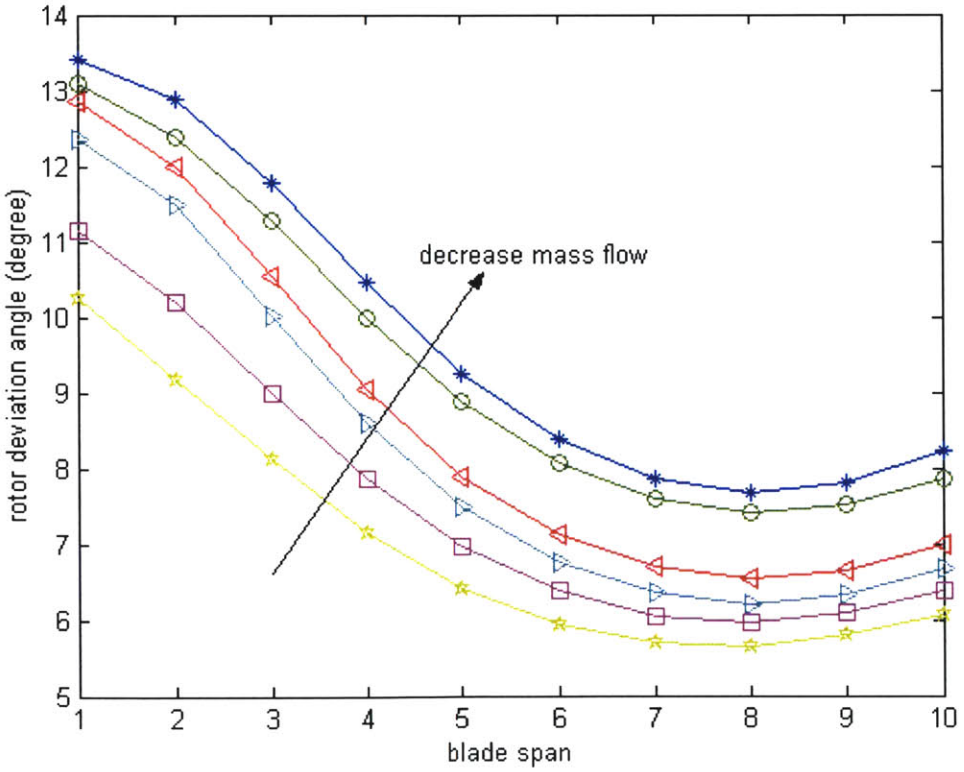

Fig. 3.20 Computational results for rotor deviation angle for different mass flow

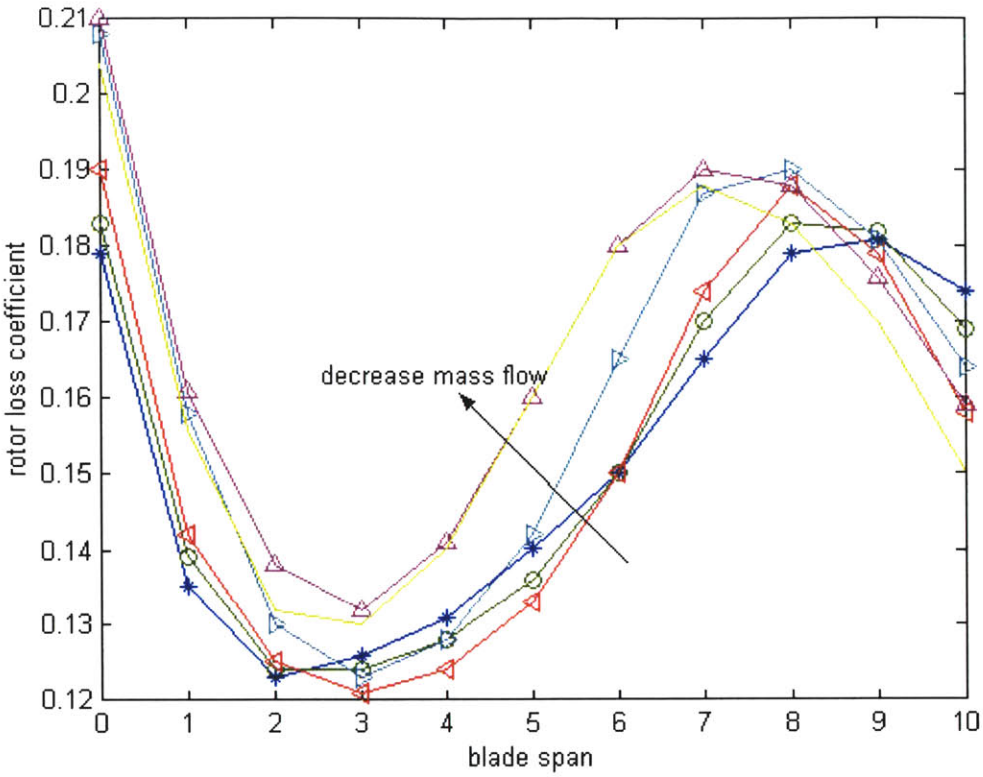

Fig. 3.21 Computational results for rotor loss coefficients for different mass flow

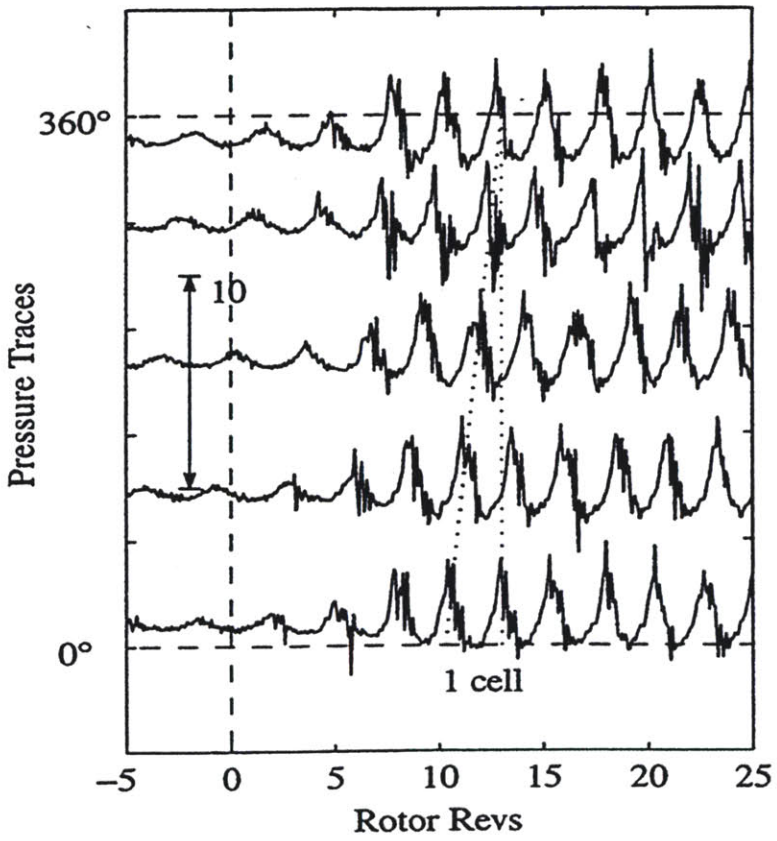

Fig. 3.22 Stall inception process for clean inlet flow in [35]

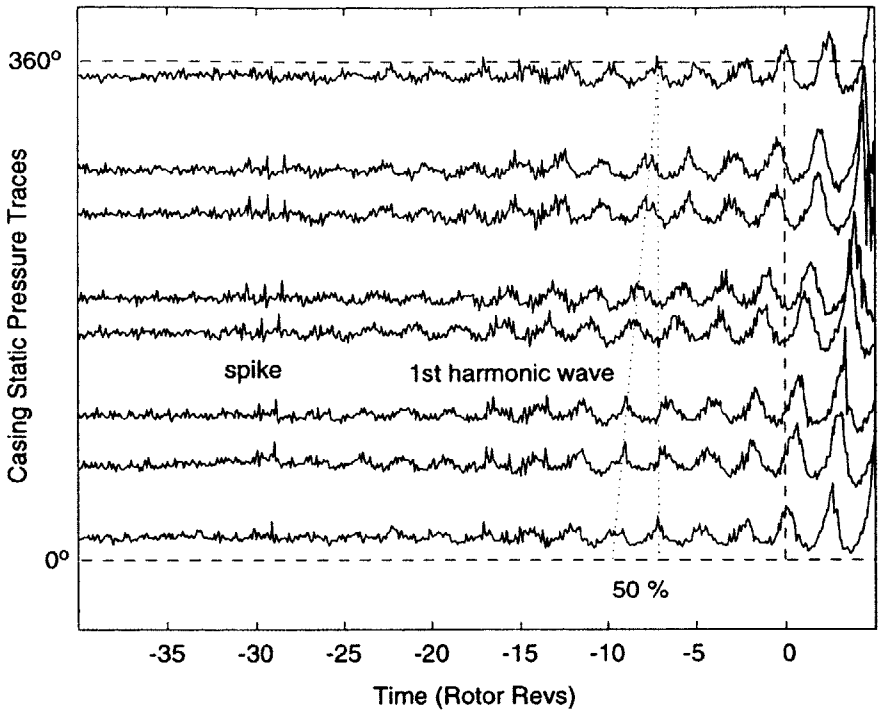

Fig. 3.23 Circumferential inlet distortion without blowing: initial spike and then modal pre-stall behavior [46]

Chapter 4 Body Force Calibration of Stage-35 Compressor and Instability Calculations based on Calibrated Body Force

As summarized in chapter 3, the body force formulation as given in Eq. 3.1 to Eq. 3.3 [Gong (9)] does not constitute an adequate representation of body force formulation for NASA stage-35 compressor for simulating the instability behavior of stage-35 compressor at 70% rotor speed. This motivates the work described in this chapter.

In this chapter, a procedure for modifying the formulation given in Eq. 3.1 to Eq. 3.3 for NASA stage-35 compressor at 70% rotor speed based on the experimental data is proposed. The modification is aimed at capturing the following important aspects related to compressor instability behavior:

(1) Stalling mass flow

(2) Slope of compressor characteristic

(3) Rotor deviation and loss distribution along blade span

(4) Stall inception process

The above aspects related to compressor instability behavior have not been reproduced based on the body force representation presented in chapter 3. In addition, instability calculations based on the modified body force formulation are given to delineate the compressor instability behavior. The issue being examined here is the level of details in the body force representation to enable its adequate description of instability behavior in high-speed compressor.

This chapter is organized as follows: Section 1 presents a procedure of formulating body force from experiments; Section 2 gives the detailed calibration procedure for NASA stage-35 compressor at 70% rotor speed; Section 3 presents the instability calculations using the modified body force formulation. Section 4 provides a summary of this chapter.

4.1 A Procedure for Formulating the Body Force

Based on the suggestion of Gong [9], the body force formulation includes the following two steps: (1) determination of a body force field from a three-dimensional flow in a

blade passage; (2) deducing the body force coefficients as functions of local flow properties. For the details of the calibration method, please refer to Appendix II.

4.2 Body Force Modification

According to the description of body force formulation in Section 4.1, it is expected that the body force be able to respond to local flow conditions and represent the flow field for several operating points on compressor characteristic. The calibrations are aimed at matching the slope of compressor characteristics near stall. In order to achieve the above goal, a calibration procedure is proposed and described in detail in Appendix II. Fig. A.17~ Fig. A.18 show the main results of body force modification, which indicate that the modified body force formulation is able to match the slope of the compressor characteristic near stall. It will be shown later that the resultant body force can match the stalling mass flow.

4.3 Instability Calculations Using the Modified Body Force

Instability calculations with body force formulation calibrated in section 4.2 have been performed in this chapter for both clean inlet flow and flow with inlet distortion. The computations are aimed at:

(1) Assessing the adequacy of the body force formulation calibrated in section 4.2;
(2) Simulating the instability behavior of the research compressor with the body force formulation calibrated in section 4.2;

This section is arranged as follows: Section 1 presents the instability calculations for clean inlet flow; Section 2 gives the instability simulation for flow with circumferential total pressure inlet distortion; Section 3 analyzes the computational results to compare with experimental data; Section 4 explains the advantages of the calibrated body force formulation over the body force formulation contained in Eq. 3.1 to Eq. 3.3 [Gong (9)]

4.3.1 Clean Inlet Flow

I. Spike-shaped disturbance

In this calculation, using a procedure similar to that in chapter 3, a spike-shaped disturbance is imposed on the flow in the rotor tip region. The disturbance rotates with

rotor speed and lasts for about 0.1 rotor revolutions. Fig. 4.1 shows the axial velocity disturbance traces at rotor hub inlet when mass flow through the compressor decreases to 11.94 kg/s (flow coefficient ϕ=0.3387). The spike-shaped disturbance is seen to be suppressed almost immediately after it is inserted into the system and the compressor stalls through long wavelength disturbances. The evolutions of Fourier coefficients of the disturbances, as shown in Fig. 4.2, shows clearly that the dominant harmonics in stall inception process is the 3rd harmonics. Fig. 4.3 shows the Fourier components for t=42.7 rotor revolutions. Again, we can see that the 3rd harmonic is the dominant harmonics. This result is consistent with the results in Fig. 4.2. Fig. 4.4 shows the flow coefficient contour in rotor inlet, where a 3 harmonic sinusoidal flow disturbance can clearly be identified around the compressor annulus. Both of the above computed results show that the stall inception is through modal wave disturbance dominant in 3rd harmonic content.

II. Modal wave disturbances

Sinusoidal axial velocity disturbance is imposed throughout the whole compressor on the mean flow field as initial condition with amplitude of less than 1% of the mainstream velocity.

Fig. 4.5 shows the axial velocity disturbance traces in rotor tip inlet when mass flow through the compressor is decreased to 11.9 kg/s (flow coefficient ϕ=0.338). Similar to the case where a spike-shaped disturbance is imposed upon, the stall inception is through a modal wave disturbance. Fig. 4.6 shows the evolutions of Fourier coefficients for the first 15 harmonics, again it shows that the 3rd harmonics plays a dominant role on stall inception process, which can also be seen in the Fourier component distribution shown in Fig. 4.7 for time instant corresponding to t=35.32 rotor revolutions. This is also consistent with the results in Fig. 4.8 where a 3 harmonic flow disturbance can be clearly identified around the compressor annulus. The small discrepancy in the stalling mass flow for both types of initially imposed disturbances (spike-shaped and modal-shaped) also indicates that the compressor with the calibrated body force formulation in this chapter is a modal-type stall compressor.

The simulation appears to indicate that rotating stall pattern evolves to "ring stall". Fig. 4.9 shows the flow coefficient contour on rotor exit plane during the evolution into

"ring stall" with reverse flow in the hub region. The reason for the final stage of stall development into "ring stall" can be attributed to the fact that the modified body force representation yields a rotor deviation distribution inconsistent with one that show the correct trend with the decreasing mass flow. This can be seen in Fig. 4.10 and Fig. 4.11, which show that in the experiment, with mass flow decreasing to near stall point, an apparent increase in rotor deviation angle in the tip region can be found; while the modified body force does not yield such a trend.

4.3.2 Flow with Circumferential Total Pressure Inlet Distortion

In this section, instability calculations are performed for flow with circumferential total pressure inlet distortion. The distortion pattern is the same as that used in chapter 3: circumferential total pressure inlet distortion covers a sector angle of 120 degrees with the distortion magnitude of 0.035 dynamic head based on the mean wheel speed.

Fig. 4.12 shows the velocity disturbance trace in rotor tip inlet when the mass flow through the compressor decreases to 13.0 kg/s (ϕ=0.376). It is observed that at time instant corresponding to t=21.0 rotor revolutions, the computed flow developed into a "ring stall". Fig. 4.13 shows the flow coefficient contour on rotor exit plane, indicating that the "ring stall" has become fully established with reverse flow in the rotor hub region. Fig. 4.14 shows the comparison of compressor characteristic for clean inlet flow and inlet distorted flow; both the compressor performance and the stability margin deteriorates with inlet distortion.

4.4 Summary

A procedure was developed to modify the body force representation for NASA research compressor stage-35 to match the following aspects of measurements: Stalling mass flow and compressor characteristic slope near stall. The resulting representation reproduces the spanwise distribution of rotor loss and deviation close to stall point. While its use gives a computed stalling mass flow in agreement with measured value, the stalling flow pattern is that of the "ring stall" with reverse flow at hub. Likewise, the situation with inlet distortion appears to indicate that when the compressor stalls, ring stall with flow reversal at the hub is the final stalled pattern.

Comparing the computational results for both clean inlet flow with inlet distorted flow, we can deduce that:

(1) For clean inlet flow, the compressor using the calibrated body force formulation is a modal-type stall compressor with the 3rd harmonic disturbance playing a dominant role on stall inception process. The stalling mass flow was computed to be 11.9 kg/s, which agrees with experimental value of $\dot{m}_{stall,experiment}$=11.8 kg/s.

(2) For clean inlet flow, the final stall pattern of the compressor using the calibrated body force formulation is a "ring stall".

(3) For flow with circumferential total pressure inlet distortion, the final stall pattern of the compressor using the calibrated body force formulation is a "ring stall".

(4) Both the compressor performance and the stability margin deteriorates with inlet distortion.

Based on the above description, we deduce that the modified representation is still not adequate for reproducing the key flow features associated with observed stalling flow behavior in high-speed NASA stage-35 research compressor.

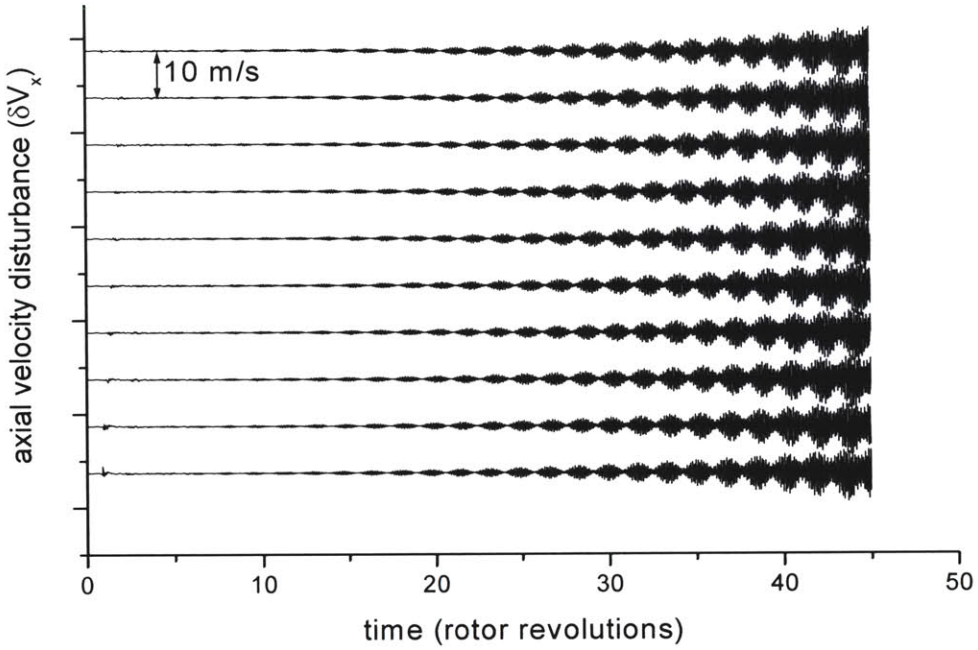

Fig. 4.1 Computed V_x traces on rotor tip inlet during stall inception process (spike-shaped disturbance as initial disturbance)

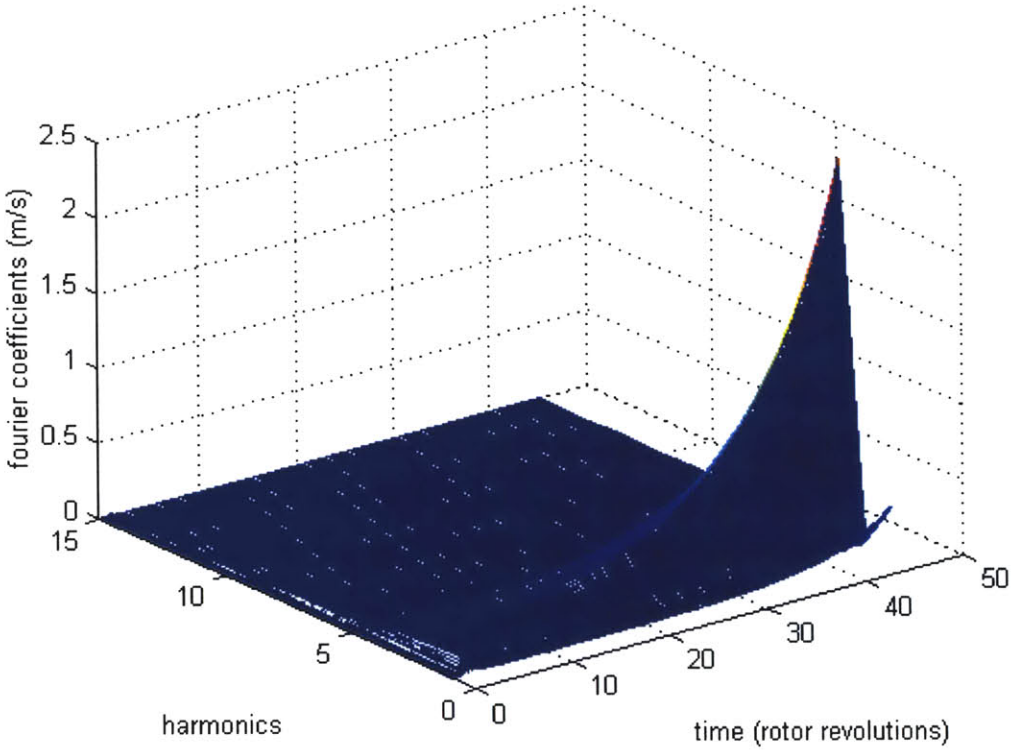

Fig. 4.2 Evolution of Fourier coefficients of computed V_x on rotor hub inlet for the first 15 harmonics

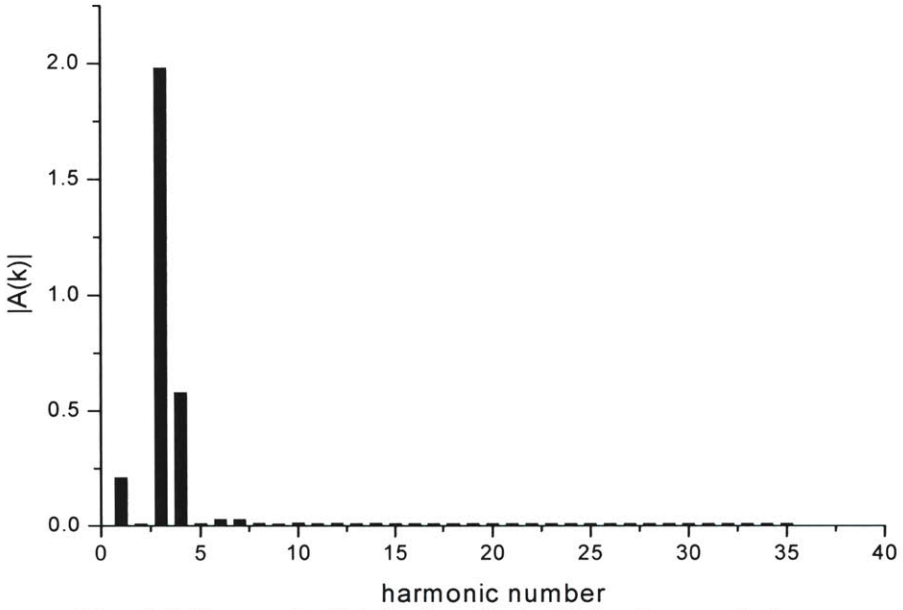

Fig. 4.3 Harmonic distribution for t=42.7 rotor revolutions

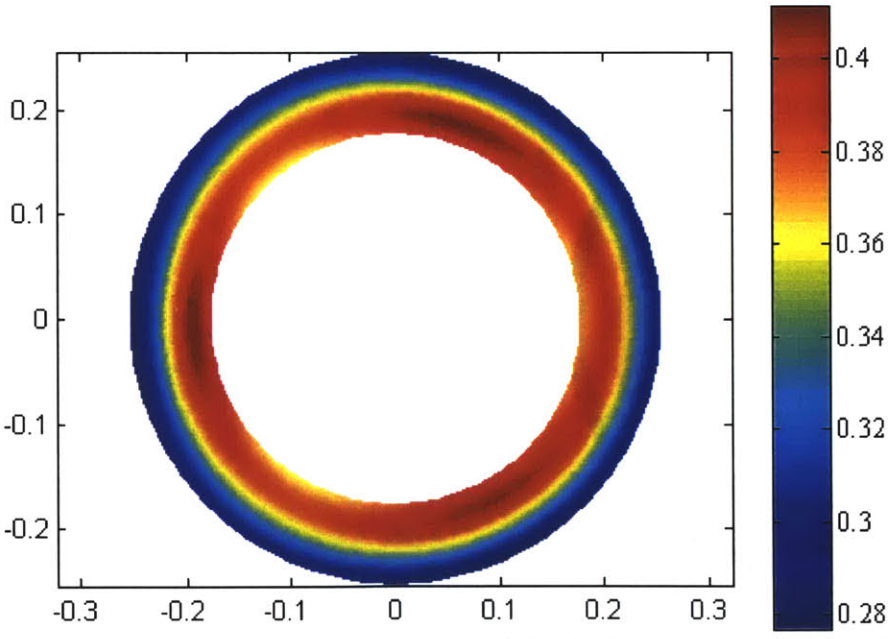

Fig. 4.4 Flow coefficient contour at rotor inlet (t=42.7 rotor revolutions)

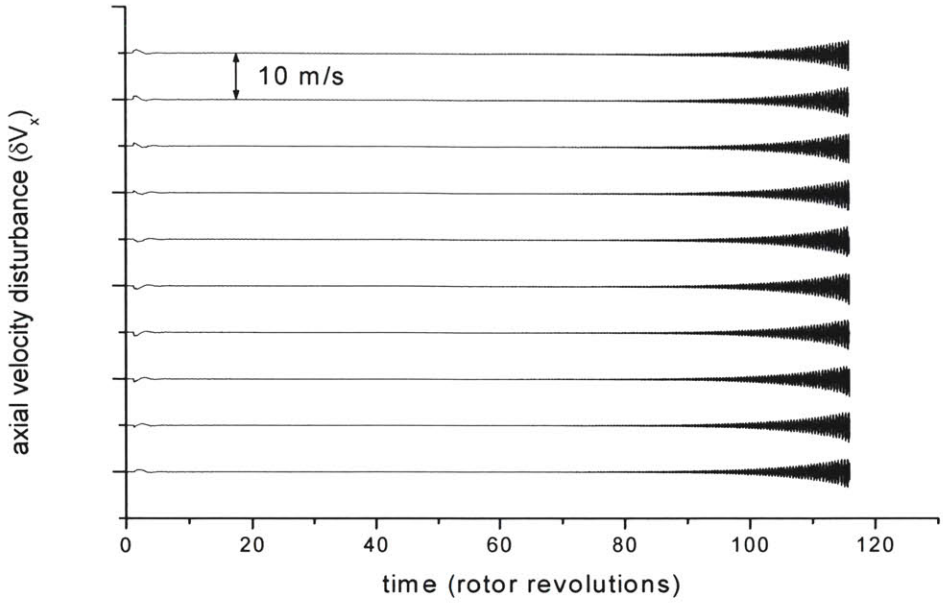

Fig. 4.5 Computed V_x traces in rotor tip inlet during stall inception process (modal-shaped disturbance as initial disturbance)

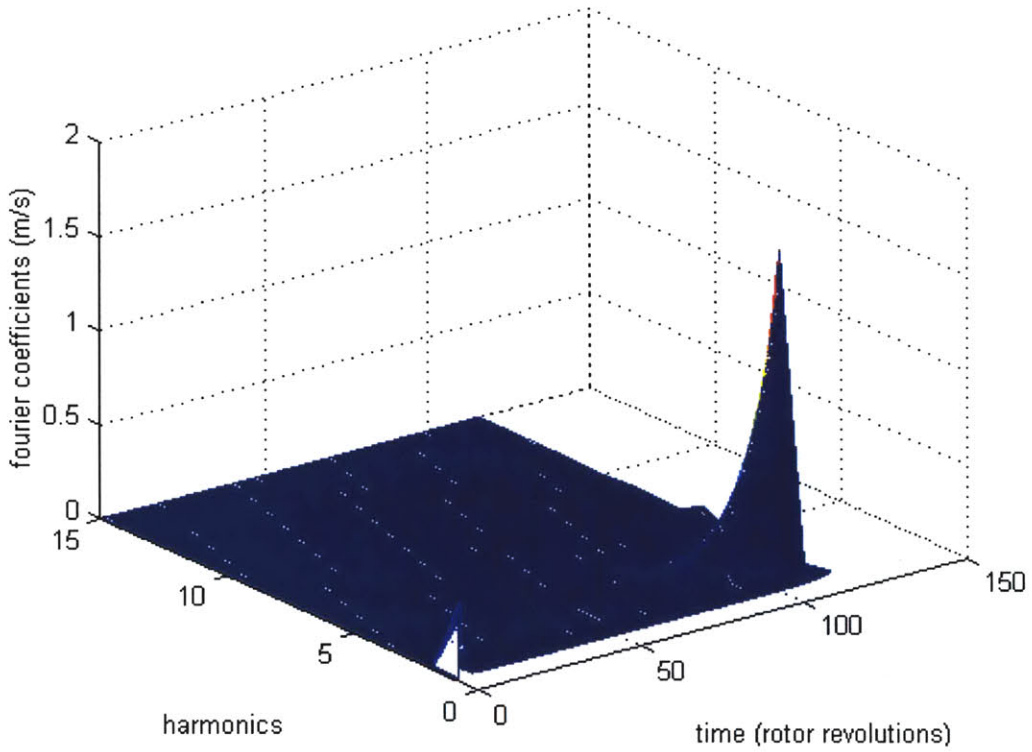

Fig. 4.6 Evolution of Fourier coefficients of calculated V_x in rotor tip inlet for the first 15 harmonics

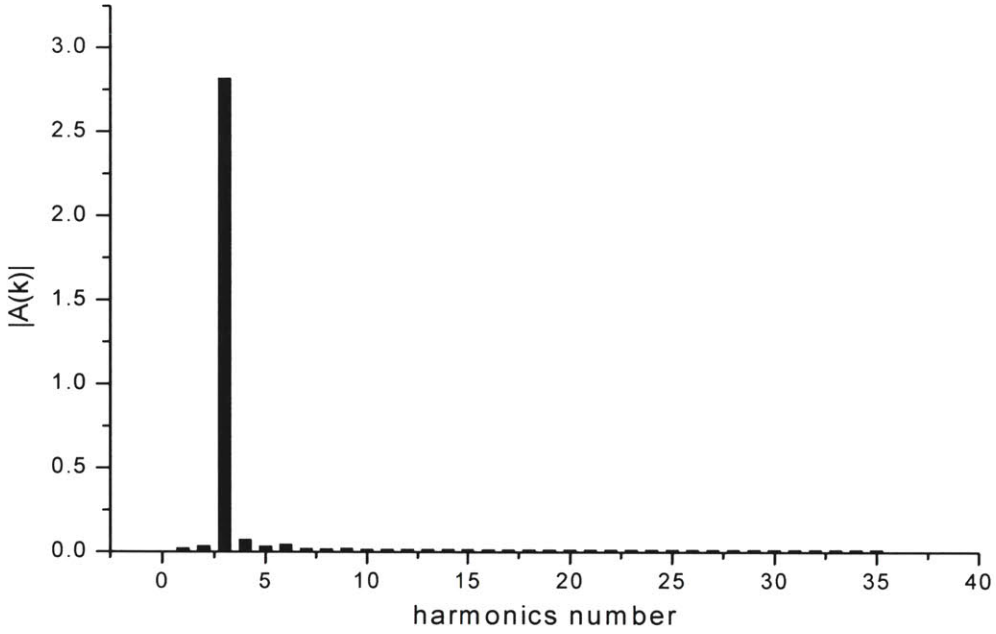

Fig. 4.7 Harmonic distribution for t=114.5 rotor revolutions

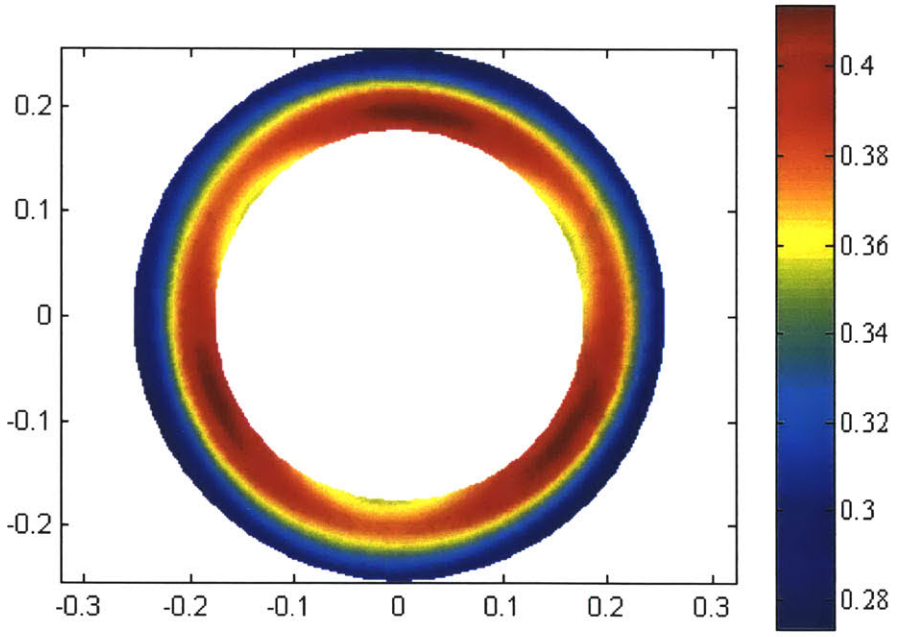

Fig. 4.8 Flow coefficient contour at rotor inlet (t=114.5 rotor revolutions)

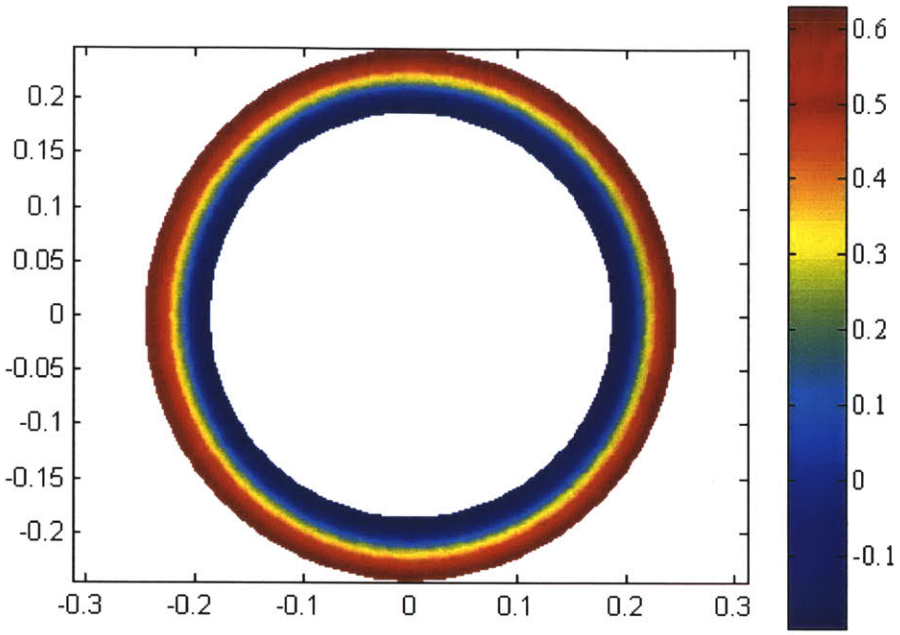

Fig. 4.9 Flow coefficient contour on rotor exit shows the final stall pattern is "ring stall"

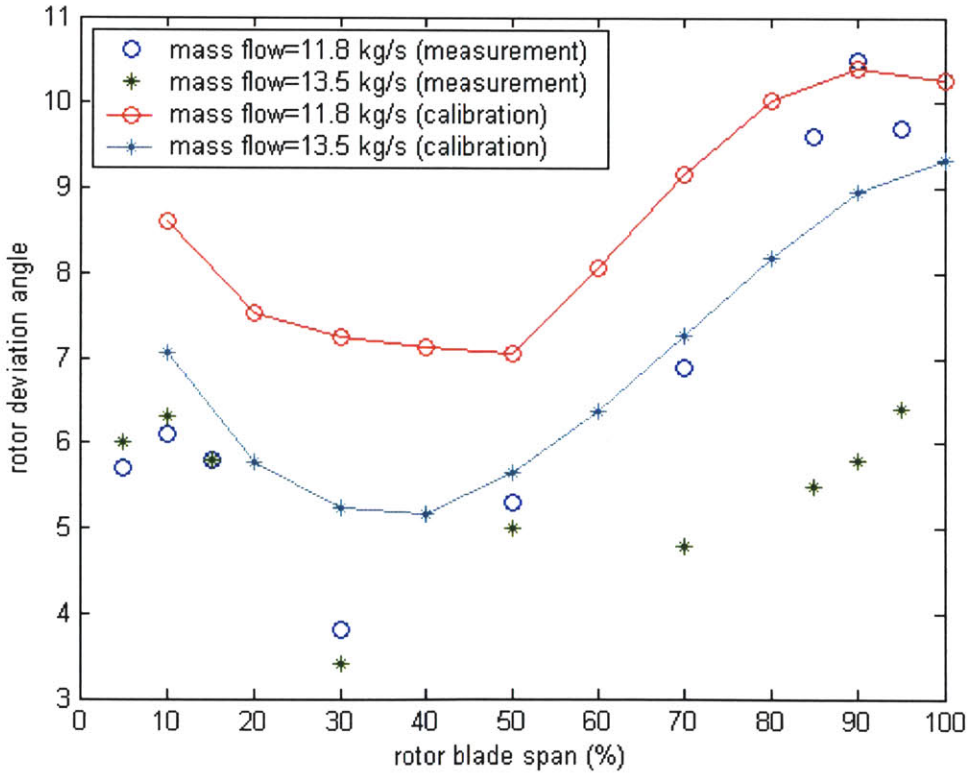

Fig. 4.10 Rotor deviation angle comparison by measurement and calibration for two operating points near stall

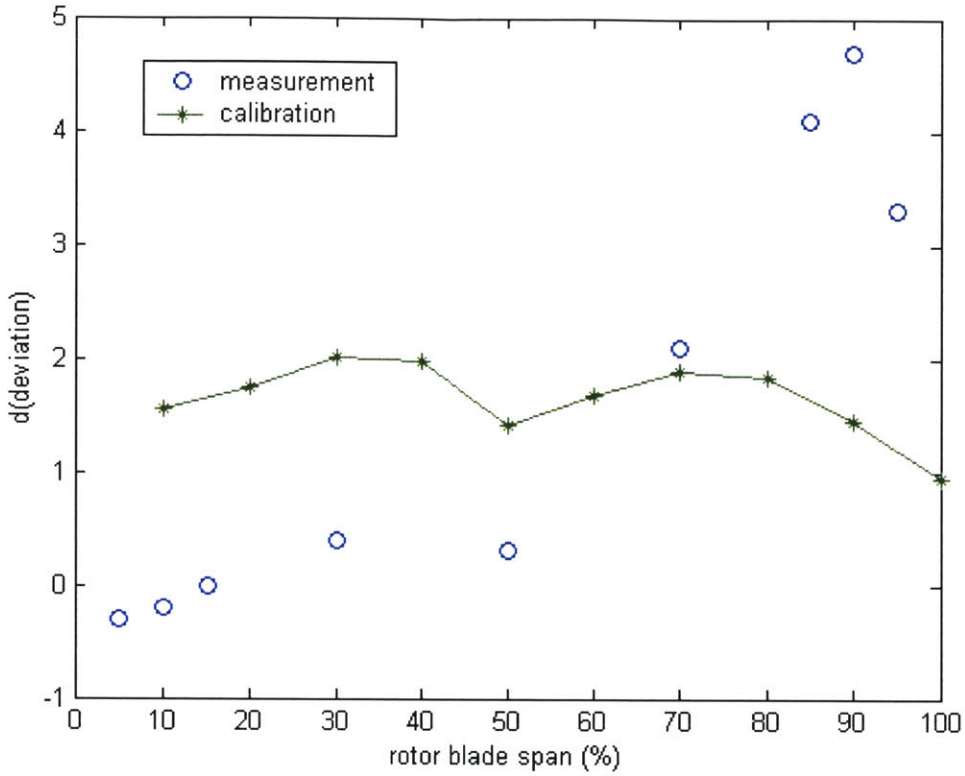

Fig. 4.11 Rotor deviation difference for the two operating points near stall

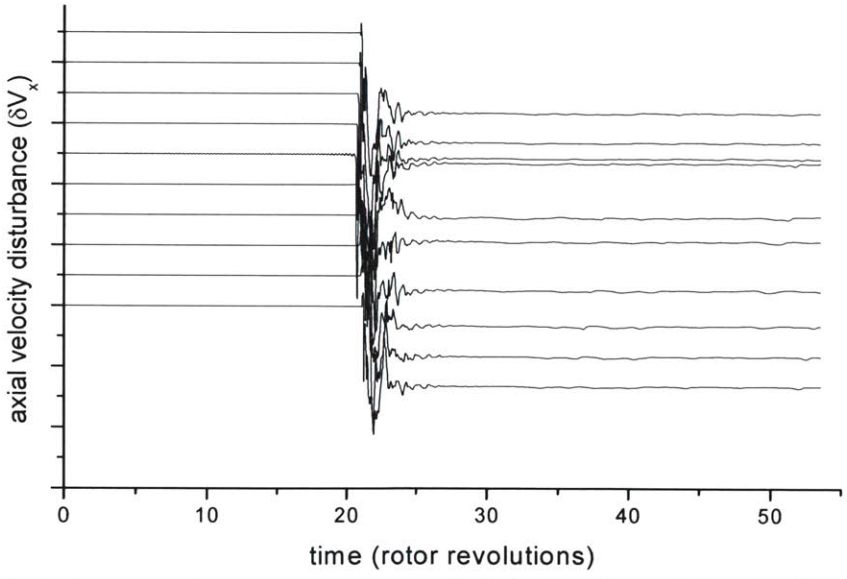

Fig. 4.12 Computed V_x traces on rotor tip inlet for flow with inlet distortion

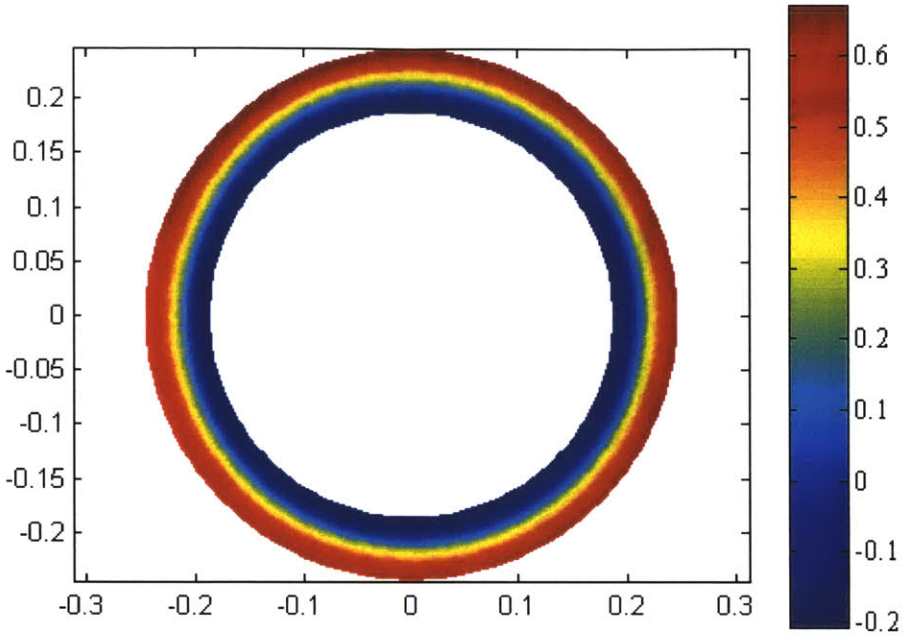

Fig. 4.13 Flow coefficient contour on rotor exit shows the final stall pattern is "ring stall"

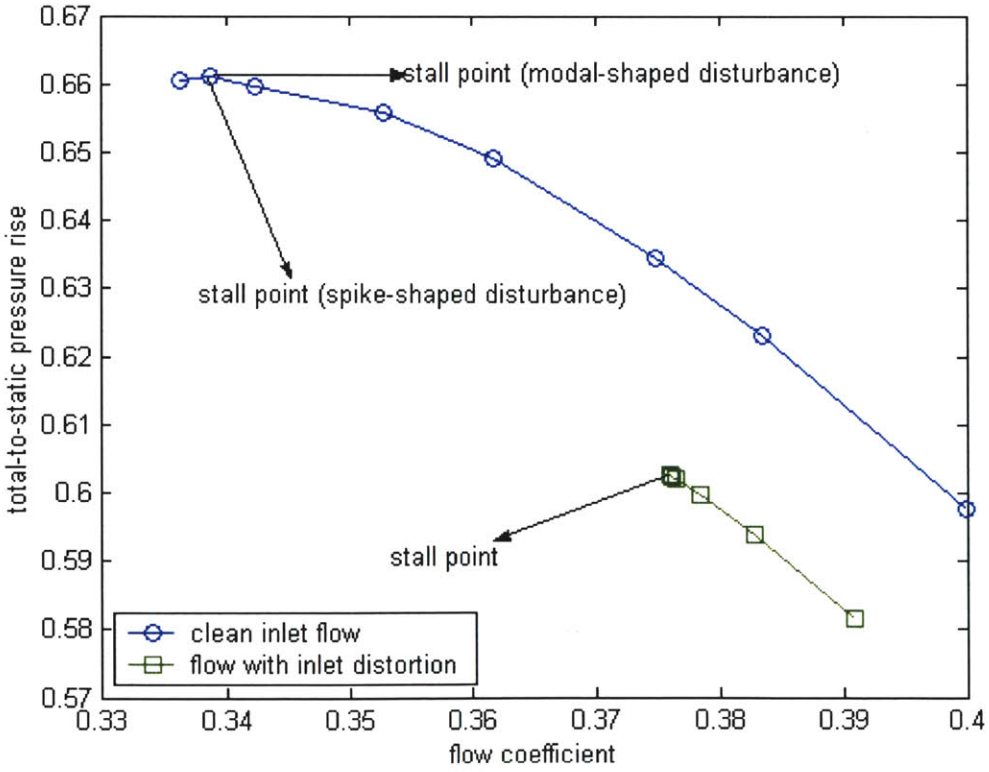

Fig. 4.14 Comparison of compressor characteristic for clean inlet flow and inlet distorted flow

Chapter 5

Summary, Conclusions and Future Work

5.1 Summary

The overall goal of this research project is to study the instability behavior of a single stage transonic compressor for both clean inlet flow and flow with circumferential total pressure inlet distortion. To achieve this goal, a computational study of compressor instability based on body force formulation in [9] as described by expressions given in Eq. 3.1 ~ Eq. 3.3 has been carried out. The computational results indicate that many aspects related to compressor instability differ from what was observed in the experiment: steady compressor characteristics, stalling mass flow as well as the details in stall inception process. The discrepancy has been attributed to the inadequacy of the body force formulation, which only reproduces the design operating point of the research compressor. In order to overcome this inadequacy, a procedure is proposed to modify the compressor body force based on the experimental data to match the stalling mass flow and compressor characteristic slope near stall. To assess the adequacy of the modified body force formulation, instability calculations incorporating the modification are carried out for both clean inlet flow and flow with circumferential total pressure inlet distortion. While the modified body force formulation yielded a computed stalling mass flow in agreement with measured value, the stall inception is through modal wave disturbance with 3^{rd} harmonic as the dominant harmonic. This differs from the experiment which indicates that the stall inception is a one-lobed sinusoidal modal wave disturbance. The calculations with inlet distortion show that both the compressor performance and stability margin deteriorate.

5.2 Concluding Remarks

The original objective of this research was to characterize the instability behavior of high-speed compressor subjected to circumferential inlet distortion with a distinct time scale of flow variation. It was determined that the status is such that assessment on the required level of details in the compressor modeling must be done before addressing the

stated objective. As such the goal was modified to determining the required level of details in the high-speed compressor modeling.

The use of the body force representation for high-speed compressor formulated to match the performance (i.e., efficiency and pressure ratio) at design operating point only has been shown to be inadequate of reproducing the key aspects of experimentally observed stalling behavior. The formulation was modified in a manner to match the following 2 aspects of the measured compressor characteristic: stalling mass flow and slope of compressor characteristic near stall. The modification does yield improvement; specifically its use in the computation gives the computed stalling mass flow in agreement with the measured value. However, the computed stall inception process differs from what was observed in the experiment, which indicates that the stall inception is through initial spike followed by modal wave disturbance. As such, the modification developed did not yield an adequate formulation that could enable us to proceed to address the originally stated objective, i.e., the effect of length scale and time scale of inlet distortion on compressor stability.

5.2 Recommendations for Future Work

From the summary and conclusions, the future work that need to be carried out should be focused on resolving the identified difficulties with the present formulation. To accomplish this, the followings are suggested:

1. The body force formulation should be such as to reproduce the loss and deviation distribution from hub to tip near the peak of compressor characteristic;
2. The body force formulation should be able to yield the correct axisymmetric compressor characteristic to zero mass flow since inlet distorted flow corresponds to low flow coefficient region.

Bibliography

1. Greitzer, E. M., "The Stability of Pumping System- The 1980 Freeman Scholar Lecture," *ASME Journal of Fluids Engineering, Vol. 103,* 1981, pp. 193-242.
2. Moore, F. K. and Greitzer, E. M. " A Theory of Post-Stall Transients in Axial Compression Systems: Part I, II, " *ASME Journal of Engineering for Gas Turbines and Power, Vol. 108*, 1986, pp 68-76, pp 231-239.
3. Garnier, V. H., Epstein, A. H. and Greitzer, E. M. "Rotating Waves as a Stall Inception Indication in Axial Compressors. " *ASME Journal of Turbomachinery, Vol. 113*, 1991, pp 290-301.
4. Day, I. J. "Stall Inception in Axial Flow Compressors, " *ASME Journal of Turbomachinery, Vol.115*, 1993, pp. 40-47.
5. Emmons, H. W, Pearson, C.E., and Grant H. P., "Compressor surge and stall propagation" Transaction of ASME, *Vol. 79*, 1955, pp 455-469.
6. Dunham, J. "Non-axisymmetric flows in axial compressors" Mechanical Engineering Science Monograph No. 3, 1965.
7. Moore, F.K., "A Theory of Rotating Stall in Multistage Axial Compressors: Part I-III, " *ASME Journal of Engineering for Gas Turbines and Power, Vol. 106*, 1984, pp. 313-336.
8. Hynes, T.P. and Greitzer, E.M., "A Method for Assessing Effects for Inlet Flow Distortion on Compressor Stability" *ASME Journal of Engineering for Power, Vol. 109*, 1987, pp 371-379.
9. Gong, Y.F, "A Computational Model for Rotating Stall and Inlet Distortion in Multi-Stage Compressors." Ph.D. thesis, Massachusetts Institute of Technology, Feb. 1999.
10. Marble, F.E., 1964 "Three-Dimensional Flow in Turbomachines," *Aerodyanmics of Turbines and Compressors, Vol. X* of High Speed Aerodynamics and Jet Propulsion, Hawthorne, W. R., ed. Princeton University Press, Princeton, NJ., pp 83-166.
11. Lieblein, S. "Experimental Flow in Two-Dimcnsional Cascades," Aerodynamic Design of Axial-Flow Compressors, NASA SP-36, 1965, pp.183-226.

12. Reid, L., and Moore, R. D. "Performance of Single-Stage Axial-Flow Transonic Compressor with Rotor and Stator Aspect Ratios of 1.19 and 1.26, Respectively, and with Design Pressure Ratio of 1.82," NASA technical Paper 1338, 1978.
13. Park, H.G., "Unsteady Disturbances Structures in Axial Flow Compressor Stall Inception," Master's thesis, Massachusetts Institute of Technology, 1994.
14. Takata, H., and Nagano, S. "Nonlinear Analysis of Rotating Stall," ASME paper 72-GT-3, 1972.
15. He, L. "Computational Study of Rotating-Stall Inception in Axial Compressors," *AIAA Journal of Propulsion and Power, vol. 13*, No. 1, 1997, pp.31-38.
16. Hoying, D. A., Tan, C. S., Vo, H. D., and Greitzer, E. M. "Role of Blade Passage Flow Structures in Axial Compressor Rotating Stall Inception," ASME paper 98-GT-588, 1998.
17. Longley, L. P. " Calculating the Flow Field Behavior of High-Speed Multi-Stage Compressors," ASME paper No. 97-GT-468, 1997.
18. Hendricks, G. J., Sabnis, J. S., and Feulner, M. R. "Analysis of Instability Inception in High-Speed Multistage Axial-Flow Compressors," *ASME Journal of Turbomachinery, Vol. 119,* 1997, pp. 714-722.
19. Escuret, J. F. and Garnier, V., "Numerical Simulations of Surge and Rotating Stall in Multi-Stage Axial-Flow Compressors," AIAA paper No. 94-3202, 1994.
20. Billet, G., Hurd, J., Chevalier, P. and Laval, P. "Experimental and Numerical Study of the Response of an Axial Compressor to Distorted Inlet Flow," *ASME Journal of Fluids Engineering Vol. 110,* 1988, pp. 355-360.
21. Camp, T. R. and Day, I. J. "A Study of Spike and Modal Stall Phenomenon in a Low-Speed Axial Compressor," ASME paper No. 97-GT-526, 1997.
22. Jameson, A., Schmidt, W., and Turkel, E., "Numerical Solutions of the Euler Equations by Finite Volume Methods with Runge-Kutta Time Stepping Schemes," AIAA paper No. 81-1259, 1981.
23. Cumpsty, N. A., and Greitzer, E. M. " A Simple Model for Compressor Stall Cell Propogation," *ASME Journal of Engineering for Power Vol. 104,* 1982, pp. 170-176.

24. Reid, C., "The Response of Axial Flow Compressors to Intake Flow Distortion," ASME paper 69-GT-29, Gas Turbine Conference, 1969.
25. Mazzawy, R. S., "Multiple Segment Parallel Compressor Model," *ASME Journal of Engineering Power, Vol. 99*, 1977, pp. 288-296.
26. Longley, J. P., Shin, H. W., Plumley, R. E., Silkowsiki, P. D., Day, I. J., Greitzer, E. M., Tan, C. S., and Wisler, D. C., "Effects of Rotating Inlet Distortion on MultiStage Compressor Stability," *ASME Jounral of Turbomachinery, Vol. 118* 1996, pp. 181-188.
27. Peyet, R., Taylor, T.D., Computational Methods for Fluid flow, Springer-Veriag, 1983.
28. Felici, " A Coupled Eulerian/Lagrangian Method for the Solution of Three-Dimensional Vortical Flows," Ph.D. Thesis, Massachusetts Institute of Technology, 1992.
29. Orner, N., "Rotating Stall in Axial Flow Compressors," Von Karman Institute Lecture Series, "Unsteady Flow in Turbomachines," Brussels, Belgium, 1979.
30. Adamczyk, J.J., "Unsteady Fluid Dynamic Response of an Isolated Rotor with Distorted Flow," AIAA paper 74-49, 1974.
31. Pandolfi, M. and Colasurdo, "Numerical Investigation on the Generation and Development of Rotating Stalls," ASME paper 78-WA/GT-5, 1978.
32. Spakovszky, Z., Weigl, H., Paduano, J., Van Schalkwyk, C., Suder, K., and Bright, M. "Rotating Stall Control in a High-speed Stage with Inlet Distortion, Part I – Radial Distortion". ASME paper 98-GT-264, 1998.
33. Gorrell, S. and Russler, P. "Stall Inception in a High-Speed Low Aspect Ratio Fan Including the Effects of Casing Treatments". ASME paper 94-GT-322, 1994.
34. Greitzer, E. "Surge and Rotating Stall in Axial Flow Compressors". *ASME Journal of Engineering for Power, Vol. 98,* No. 2, 1976, pp 190-217.
35. Weigl, H. "Active Stabilization of Rotating Stall and Surge in a Transonic Single Stage Axial Compressor", Ph.D. thesis, Massachusetts Institute of Technology, 1997.
36. McDougall, N., Cumpsty, N., and Hynes, T. "Stall Inception in Axial Compressors". *ASME Journal of Turbomachinery, Vol. 112*, 1990, pp. 228-246.

37. Soundranayagam, M. and Elder, R. "A Study of Stall in a Low Hub/Tip Ratio Fan". *ASME Journal of Turbomachinery, Vol. 115*, 1993, pp. 10-18.
38. Jackson, A. "Stall Cell Development in an Axial Compressor". ASME paper 86-GT-249, 1986.
39. Longley, L. P. "A Review of Non-Steady Flow Models For Compressor Stability". ASME paper 93-GT-17.
40. Paduano, J. D. "Recent Developments in Compressor Stability and Control".
41. Tikhonov, A.N., "Solution of incorrectly formulated problems and the regularization method," *Dokl. Akad. Nauk SSSR,* 151(1963), pp. 501-504, *Soviet Math. Dokl.*, 4, 1963, pp. 1035-1038.
42. Tikhonov, A.N., and Arsenin, V.Y., Solutions of Ill-Posed Problems, Winston and Sons, Washington, 1977.
43. Golub, G.H. and Kahan, W., "Calculating the Singular Value Decomposition and Pseudo-Inverse of a Matrix," *SIAM J. Numer. Anal.*, 2, 1965, pp. 205-224.
44. Golub, G.H., Heath, M. and Wahba, G, "Generalized Cross-Validation as a Method for Choosing a Good Ridge Parameter," *Technometrics, Vol. 21, No. 2*, 215-223, May 1979.
45. Hadamard, J., Lectures on Cauchy's Problem in Linear Partial Differential Equations, Yale University Press, New Haven, 1923.
46. Spakovszky Z., "Active Control of Rotating Stall in NASA Compressor Stage 35 with Inlet Distortion." Master's thesis, Massachusetts Institute of Technology, 1998.

Appendix I

Post Process of Computational Results

Two kinds of data analysis methods: Spatial Fourier Transform and Fourier Collocation Method are used in this thesis to implement the post process of the computational results. They are discussed in detail in the following:

I. Spatial Fourier Transform

Spatial Fourier Transform (SFT) is used as the basic form of data reduction for computational results. At each time step a discrete Spatial Fourier transform was performed on several velocity measurements around the compressor annulus. Using this method, the individual velocity traces can be combined to yield the history of the circumferentially traveling modal waves. The Fourier transform is performed as follows:

$$C_k = \frac{1}{N}\sum_{n=1}^{N} x_n \exp(\frac{-2ik\pi n}{N})$$

C_k = Spatial Fourier coefficients

N = total number of velocity traces along the circumferential direction

$k = -N/2, N/2-1$ where x_n represents the N individual velocity perturbation (mean flow velocities which are the velocity before the disturbance is imposed, has been subtracted out from the total velocity trace) at a given time. The results of the transform are complex Fourier coefficients for modes $-N/2, N/2-1$. Since the coefficients form pairs of complex conjugates, the coefficients corresponding to $k = 1,2\cdots N/2-1$ provide all the information necessary to analyze the first $N/2-1$ modes of the compressor flow field.

II. Fourier Collocation Method

In addition to SFT, the Fourier Collocation method is used to handle the computations for the spacial variations. In this technique, the flow variables that are functions of θ are expressed in finite Fourier series. The method of collocation provides a convenient way to handle the nonlinear terms of the equations. This is done by discretizing the annulus in

N grid points, and imposing the equations to be satisfied at these points only. By doing so, for example, the axial velocity perturbation component is expressed as:

$$\phi_j = \sum_{k=-K}^{K-1} A_k e^{ik\theta_j}\ ,\ \theta_j = \frac{2\pi}{N-1} j,\ k = N/2$$

once ϕ_j is known, the Fourier coefficients can be obtained through an inverse transform relation

$$A_k = \frac{1}{N} \sum_{j=1}^{N} \phi_j \exp(-ik\theta_j)$$

Thus, we can analyze the Fourier component for different time by plotting A_k for all the harmonics.

Appendix II

Detailed Calibration Procedure of Compressor Body Force

In this section, a calibration procedure for compressor body force based on the experimental data is proposed and described in detail.

Based on the idea of Gong [9], the body force formulation includes the following two steps: (1) determination of a body force field from a three-dimensional flow in a blade passage; (2) deducing the body force coefficients as functions of local flow properties.

Firstly the procedure for determining the body force field which will produce a axisymmetric flow field which is the same as that of the pitch-wise average of a given three-dimensional flow field. The procedure is applied to compute the body forces for different operating points; then the body force expression for each spatial point can be deduced from these body forces for different operating conditions. This mainly consists of the following two steps:

I. Determination of the Body Force from a Three-Dimensional Flow in a Blade Passage

A three-dimensional flow field, which can be obtained from either CFD computation or experimental measurement, is expressed as

$$V_x(x,\theta,r),\ V_\theta(x,\theta,r),\ V_r(x,\theta,r),\ T(x,\theta,r),\ P(x,\theta,r),\ \rho(x,\theta,r),\ \ldots$$

After pitch-wise average, an axisymmetric flow field can be expressed as

$$V_x(x,r),\ V_\theta(x,r),\ V_r(x,r),\ T(x,r),\ P(x,r),\ \rho(x,r),\ \ldots$$

The momentum equations with body force terms for the steady flow in a blade row can be written as the following:

$$\frac{\partial}{\partial x}\begin{bmatrix} r\rho V_x^2 + rp \\ r\rho V_x V_\theta \\ r\rho V_x V_r \end{bmatrix} + \frac{\partial}{\partial r}\begin{bmatrix} r\rho V_x V_r \\ r\rho V_\theta V_r \\ r\rho V_r^2 + rp \end{bmatrix} = \begin{bmatrix} r\rho(F_{nx} + F_{px}) \\ -\rho V_\theta V_r + r\rho(F_{n\theta} + F_{p\theta}) \\ \rho V_\theta^2 + p + r\rho(F_{nr} + F_{pr}) \end{bmatrix} \tag{A.1}$$

The force terms in the above equations are

$$F_n = \frac{V_{rel}^2}{h} f_n(M, \Delta\beta) + \frac{1}{\rho}\frac{\partial P}{\partial x}\sin\alpha \tag{A.2}$$

$$F_p = \frac{V_{rel}^2}{h} f_p(M, \Delta\beta) \tag{A.3}$$

where V_{rel} is the relative velocity. Effectively, formulating of the body force is equaivalent to finding f_n and f_p as functions of the local flow conditions.

Integrating Eq. A.1 on a control volume gives

$$\int_{\delta\Gamma} \left(\begin{bmatrix} r\rho V_x^2 + rp \\ r\rho V_x V_\theta \\ r\rho V_x V_r \end{bmatrix} \hat{x} + \begin{bmatrix} r\rho V_x V_r \\ r\rho V_\theta V_r \\ r\rho V_r^2 + rp \end{bmatrix} \hat{r} \right) d(\delta\Gamma) = \int_{\Gamma} \begin{bmatrix} r\rho(F_{nx} + F_{px}) \\ -\rho V_\theta V_r + r\rho(F_{n\theta} + F_{p\theta}) \\ \rho V_\theta^2 + p + r\rho(F_{nr} + F_{pr}) \end{bmatrix} d\Gamma \tag{A.4}$$

where Γ is the control volume, $\delta\Gamma$ is the surface of the control volume, $\hat{x}$ and $\hat{r}$ unit vectors in the axial and radial directions. If the control volume is a small mesh cell, the value of the right hand side of Eq. A.4 can be evaluated assuming the flow properties in the mesh cell to be approximately uniform. Then the above equation set becomes

$$\int_{\delta\Gamma} \left(\begin{bmatrix} r\rho V_x^2 + rp \\ r\rho V_x V_\theta \\ r\rho V_x V_r \end{bmatrix} \hat{x} + \begin{bmatrix} r\rho V_x V_r \\ r\rho V_\theta V_r \\ r\rho V_r^2 + rp \end{bmatrix} \hat{r} \right) d(\delta\Gamma) = V_\Gamma \begin{bmatrix} r\rho(F_{nx} + F_{px}) \\ -\rho V_\theta V_r + r\rho(F_{n\theta} + F_{p\theta}) \\ \rho V_\theta^2 + p + r\rho(F_{nr} + F_{pr}) \end{bmatrix} \tag{A.5}$$

where V_Γ is the volume of the control volume. F_x, F_θ, and F_r can be computed using the above equation set; and their components normal and parallel to the relative velocity can be calculated. Finally, f_n and f_p can be calculated using their definition in Eq. A.2 and Eq. A.3.

II. Deducing f_n and f_p as Functions of Local Flow Properties

In the previous section, f_n and f_p at each mesh cell can be calculated for a given three-dimensional flow field. They are labeled as:

$$f_n(j,k),\ f_p(j,k)$$

where (j,k) is the index of a mesh cell (Fig. A.2). A simple way of formulating these f_n and f_p is to express them as polynomials, such as

$$f_n(j,k) = C_{n0(j,k)} + C_{n1(j,k)}\beta + C_{n2(j,k)}\beta^2 + C_{n3(j,k)}M + C_{n4(j,k)}M^2 \tag{A.6}$$

$$f_p(j,k) = C_{p0(j,k)} + C_{p1(j,k)}\beta + C_{p2(j,k)}\beta^2 + C_{p3(j,k)}M + C_{p4(j,k)}M^2 \tag{A.7}$$

where $C_{no}, \ldots C_{p4}$, are coefficients to be determined. If a sufficient number of f_n and f_p have been computed for different operating points using the method described in the previous section, then C can be determined to have the best fit for these f_n and f_p.

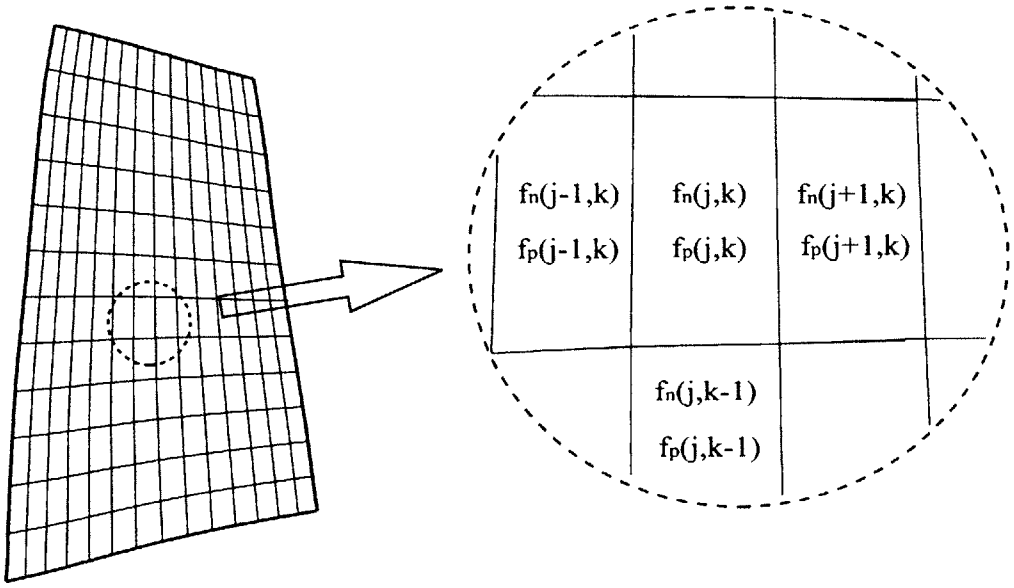

Fig. A.1 f_n and f_p are defined on each cell of pre-generated mesh

III. Calibration Procedure

Based on the above procedures, the detailed calibration procedure for body force formulation of NASA stage-35 compressor is as follows:

Firstly, using an iterative procedure to tune the loss and deviation angle for different operating points at 70% speed. This basically means for one operating point, using presumed expressions for both parallel and normal body force coefficients to do an axisymmetric calculation (in this step, the body force coefficients don't need to be functions of local flow properties), the main goal is to match the experimental data for mass flow, total pressure ratio, deviation angle, loss coefficients distribution along the blade span. If there is some deviation from the experiments, some adjustments to the body force coefficients are fulfilled and another calculation is carried out. For example, if the loss in the tip region is found to be larger than experimental data, the parallel body force coefficient k_p in the tip region is decreased and an axisymmetric calculation is done again. This kind of iterative process is pressed on until there is a good agreement with the experimental data. At the same time, local deviation angle and mach number are

recorded for different operating points. Finally, there are five sets of body force coefficients corresponding to the five operating points.

Secondly, using the curve fit method to match the five operating points and express body force coefficients as functions of local flow properties. This basically means using one set of body force coefficients which are functions of local flow properties to represent the five sets of body force coefficients obtained in the first step.

For the five operating points, we have

$$\begin{cases} K_{n1} = A_0 + A_1\beta_1 + A_2\beta_1^2 + A_3M_1 + A_4M_1^2 \\ K_{n2} = A_0 + A_1\beta_2 + A_2\beta_2^2 + A_3M_2 + A_4M_2^2 \\ K_{n3} = A_0 + A_1\beta_3 + A_2\beta_3^2 + A_3M_3 + A_4M_3^2 \\ K_{n4} = A_0 + A_1\beta_4 + A_2\beta_4^2 + A_3M_4 + A_4M_4^2 \\ K_{n5} = A_0 + A_1\beta_5 + A_2\beta_5^2 + A_3M_5 + A_4M_5^2 \end{cases} \tag{A.8}$$

$$\begin{cases} K_{p1} = B_0 + B_1\beta_1 + B_2\beta_1^2 + B_3M_1 + B_4M_1^2 \\ K_{p2} = B_0 + B_1\beta_2 + B_2\beta_2^2 + B_3M_2 + B_4M_2^2 \\ K_{p3} = B_0 + B_1\beta_3 + B_2\beta_3^2 + B_3M_3 + B_4M_3^2 \\ K_{p4} = B_0 + B_1\beta_4 + B_2\beta_4^2 + B_3M_4 + B_4M_4^2 \\ K_{p5} = B_0 + B_1\beta_5 + B_2\beta_5^2 + B_3M_5 + B_4M_5^2 \end{cases} \tag{A.9}$$

Writing the above equations in matrix form:

$$\begin{bmatrix} 1 & \beta_1 & \beta_1^2 & M_1 & M_1^2 \\ 1 & \beta_2 & \beta_2^2 & M_2 & M_2^2 \\ 1 & \beta_3 & \beta_3^2 & M_3 & M_3^2 \\ 1 & \beta_4 & \beta_4^2 & M_4 & M_4^2 \\ 1 & \beta_5 & \beta_5^2 & M_5 & M_5^2 \end{bmatrix} \begin{bmatrix} A_0 \\ A_1 \\ A_2 \\ A_3 \\ A_4 \end{bmatrix} = \begin{bmatrix} K_{n1} \\ K_{n2} \\ K_{n3} \\ K_{n4} \\ K_{n5} \end{bmatrix} \tag{A.10}$$

$$\begin{bmatrix} 1 & \beta_1 & \beta_1^2 & M_1 & M_1^2 \\ 1 & \beta_2 & \beta_2^2 & M_2 & M_2^2 \\ 1 & \beta_3 & \beta_3^2 & M_3 & M_3^2 \\ 1 & \beta_4 & \beta_4^2 & M_4 & M_4^2 \\ 1 & \beta_5 & \beta_5^2 & M_5 & M_5^2 \end{bmatrix} \begin{bmatrix} B_0 \\ B_1 \\ B_2 \\ B_3 \\ B_4 \end{bmatrix} = \begin{bmatrix} K_{p1} \\ K_{p2} \\ K_{p3} \\ K_{p4} \\ K_{p5} \end{bmatrix} \tag{A.11}$$

In the above formulations, K_n and K_p are body force coefficients in normal and parallel directions respectively. They are both distributions along the blades (rotor and stator). The number index 1,2…5 stand for the five operating points in the experimental data.

However, the iteration process in the first step of body force calibration is found to be rather cumbersome, matching five operating points is really a lot of work. In addition, for five operating points, the dimension of the matrix in eq. is very large and solving the equation needs a lot of computational power. Based on the above reason, the dimension of the above problem was reduced from 5 to 2, that is to say, only two operating points in the compressor map are calibrated using the above proposed procedure. In this thesis, we pick the two operating points near stall. Since we are more concerned about the instability behavior of the compressor. Two operating points near stall can determine the slope of the characteristic line near stall, which also determines the stability of pre-stall perturbations in Moore-Greitzer model. The detailed body force formulation for the two operating points near stall is as follows:

In the first step, the manual iteration was done to tune the compressor characteristics, loss and deviation. Fig. A.1 ~ Fig. A.8 shows the results (loss and deviation angle) for manual iteration, where 3989 and 3990 are the two operating points near stall. In all the figures, line stands for calculated results and circles stand for experimental data. Since rotor plays a more important role in rotating stall compared with stator, more attention is put on the calibration of rotor body force. The two settings of body force coefficients in both normal and parallel directions are recorded as K_{n1}, K_{p1}, K_{n2}, K_{p2}. Where the index 1 and 2 stand for the two operating points 3989 and 3990 respectively.

Therefore, we have two different settings of body force coefficients for the two operating points near stall. After matching these two operating points respectively, we try to link these two operating points by expressing the body force coefficients as a function of local flow property. In this part, the body force coefficients are expressed as a function of local deviation angle, the reason to choose local deviation angle is it can take into account the effect of inlet distortion, swirling flow, etc. This is essential to simulate stall inception process with inlet distorted flow. So we have:

$$\begin{cases} K_{n1,r} = A_0 + A_1\beta_{1,r} \\ K_{n2,r} = A_0 + A_1\beta_{2,r} \end{cases} \tag{A.12}$$

$$\begin{cases} K_{p1,r} = B_0 + B_1\beta_{1,r} \\ K_{p2,r} = B_0 + B_1\beta_{2,r} \end{cases} \tag{A.13}$$

$$\begin{cases} K_{n1,s} = C_0 + C_1\beta_{1,s} \\ K_{n2,s} = C_0 + C_1\beta_{2,s} \end{cases} \tag{A.14}$$

$$\begin{cases} K_{p1,s} = D_0 + D_1\beta_{1,s} \\ K_{p2,s} = D_0 + D_1\beta_{2,s} \end{cases} \tag{A.15}$$

In the above equations, A_0, A_1 are rotor body force coefficients in normal direction, B_0, B_1 are rotor body force coefficients in parallel direction, C_0, C_1 are stator body force coefficients in normal direction, D_0, D_1 are stator body force coefficients in parallel direction. The index r and s stand for rotor and stator respectively. The index 1 and 2 in K_n, K_p and β stand for the two operating points near stall. All the above parameters above are distributions along the blades (rotor and stator). Therefore for rotor, the dimensions of K_n and K_p are 10×12=120, where 10 is the grid number in radial direction and 12 is the grid number in axial direction on the rotor; for stator, the dimensions of K_n and K_p are 10×13=130, where 10 is the grid number in radial direction and 13 is the grid number in axial direction on the stator.

For simplicity, we only talk about rotor body force in normal direction in the following.

$$\begin{bmatrix} 1 & \beta_{1,r} \\ 1 & \beta_{2,r} \end{bmatrix} \begin{bmatrix} A_0 \\ A_1 \end{bmatrix} = \begin{bmatrix} K_{n1,r} \\ K_{n2,r} \end{bmatrix} \tag{A.16}$$

For the above equation. The detailed structure of the matrix in the LHS of Eq. A.16 is

$$\begin{bmatrix} \begin{bmatrix} 1 & \beta_{1r,1} \\ 1 & \beta_{2r,1} \end{bmatrix} & & & & 0 \\ & \begin{bmatrix} 1 & \beta_{1r,2} \\ 1 & \beta_{2r,2} \end{bmatrix} & & & \\ & & \ddots & & \\ & & & \begin{bmatrix} 1 & \beta_{1r,119} \\ 1 & \beta_{2r,119} \end{bmatrix} & \\ 0 & & & & \begin{bmatrix} 1 & \beta_{1r,120} \\ 1 & \beta_{2r,120} \end{bmatrix} \end{bmatrix} \tag{A.17}$$

it's a square sparse matrix with dimension 240×240

The detailed structure for right hand side in Eq. A.16 is:

$$\begin{bmatrix} K_{n1,1} \\ K_{n1,2} \\ \vdots \\ K_{n1,120} \\ K_{n2,1} \\ K_{n2,2} \\ \vdots \\ K_{n2,120} \end{bmatrix} \tag{A.18}$$

it is a column vector with dimension 240×1.

The detailed structure of the body force coefficients vector in Eq. A.16 that we are solving for is:

$$\begin{bmatrix} A_{0,1} \\ A_{0,2} \\ \vdots \\ A_{0,120} \\ A_{1,1} \\ A_{1,2} \\ \vdots \\ A_{1,120} \end{bmatrix} \tag{A.19}$$

it is a column vector with dimension 240×1.

Solving the above matrix equation yields the desired rotor body force coefficients in normal direction. The rotor body force coefficients in parallel direction can be obtained following the same procedure. Similarly, the stator body force coefficients can also be computed by the same method, the only difference is the dimension of the matrix for solving is 260×260, since the axial grid number on stator blade is 13 instead of 12 on rotor blade.

However, by observing the matrix in Eq. A.16, it's easy to see that the matrix will be near singular is the local deviation for the two operating points are very close to each other. This means the problem will become ill-posed and small errors in the input data will result in large errors in the solutions. For a ill-posed problem, the standard matrix solvers such as LU, QR can not be used and some regularization method is employed in this thesis to solve this problem. In this thesis, the Tikhonov Regularization method

combined with Singular Value Decomposition is employed to solve the matrix equation A.16. The detailed solving method is introduced in Appendix III.

Fig. A.9 ~ Fig. A.16 show the results of comparison of calibration and measurement for compressor blade (rotor and stator) deviation angle and loss. The "first step calibration" means the initial iterative process to tune the loss and deviation. In this step, body force coefficients are different for different operating points and the body force coefficients are ***not*** functions of local flow properties. The expressions of body force coefficients are not unique, as long as they are good enough to tune the loss and deviation by measurement. The "second step calibration" means linking the two operating points by expressing the body force coefficients as a function of local flow property. From the results, we can see that for rotor deviation angle, the calibrated body force can qualitatively capture the correct trend that when the compressor is going to stall, there is a large increase in the rotor deviation angle in the tip region (Fig. A.9 and Fig. A.13). As for rotor loss coefficients, the calibrated body force yields rather good agreement with measurement, as seen in Fig.A.10 and Fig. A.14. Fig. A.11, Fig. A.12, Fig. A.15 and Fig. A.16 shows the stator deviation angle and loss comparison by calibration and measurement. The agreement is not so good compared with that of rotor. This is because in the first step calibration, the agreement of stator deviation and loss is not good enough. Since stator does not play a role as important as that of rotor in terms of instability behavior, we do not need to have a very high requirement on the agreement of stator body force calibration.

Fig. A.18 and Fig. A.19 show the comparison in total pressure ratio for rotor and stage between measurement and computation which uses calibrated body force. The results show that the computation agrees with the experiment reasonably well in the mass flow range between the two operating points near stall. The calibrated results can be summarized in Table A.1, which list the comparison of slope of characteristic line near stall.

	Measurement	Body force in Chapter 3	Body force in Chapter A
Slope of characteristic (s/kg)	0.003	0.06	0.03

Table A.1 comparison of slope of characteristics

However, there is some deviation in the high mass flow range, this can be explained by the fact that the body force calibration is based on the experimental data for only two operating points near stall instead of the five operating points for the whole mass flow range.

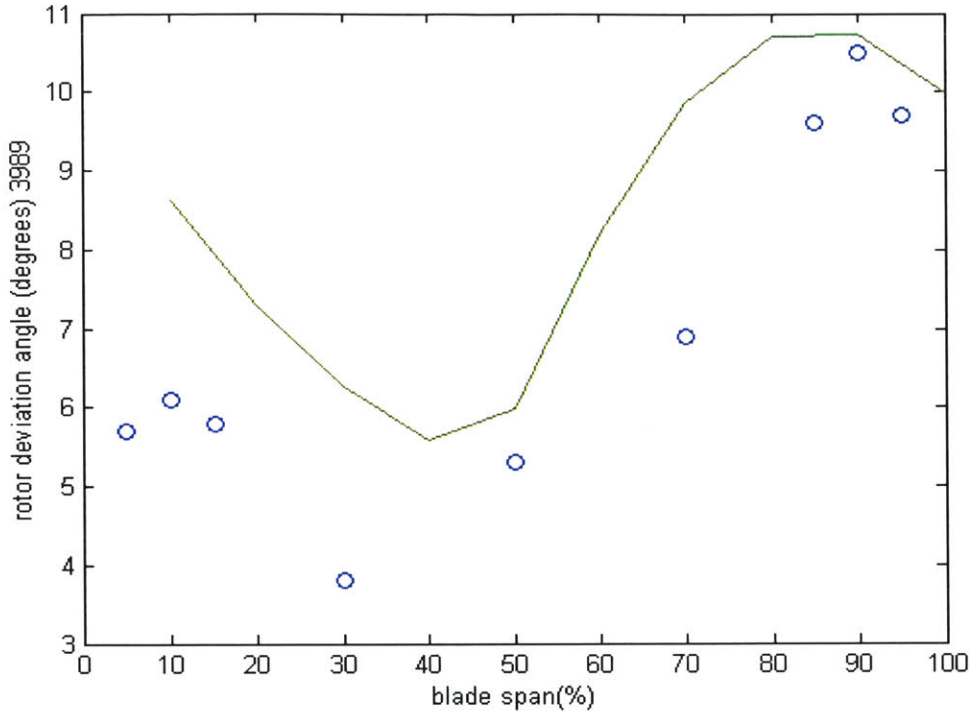

Fig. A.1 Rotor deviation distribution along blade span (mass flow=11.8 kg/s)

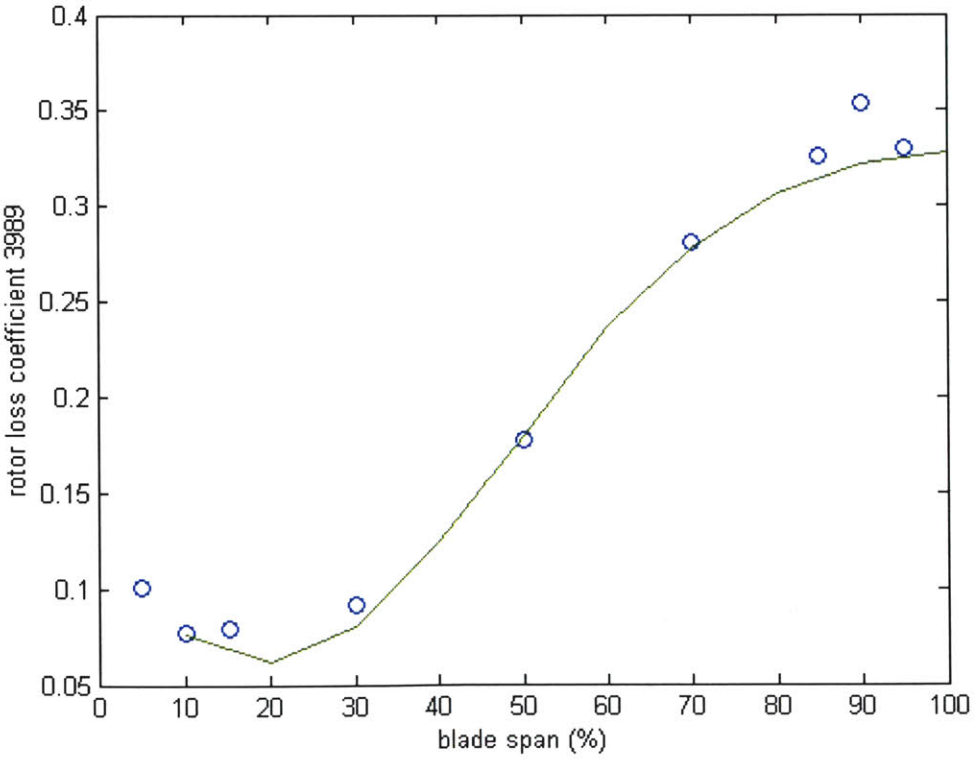

Fig. A.2 Rotor loss coefficient distribution along blade span (mass flow=11.8 kg/s)

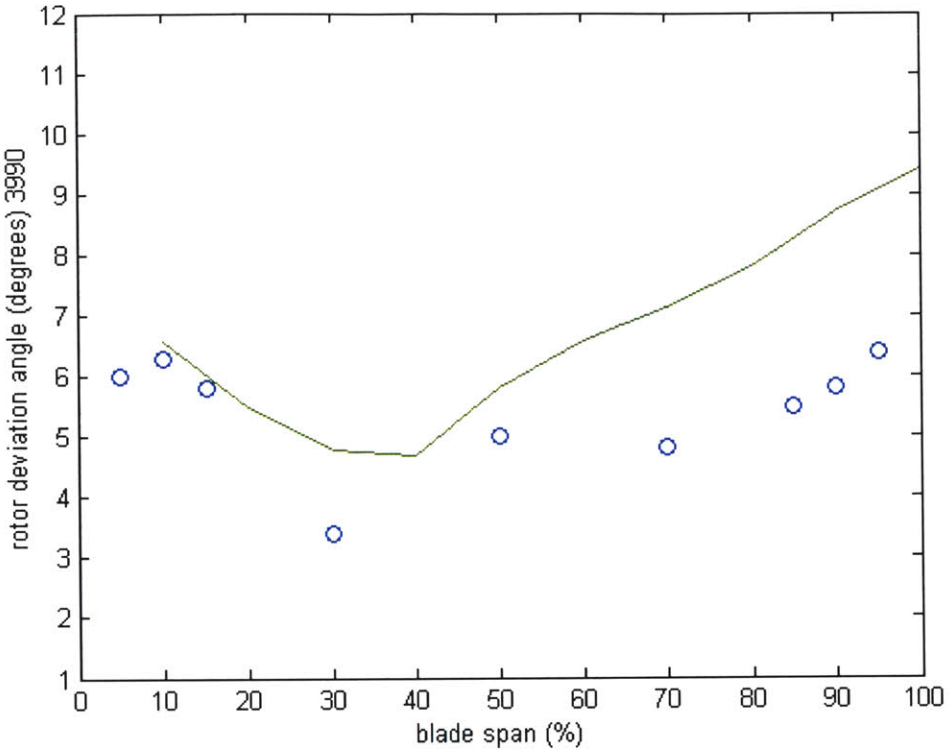

Fig. A.3 Rotor deviation distribution along blade span (mass flow=13.5 kg/s)

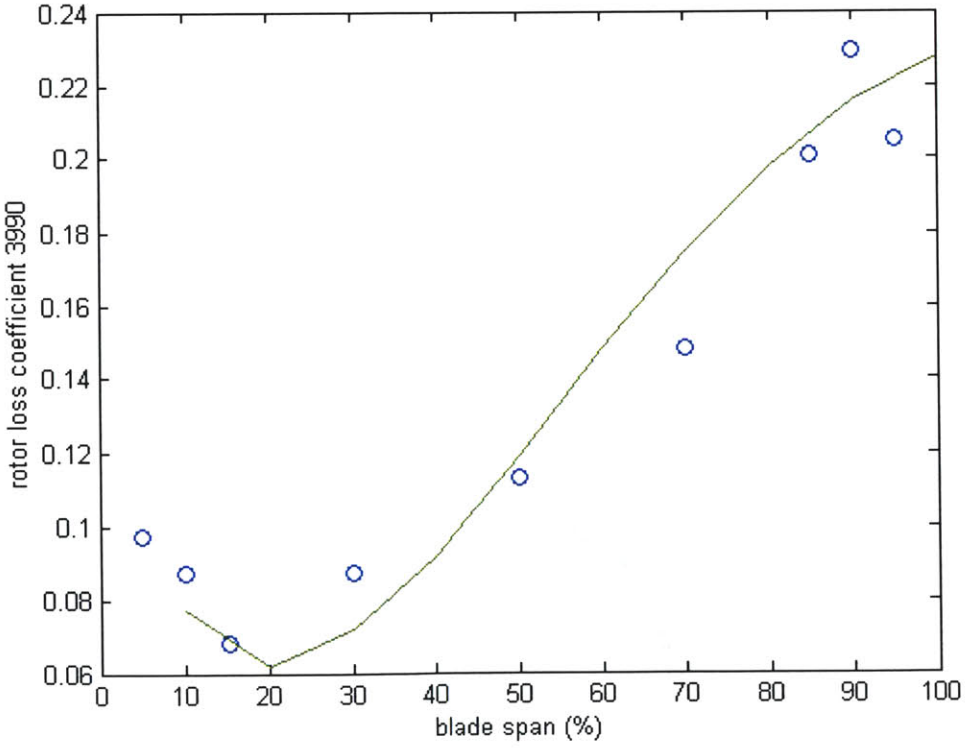

Fig. A.4 Rotor loss coefficient distribution along blade span (mass flow=13.5 kg/s)

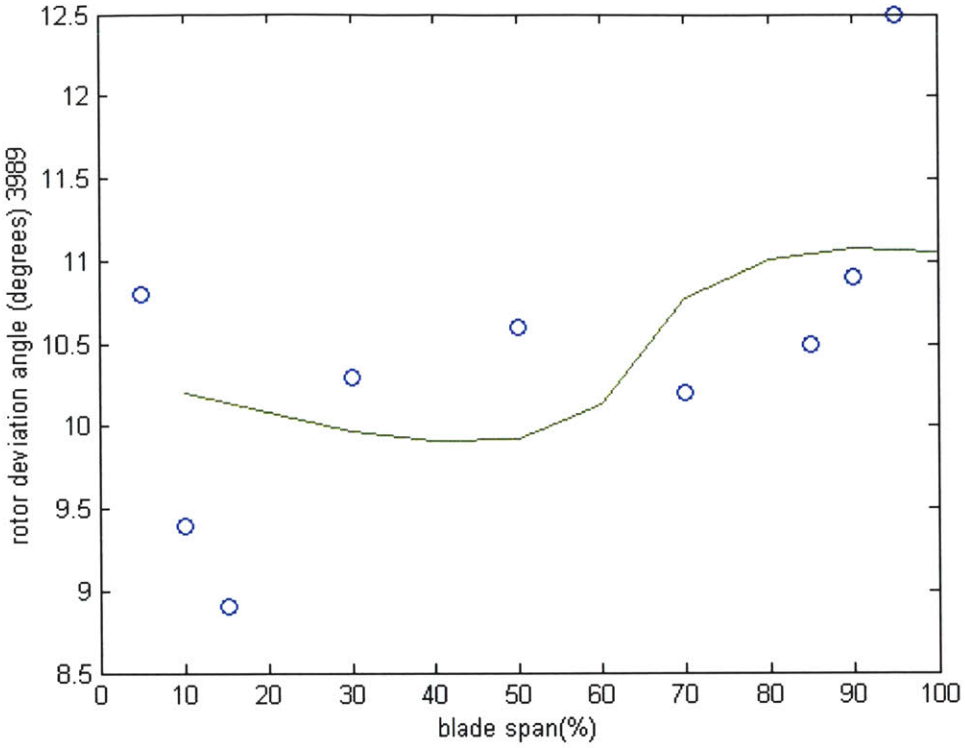

Fig. A.5 Stator deviation distribution along blade span (mass flow=11.8 kg/s)

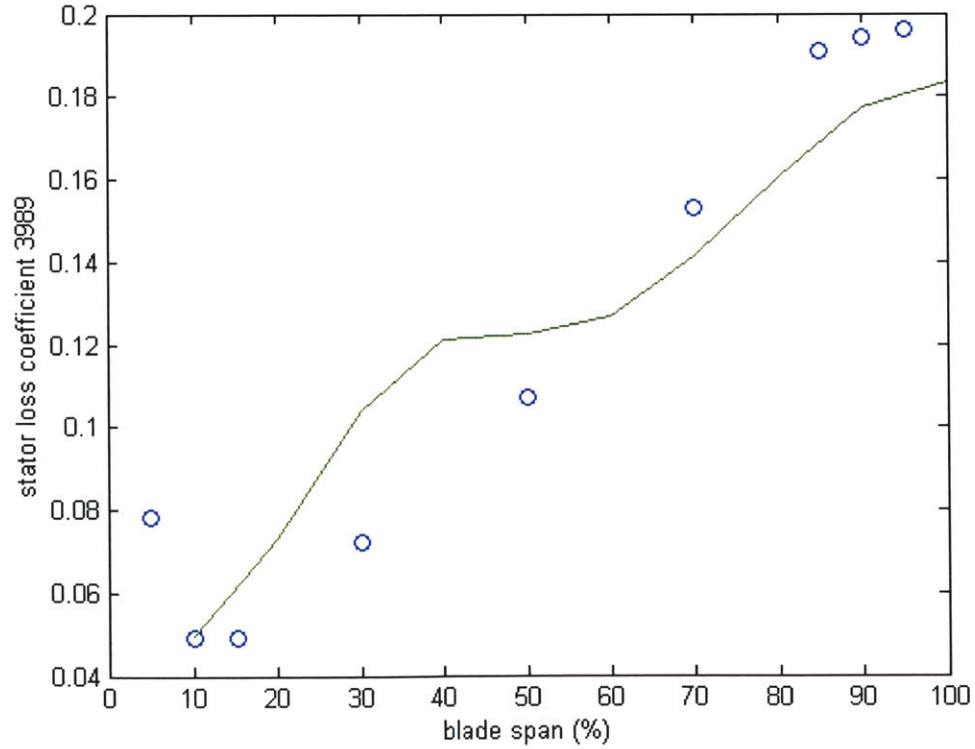

Fig. A.6 Stator loss coefficient distribution along blade span (mass flow=11.8 kg/s)

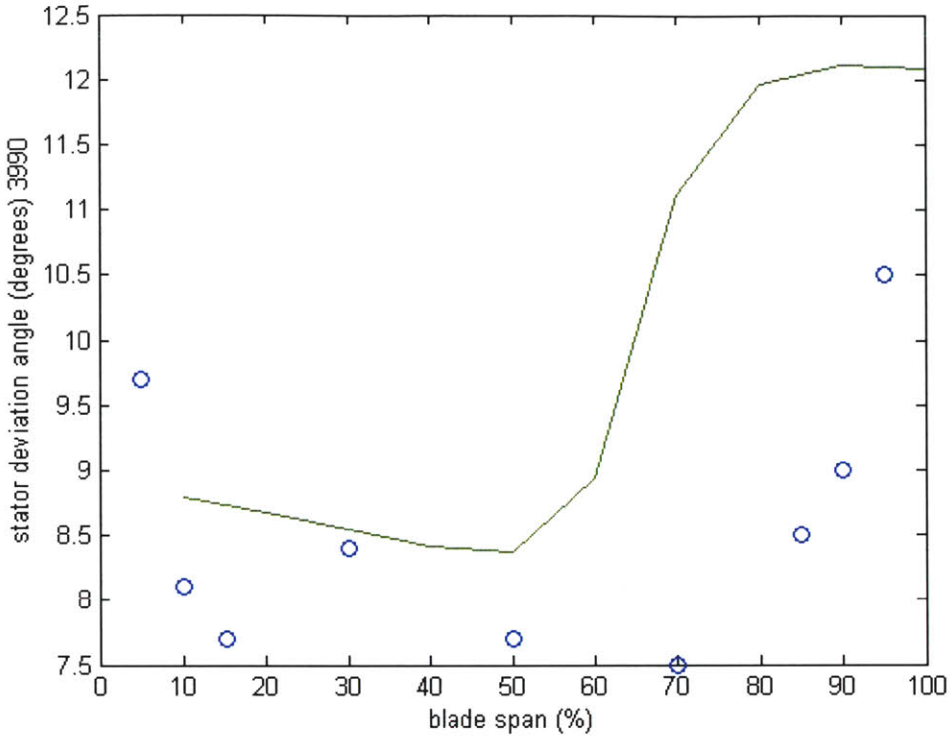

Fig. A.7 Stator deviation distribution along blade span (mass flow=13.5 kg/s)

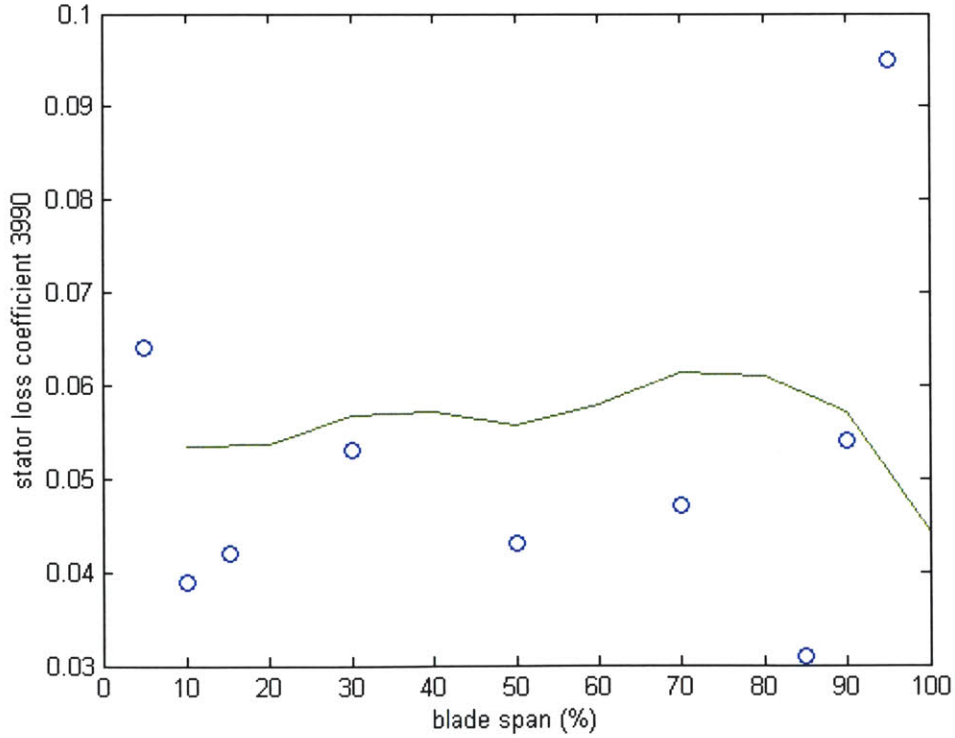

Fig. A.8 Stator loss coefficient distribution along blade span (mass flow=13.5 kg/s)

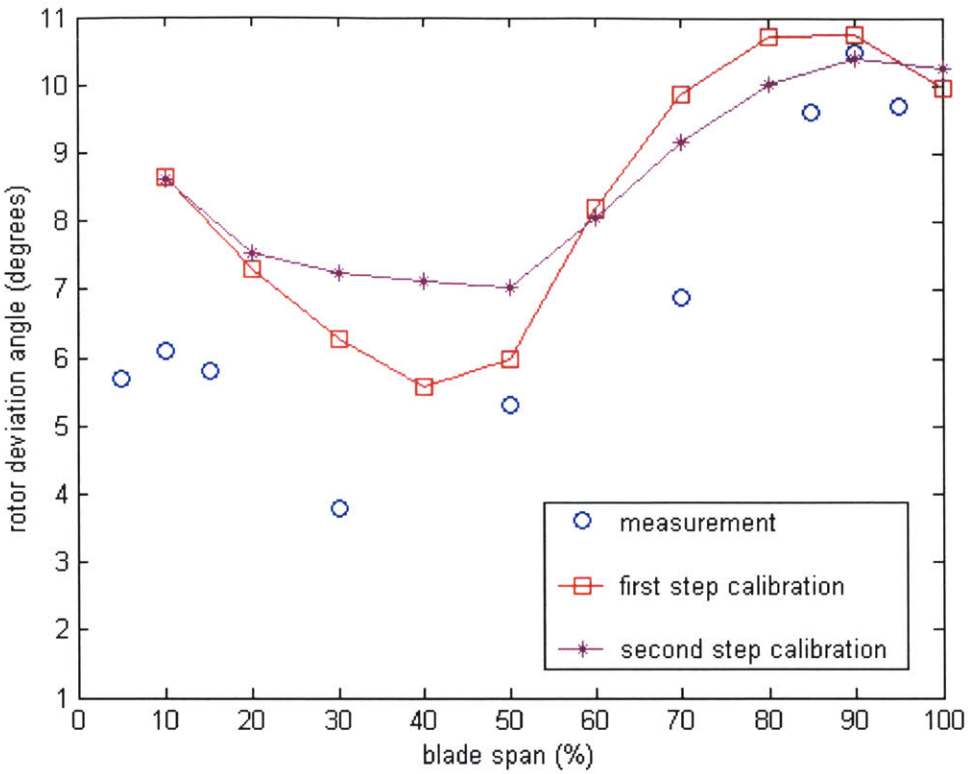

Fig. A.9 Rotor deviation angle by measurement and calibration (mass flow=11.8 kg/s)

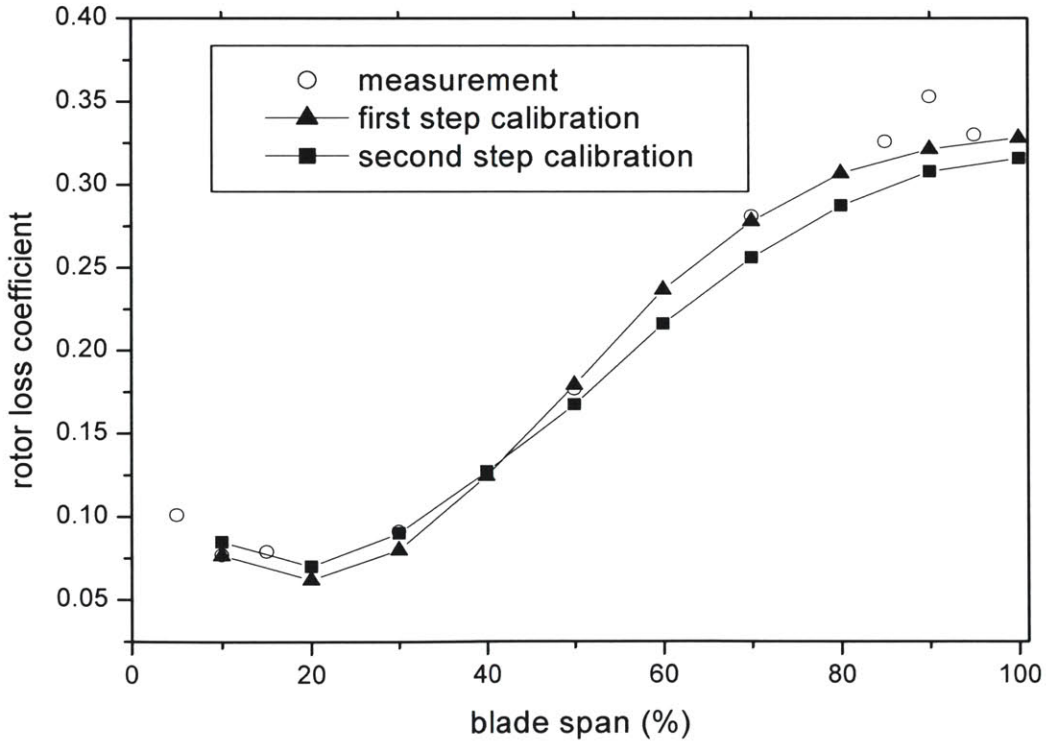

Fig. A.10 Rotor loss coefficient by measurement and calibration (mass flow=11.8 kg/s)

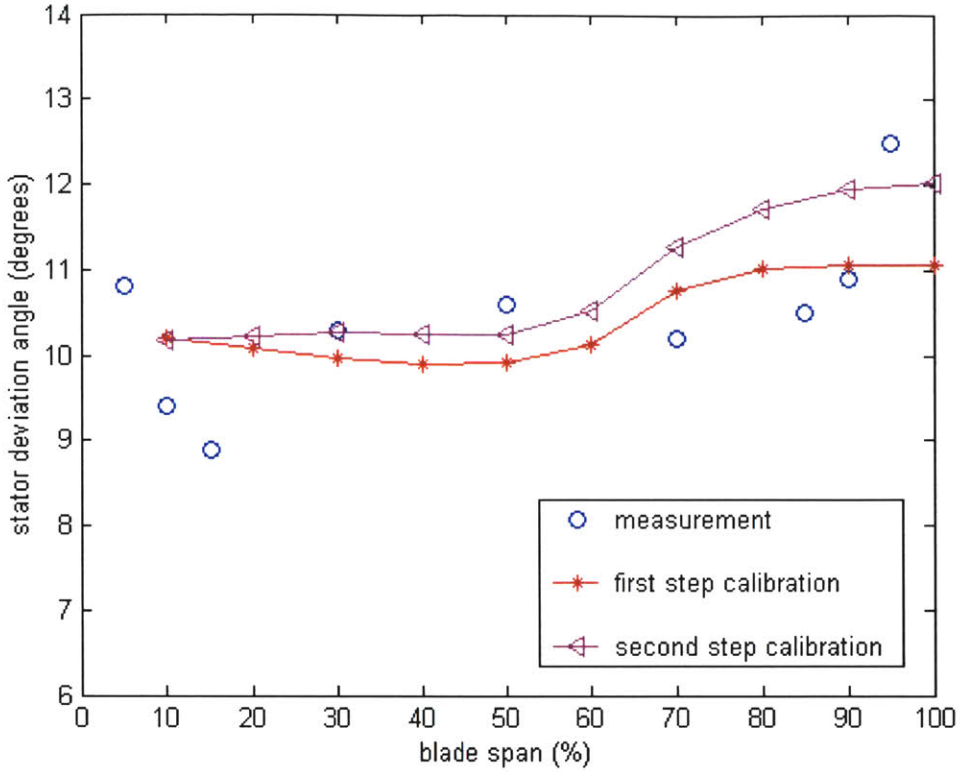

Fig. A.11 Stator deviation angle by measurement and calibration (mass flow=11.8 kg/s)

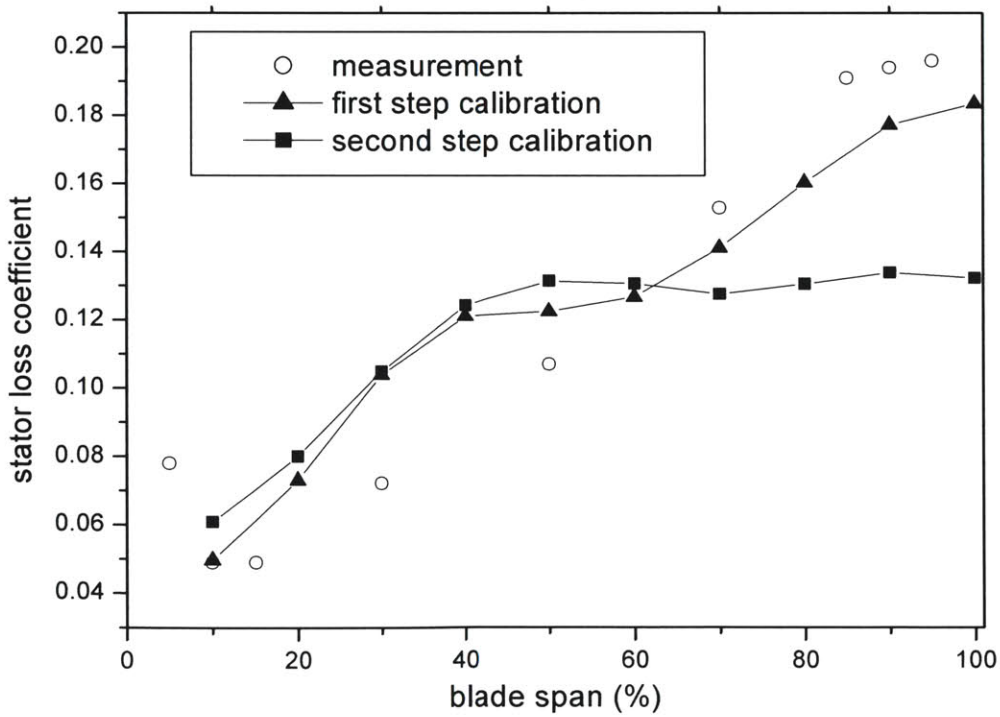

Fig. A.12 Stator loss coefficient by measurement and calibration (mass flow=11.8 kg/s)

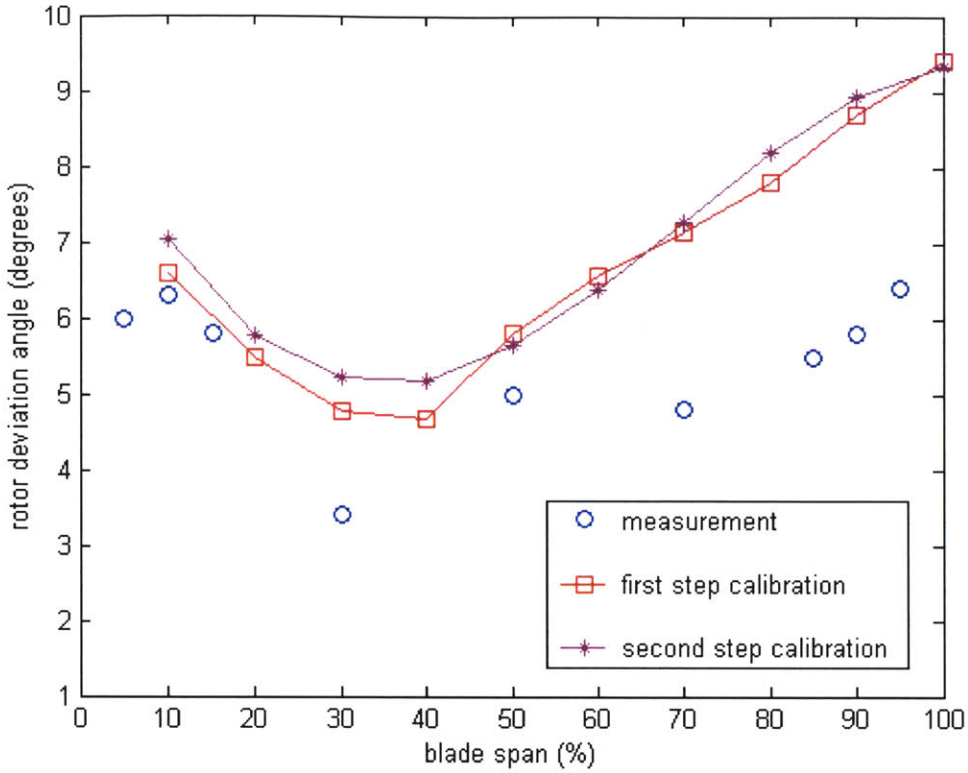

Fig. A.13 Rotor deviation angle by measurement and calibration (mass flow=13.5 kg/s)

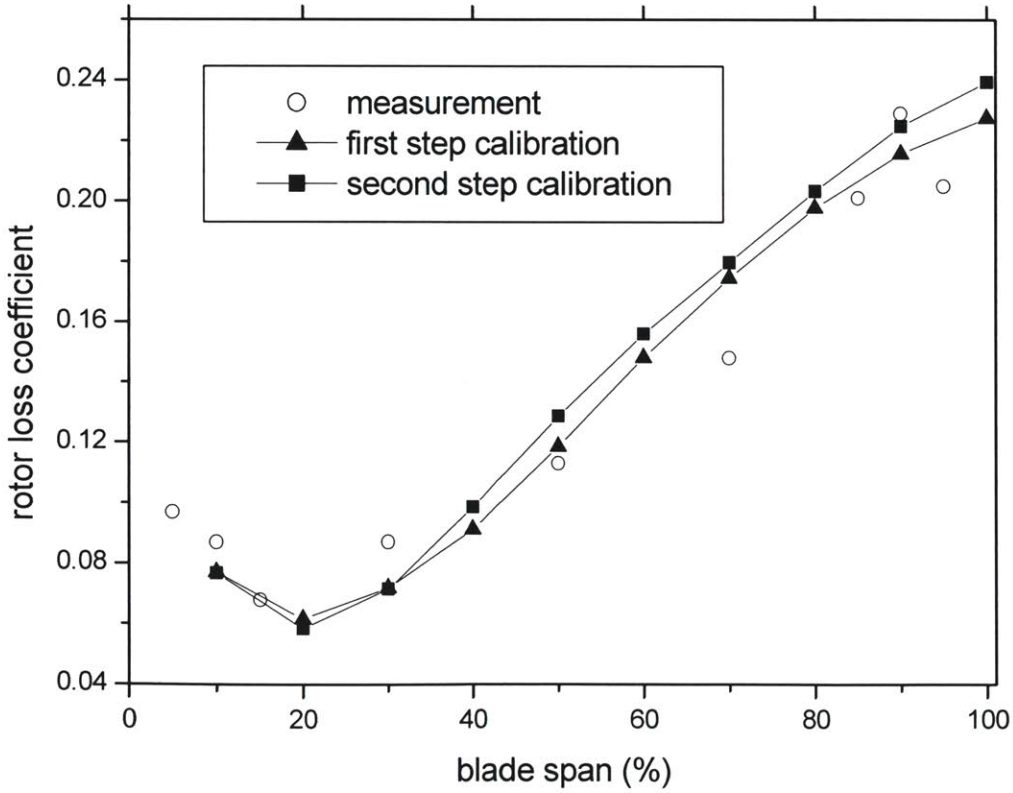

Fig. A.14 Rotor loss coefficient by measurement and calibration (mass flow=13.5 kg/s)

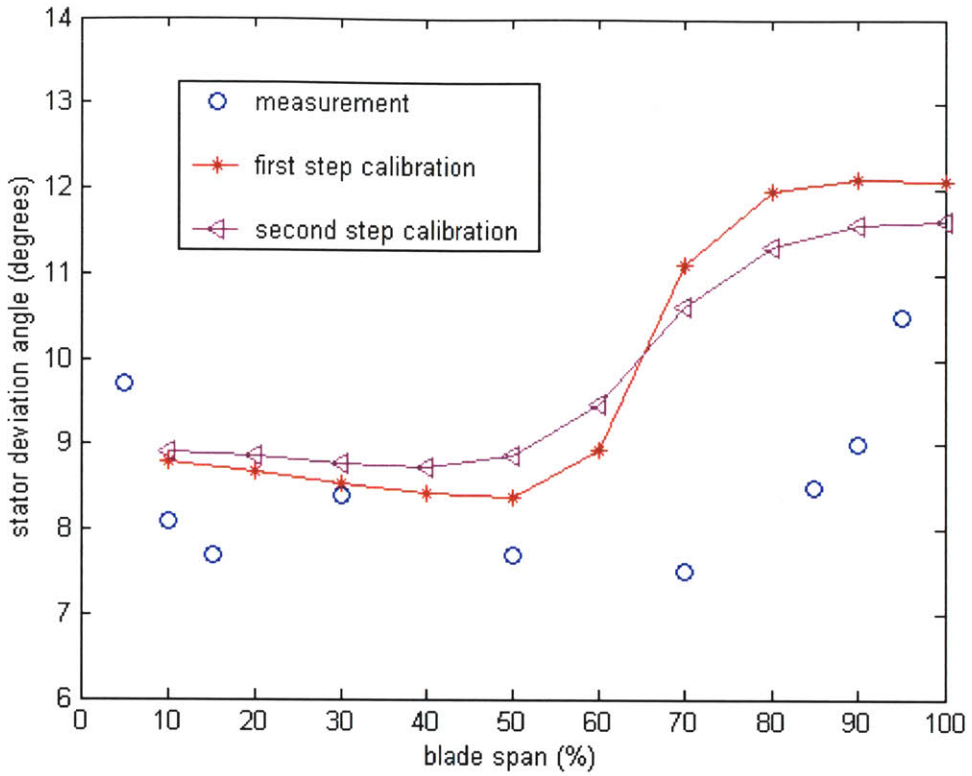

Fig. A.15 Stator deviation angle by measurement and calibration (mass flow=13.5 kg/s)

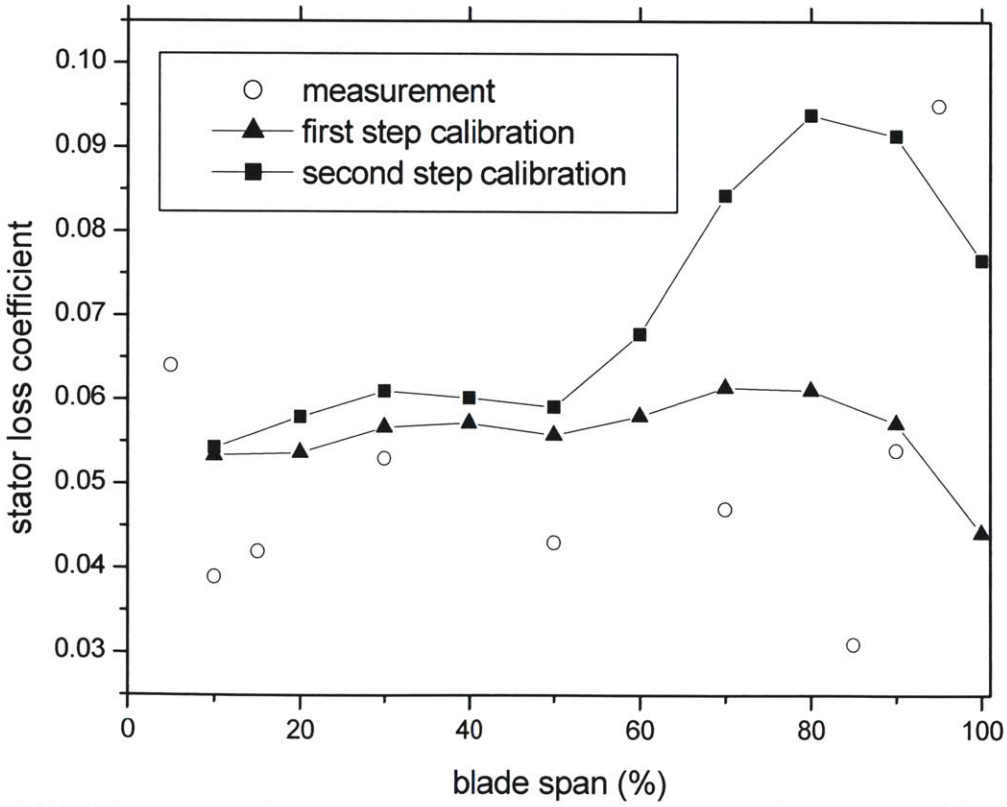

Fig. A.16 Stator loss coefficient by measurement and calibration (mass flow=13.5 kg/s)

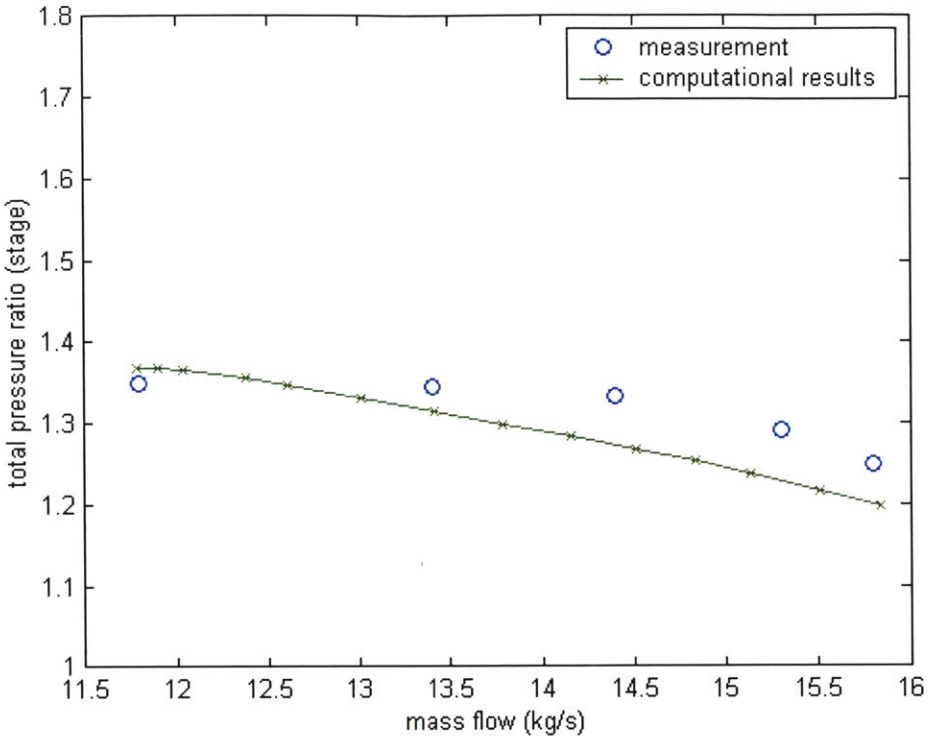

Fig. A.17 Comparison between measurement and computation for stage total pressure ratio

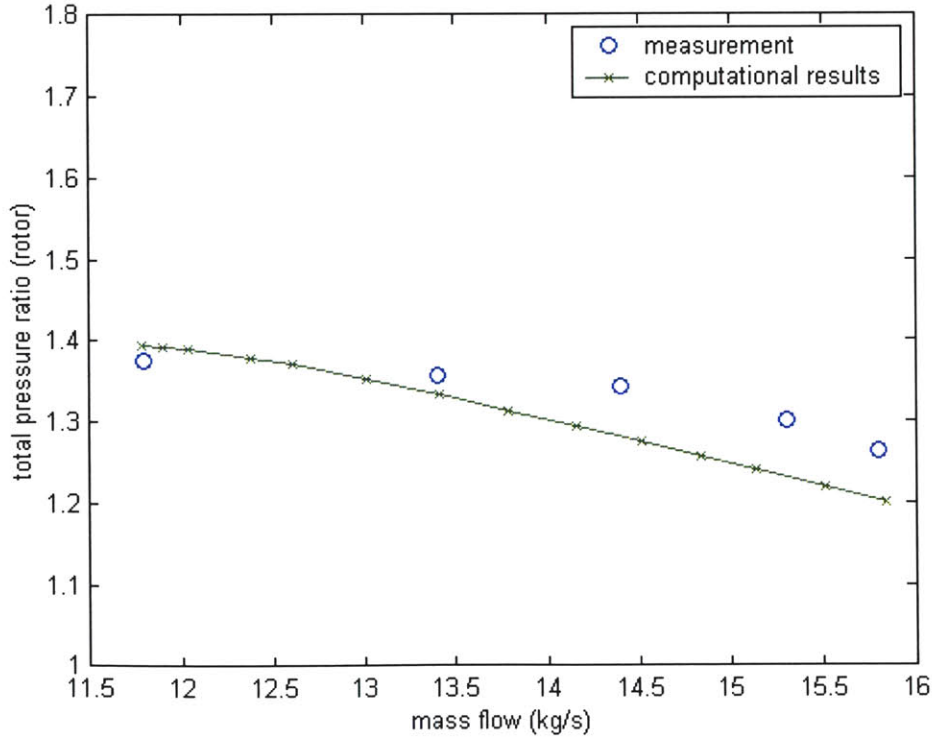

Fig. A.18 Comparison between measurement and computation for rotor total pressure ratio

Appendix III
Introduction and Solution of Ill-Posed Problem

I. Introduction

According to Hadamard's definition, if the solution to a problem exists, is unique, and depends continuously on boundary conditions and initial conditions, this problem is well-posed, otherwise, it is ill-posed [45]. For most ill-posed problems encountered in various fields of Science and Engineering, the existence and uniqueness of the solutions can be satisfied, but the condition "the solutions depend continuously on boundary conditions and initial conditions" cannot be satisfied. For most ill-posed problems in the field of Engineering, the errors in measurement or computer round-off errors is unavoidable, while the solutions of ill-posed problems are very sensitive to errors, small errors in the input data can lead to large errors in solutions.

II. Solution of Ill-Posed Problem

In general, the ill-posed problem can be formulated into a matrix equation:

$$Ax = b \tag{A.1}$$

where A is the model matrix with an overdetermined dimension $m \geq n$.

For a ill-posed problem, the matrix A is ill-conditioned, some general methods such as Gauss elimination, LU factorization, and QR factorization cannot be employed to solve the problem since zero pivots will always occur and result in large errors in the solution. In order to overcome the above difficulty, Tikhonov regularization method [41] [42] is employed to find the minimum norm solution of the following least square problem:

$$\min_x (\| Ax - b \|_2 + \lambda \| Lx \|_2) \tag{A.2}$$

where λ is the regularization parameter which controls the weight given to minimization of the seminorm $\| Lx \|_2$ of the solution relative to minimization of the residual norm $\| Ax - b \|_2$.

Decompose the model matrix A by Singular Value Decomposition (SVD) [43]:

$$A = U\Sigma V = \sum_{i=1}^{n} u_i \sigma_i v_i^T \tag{A.3}$$

where $U = (u_1,...u_n)$ and $V = (v_1,...v_n)$ are matrices with orthonormal columns, $U^T U = I_m$, $V^T V = I_n$, and T denotes transposition. σ_i are the singular values with $\sigma_1 \geq \cdots \geq \sigma_n \geq 0$. Then the final form of Tikhonov regularization solution can be written as:

$$x_{reg} = \sum_{i=1}^{n} \sigma_i \frac{u_i^T b}{\sigma_i^2 + \lambda^2} v_i \tag{A.4}$$

The ill-conditioning matrix A has the following two most important characters:

I. The singular values of A decay to zero gradually.

II. The condition number (the ratio of the maximum singular value to minimum singular value) of A is very large

For a ill-conditioning matrix, a cluster of singular values are very close to zero, part of them are contaminated by measurement and round-off errors. The essence of the regularization parameter λ is to filter out the influence of these components, thus yielding stable solutions. It's easy to see from formula (A.4) that even if $\sigma_i \to 0$, the division by zero does not occur.

III. Choice of regularization parameter

In Tikhonov regularization method, the choice of regularization parameter λ plays an important role in solving the ill-posed problem. A good regularization parameter can suitably balance the perturbation errors and the errors introduced by regularization parameter, thus producing a good solution. The General Cross-Validation (GCV) [44] criterion is employed in this thesis to choose the regularization parameter. Once the SVD of matrix A is finished, the GCV function of the Tikhonov regularization method can be expressed as:

$$V(\lambda) = \frac{\| b \|^2 - \| z \|^2 + \sum_{i=1}^{n} \left[\frac{\lambda^2}{\sigma_i^2 + \lambda^2} \right]^2 z_i^2}{[m - n + \sum_{i=1}^{n} \frac{\lambda^2}{\sigma_i^2 + \lambda^2}]^2}$$

where $z = U^T b$.

The optimal value of regularization parameter λ_{opt} is determined by minimization of the GCV function $V(\lambda)$.

IV. Solving the Matrix Equation in Body Force Calibration

For simplicity, the part will only treat with how to get the rotor body force coefficients in normal direction by solving the matrix equation with the Tikhonov regularization method mentioned above. Other body force coefficients (rotor body force coefficients in parallel direction, stator body force coefficients in both normal and parallel directions) are obtained by the same way.

For the matrix equation 4.

$$\begin{bmatrix} 1 & \beta_{1,r} \\ 1 & \beta_{2,r} \end{bmatrix} \begin{bmatrix} A_0 \\ A_1 \end{bmatrix} = \begin{bmatrix} K_{n1,r} \\ K_{n2,r} \end{bmatrix}$$

The detailed structure of the coefficient matrix is:

$$\begin{bmatrix} \begin{bmatrix} 1 & \beta_{1r,1} \\ 1 & \beta_{2r,1} \end{bmatrix} & & & & 0 \\ & \begin{bmatrix} 1 & \beta_{1r,2} \\ 1 & \beta_{2r,2} \end{bmatrix} & & & \\ & & \ddots & & \\ & & & \begin{bmatrix} 1 & \beta_{1r,119} \\ 1 & \beta_{2r,119} \end{bmatrix} & \\ 0 & & & & \begin{bmatrix} 1 & \beta_{1r,120} \\ 1 & \beta_{2r,120} \end{bmatrix} \end{bmatrix}$$

it is a square sparse matrix with dimension 240×240. The index 1,2,...120 denote the cell number on the rotor, the index $1r$, $2r$ stand for calibration of rotor body force using the two operating points near stall. The local deviation β is distribution on the whole rotor blade which were obtained in the first step calibration as described in Section 4.3.

The structure of right hand side is

$$\begin{bmatrix} K_{n1,1} \\ K_{n1,2} \\ \vdots \\ K_{n1,120} \\ K_{n2,1} \\ K_{n2,2} \\ \vdots \\ K_{n2,120} \end{bmatrix}$$

it is a column vector with dimension 240×1, all the K_n are also obtained in the first step calibration.

By doing the Singular Value Decomposition (SVD) of the coefficient matrix, the condition number of the coefficient matrix can be calculated by

$$cond(A) = \sigma_{\max} / \sigma_{\min}$$

It is found to be ~ 10^3, this means the coefficient matrix is ill-conditioned and can not be solved by standard matrix solver such as GAUSS elimination, LU, QR. Tikhonov regularization method is employed in this thesis to solve this problem.